



**HAL**  
open science

## Climate-driven deposition of water ice and the formation of mounds in craters in Mars' North Polar Region

Susan J. Conway, Niels Hovius, Talfan Barnie, Jonathan Besserer, Stéphane Le Mouélic, Roberto Orosei, Natalie Anne Read

### ► To cite this version:

Susan J. Conway, Niels Hovius, Talfan Barnie, Jonathan Besserer, Stéphane Le Mouélic, et al.. Climate-driven deposition of water ice and the formation of mounds in craters in Mars' North Polar Region. *Icarus*, 2012, 220 (1), pp.174-193. 10.1016/j.icarus.2012.04.021 . insu-02276816

**HAL Id: insu-02276816**

**<https://insu.hal.science/insu-02276816>**

Submitted on 3 Sep 2019

**HAL** is a multi-disciplinary open access archive for the deposit and dissemination of scientific research documents, whether they are published or not. The documents may come from teaching and research institutions in France or abroad, or from public or private research centers.

L'archive ouverte pluridisciplinaire **HAL**, est destinée au dépôt et à la diffusion de documents scientifiques de niveau recherche, publiés ou non, émanant des établissements d'enseignement et de recherche français ou étrangers, des laboratoires publics ou privés.

1 **Climate-driven deposition of water ice and the formation of**  
2 **mounds in craters in Mars' North Polar Region**

3  
4 Susan J. Conway\*

5 Laboratoire de Planétologie et Géodynamique de Nantes UMR-CNRS 6112,  
6 Université de Nantes, 2 rue de la Houssinière, BP92208, 44322 Nantes, France.  
7 susan.conway@univ-nantes.fr

8  
9 Niels Hovius

10 Dept. of Earth Science, University of Cambridge UK, CB2 3EQ.  
11 nhovius@esc.cam.ac.uk

12  
13 Talfan Barnie

14 Dept.of Geography, University of Cambridge UK, CB2 3EN.

15  
16 Jonathan Besserer

17 Laboratoire de Planétologie et Géodynamique de Nantes UMR-CNRS 6112,  
18 Université de Nantes, 2 rue de la Houssinière, BP92208, 44322 Nantes, France.

19  
20 Stéphane Le Mouélic

21 Laboratoire de Planétologie et Géodynamique de Nantes UMR-CNRS 6112,  
22 Université de Nantes, 2 rue de la Houssinière, BP92208, 44322 Nantes, France.

23

24 Roberto Orosei

25 Istituto di Astrofisica Spaziale e Fisica Cosmica (IASF), Italy

26

27 Natalie Anne Read

28 Dept. of Earth Science, University of Cambridge UK, CB2 3EQ.

29

30 \*Corresponding author

31

32 **Short title:** A climatic origin of crater-ice in Mars' North Polar Region

33

34        **Abstract**

35    This paper explores the origins and evolution of ice-rich interior mounds found within craters  
36    of the north polar region of Mars. We present a systematic study of impact craters above  
37    65°N, and identify 18 craters that have interior mounds. At least eleven of these mounds are  
38    composed of water ice and geometric similarities suggest that dune-covered mounds may  
39    also have a water ice core. The mounds are found in the deeper craters in the north polar  
40    area and we suggest that these form a specific microclimate favorable for mound initiation  
41    and growth. It is likely that at least seven of the mounds have evolved as individual outliers,  
42    rather than conterminous with the main polar cap. Our observations suggest that the  
43    mounds are built up by atmospheric deposition, similar to that of the north polar layered  
44    deposits. Using a combination of remote sensing techniques enabling topographic, spectral,  
45    radar and image data analyses, we have documented the morphology, composition and  
46    stratigraphy of selected mounds. We advance and test four hypotheses for formation of  
47    these mounds: artesian outpouring from a deep aquifer, hydrothermal activation of ground  
48    ice, remnants of a more extensive polar cap, and atmospheric deposition on ice caps in  
49    meteorologically isolated locations. We propose that during periods when the perihelion was  
50    located in northern summer (most recently 10-25 ka before present) the microclimate in  
51    these craters retarded the sublimation of CO<sub>2</sub> and water ice in northern spring, thus creating  
52    a cold trap for volatiles released as the seasonal cap retreated. This created a thick enough  
53    deposit of water ice to withstand sublimation over the summer and initiate a positive  
54    feedback leading to mound-building. Mounds without complete dune-cover may be in  
55    dynamic equilibrium with the ambient climate and show evidence of both present-day and  
56    past periods of erosion and aggradation. We conclude that the water ice mounds formed in  
57    deep impact craters in Mars' north polar region may contain sensitive records of past polar  
58    climate that may enhance our understanding of the CO<sub>2</sub>-H<sub>2</sub>O system in the polar regions.

59    **Keywords: Mars; ices; Mars, polar geology; Mars, climate; Cratering.**

60 **Highlights:**

- 61 • 18 potentially ice-cored mounds were found in craters in Mars' north polar region.
- 62 • The stratigraphy of the mounds argues for deposition from the atmosphere.
- 63 • We argue many of them were deposited separately from the polar cap.
- 64 • The crater micro-environment is a potential explanation for mound initiation.
- 65 • These mounds are sensitive and important records of Amazonian climate on Mars.

66

## 67 **1. Introduction**

68 The northern lowlands of Mars have long been considered an important reservoir for water.  
69 It has been suggested that a northern ocean existed there in the Noachian and that water  
70 may now be present deep in the local subsurface (e.g., Clifford, 1993; Clifford and Parker,  
71 2001; Perron et al., 2007). More pertinently, the northern polar cap, with an estimated  
72 volume of  $1.3 \times 10^6 \text{ km}^3$  (Selvans et al., 2010) consists of a mixture of water ice and dust,  
73 and a region of near-surface ground ice extends down to latitudes of  $45^\circ$  (Byrne et al. 2009).  
74 This was first shown by the hydrogen ion signature found by gamma ray spectrometry  
75 (Feldman et al., 2004; Jakosky et al., 2005) and later supported by spectral signatures from  
76 OMEGA (Bibring et al., 2005), the distribution of water surface frosts (Vincendon et al.,  
77 2010), the distribution of fluidized craters (Barlow and Perez, 2003) and the radar reflectivity  
78 properties of the surface (Mouginot et al., 2010), with ice found by the Phoenix lander  
79 (Mellon et al., 2008) providing a local ground truth. Seasonal cycles mobilize and redistribute  
80 these surface volatiles; principally those exposed on the polar cap. At present, the most  
81 noticeable seasonal change is the waxing and waning of the so called 'seasonal' polar caps,  
82 observable from Earth (e.g., Antoniadi, 1930). The northern hemisphere seasonal cap  
83 commonly extends down to  $50^\circ\text{N}$  and consists primarily of  $\text{CO}_2$  ice. It has a thickness of  
84  $\sim 0.5 \text{ m}$  (Cull et al., 2010; Smith et al., 2001), and is sourced from the atmosphere by  
85 condensation of water followed by  $\text{CO}_2$  (Ivanov and Muhleman, 2001). Deposition occurs  
86 during the polar night and so has not been directly observed, but is thought to involve  
87 atmospheric condensation possibly as snow from ubiquitous cloud-cover. The spring  
88 recession is better characterized and it comprises a gradual northward retreat first of the  
89  $\text{CO}_2$ , then of the thinner water-ice annulus (Bibring et al., 2005; Wagstaff et al., 2008).

90 After recession of the seasonal volatile deposits there remain several substantial outliers  
91 composed of water ice, which are spatially separated from the northern polar cap (Langevin  
92 et al., 2005; Tanaka et al., 2008). Many of these ice bodies are found within craters, e.g.,

93 Korolev, Dokka and Louth. They are morphologically distinctive (Garvin et al., 2000), forming  
94 an interior mound, which is convex-up and dome-shaped, with low local slopes and a moat  
95 that separates it from the crater walls. These mounds are distinct from an impact central  
96 peak, because they have convex-up positive relief in the center, often with a large volume  
97 placed asymmetrically within the crater. These mounds are generally assumed to be  
98 remnants of a previously more extensive northern ice cap (Garvin et al., 2000; Tanaka et al.,  
99 2008). Other possible origins include: upwelling from an underground aquifer (proposed but  
100 not supported by Russell and Head, 2002), activation of near-surface ground ice by impact-  
101 induced hydrothermal systems (a possibility considered for paleolake formation by Osinski et  
102 al., 2005; Rathbun and Squyres, 2002) and atmospheric condensation as individual outliers  
103 of the main cap (Brown et al., 2008). Although the latter invokes atmospheric deposition, as  
104 for the polar cap, it differs significantly from the formation of polar cap remnants in that 1) a  
105 larger extent of the polar cap is not required and 2) more importance is given to  
106 microclimatic effects inside the craters. Each of these formative mechanisms has important,  
107 but different, implications for the dynamics of Mars' hydrosphere and climate. For example, if  
108 they are indeed remnants of a formerly more extensive polar cap, then these mounds are  
109 important records of both its extent and the conditions needed to preserve this ice. If sourced  
110 from near-surface, or deep ground-ice, then the mounds give information on the distribution  
111 of this ice and an indication of the volumes of water stored in the Martian crust. If the  
112 mounds are supplied from deep sources, then this could support the presence of a deep,  
113 global hydrosphere (Clifford, 1993). And if they are individual cap outliers, then the mounds  
114 could be sensitive to climate perturbations and hence, their spatial distribution, morphology  
115 and internal structure can help place constraints on recent climate.

116 The aim of this study is to explore the origins and evolution of interior mounds that are found  
117 within some craters in the North Polar region of Mars. To this end, we document and  
118 interpret the distribution, morphology and internal structure of these mounds, finding that the

119 majority have likely formed by atmospheric deposition triggered by microclimatic effects  
120 inside the host craters, separate from the main polar cap.

## 121 **2. Approach**

### 122 **2.1 Craters in the north polar basin**

123 We have based our impact crater survey on information from the Mars Orbiter Laser  
124 Altimeter (MOLA) gridded data at 256 and 128 pixels per degree for the north polar region,  
125 recording the locations and morphometric properties of all craters that are hydrologically  
126 intact including craters with internal mounds. This survey is complete for craters with a  
127 diameter >5 km, located north of 65°N (Barnie, 2006).

128 Impact craters were identified and digitized from MOLA data using a watershed analysis  
129 technique aimed at delineating crater rims (*cf.* Stepinski et al., 2009). Each crater was given  
130 a unique identifying number (Barnie, 2006; Hovius et al. 2009). Based on visual inspection of  
131 the Thermal Emission Imaging System (THEMIS) and Mars Orbiter Camera Narrow-Angle  
132 (MOC-NA) image mosaic data we identified craters containing dune fields. Dune fields were  
133 identified by morphology where image resolution was sufficient and elsewhere by a  
134 characteristic combination of high IR emission values in THEMIS IR daytime data and low  
135 reflection of visible light in THEMIS VIS.

136 For all impact craters in our catalogue, we obtained elevation statistics from the MOLA digital  
137 elevation model (DEM) including the maximum, minimum and range. The latter was used as  
138 an estimate of the overall crater depth. The mean crater diameter was calculated by using  
139  $D = 2 \sqrt{A/\pi}$ , where  $D$  is the diameter and  $A$  the area of the digitized rim polygon. This  
140 method assumes the rim traces a circle and is not biased by topographic irregularities or  
141 slight obliquity of the crater-form. The distance from a crater to the polar cap was measured  
142 along the shortest straight line from the crater centroid to the edge of the contiguous Polar  
143 Layered Deposits and Polar Ice Deposits as mapped by Tanaka et al. (2005).



144 From our catalogue, we have isolated all craters containing raised central topography for  
145 further analysis. The following additional criteria were applied:

- 146 1. To identify and exclude central peaks: North-south and east-west topographic  
147 profiles were taken across these craters. Craters with central peaks were recognized  
148 by the small extent ( $< 10\%$  of the crater floor) and central position of the rise and the  
149 similarity of rise and crater wall albedo. These craters were not considered further.
- 150 2. For the remaining craters where the presence of dark dunes dominated the albedo of  
151 deposits within a crater, we applied a minimum relief of 150 m in our identification of  
152 mounds. This is the maximum relief of inner-crater dunefields measured outside of  
153 the survey area, and the cut-off eliminated only one mound from our survey (marked  
154 332 in Fig. 2).

155 As the resulting mounds have geometries and surface attributes distinct from those of  
156 central peaks, they were deemed to be depositional in origin. We digitized the limit of the  
157 mounds using the topographic inflexion at the transition to concave-up crater topography as  
158 a guide. Mound volume was estimated from surface topography and an extrapolation of the  
159 crater floor below the mound (not including any estimate of a central peak). This involved  
160 rotating through  $360^\circ$  the power-law best fit to the median radial profile of the crater interior  
161 (excluding any areas containing the mound) and differencing this estimated surface with the  
162 MOLA topography to generate an isopach map for each mound. Using this map we also  
163 calculated the mound asymmetry by measuring the horizontal offset between the center of  
164 mass of the mound and the centroid of the crater rim.

## 165 **2.2 Mound Composition**

166 We have investigated the composition of surface materials on the crater mounds using data  
167 from Mars Express' Observatoire pour la Minéralogie, l'Eau, les Glaces et l'Activité (MEX  
168 OMEGA) imaging spectrometer and Mars Reconnaissance Orbiter's Compact

169 Reconnaissance Imaging Spectrometer for Mars (MRO CRISM) targeted observations to  
170 compute simple diagnostic ratios, including band depth and drop-off. OMEGA has a nearly  
171 complete coverage of the north polar region at a spatial resolution of  $\sim 3 - 7$  km/pix and also  
172 covers selected areas at 0.5 - 1.5 km/pix. CRISM targeted observations have much lower  
173 global coverage, but a very high spatial resolution of 15.7 - 19.7 m/pix. Both datasets  
174 underwent standard atmospheric correction before spectral analysis (“volcano-scan”  
175 algorithm, cf. Morgan et al., 2009). Although aerosol effects, not accounted for in this  
176 correction, can be important in the north polar region (Vincendon et al. 2006; Vincendon  
177 2008), the strong reflectivity of water and CO<sub>2</sub> ice overwhelms the atmospheric effects  
178 allowing reliable identification (Brown et al., 2010). Datasets from northern summer (Solar  
179 longitude,  $L_s$  90 - 120°) were used to avoid seasonal CO<sub>2</sub> surface frost, which could mask  
180 any spectral signals from the material beneath (Bibring et al., 2005). The relative depth of  
181 the absorption band at 1.50  $\mu\text{m}$  was used to estimate the water ice content. The depth of the  
182 absorption band at 2.35  $\mu\text{m}$  was used to estimate the quantity of carbon dioxide ice (Brown  
183 et al., 2010).

## 184 **2.3 Internal Stratigraphy**

185 The stratigraphy of mound materials was investigated with image data of surface outcrops  
186 and radar data capturing the interior stratigraphy. Surface stratigraphic information was  
187 obtained from images collected with THEMIS, High Resolution Stereo Camera (HRSC on  
188 Mars Express), MRO Context (CTX) and MRO High Resolution Imaging Science Experiment  
189 (HiRISE). All these images were either already geometrically corrected (HiRISE, HRSC), or  
190 corrected using routines in the software ISIS3. Alignment with the MOLA DEM was manually  
191 checked by verifying that local highs and local lows (e.g., crater rims, troughs) corresponded  
192 between the image and the MOLA data. For specific examples we measured the distance  
193 between the layers in plan-view. We assumed that the layers were approximately flat-lying  
194 and thus corrected the measured distances to account for exposure angle (which makes the

195 plan-view width of layers wider than their true thickness if the slope is less than 45°). This  
196 was done by measuring the local slope, derived from MOLA topography, in the same  
197 orientation as the layer thickness measurements. As the length scale of the MOLA-derived  
198 slope is approximately ten times larger than that of the measured layers, the slope correction  
199 introduces a degree of error, however it affects all measurements and no better source of  
200 topography is available at present. For comparison purposes, we made equivalent  
201 measurements of layer thickness in three exposures of the Polar Layered Deposits (PLD) in  
202 HiRISE images PSP\_010366\_2590, TRA\_000825\_2665 and TRA\_000863\_2640 and one  
203 exposure of the Basal Unit (BU) in HiRISE image TRA\_000863\_2640.

204 At selected locations we measured the junction angles of angular unconformities and/or  
205 discontinuities exposed in outcrop, and ascertained younging directions from the layer  
206 geometry. Where possible, dip and strike measurements of large-scale layering were made  
207 by employing the geometric relationships between individual layers and 25 or 50 m contours  
208 derived from the MOLA 512 and 256 pixels per degree data (~115 and ~230 m/pix,  
209 respectively). Dips and strikes were measured over a length-scale of kilometers, so should  
210 be considered as an area average value. We estimate the error in the dip measurement to  
211 be 1-2° as detailed below.

212 Uncertainty in the dip measurement derives from: 1) errors in the layer digitization, 2) human  
213 errors in the distance measurements and 3) errors in the contours. We consider the layers to  
214 be digitized to within 2 pixels of their actual location on the images (50 cm for HiRISE and  
215 12 m for CTX). We estimate the horizontal uncertainty of our distance measurements due to  
216 human error as being between 10 and 50 m, thus greater than the digitization uncertainty.  
217 Horizontal errors of this magnitude (over lengthscales of kilometers) account for at worst a  
218 2° error in dip, but usually  $\pm 1^\circ$ . Contour errors can originate from interpolated pixels in the  
219 MOLA DEM and misalignment of the DEM with the images. The interpolated pixels are a  
220 relatively small source of error, because we performed these measurements over smooth,  
221 continuous surfaces for which interpolation performs well, resulting in smooth contours with

222 regular intervals. The potential horizontal misalignment between the images and DEM  
223 dominates the error and we estimate it is of the order of 1-2 MOLA pixels (460 m at worst,  
224 but more likely 100-200 m). However this does not necessarily change the horizontal  
225 distance between the contours (and thus the dip measurement) unless the slope changes  
226 significantly over distances of 460 m or less in the region of measurement. For the majority  
227 of measurements this was not the case. However, we took three examples where this was  
228 the case (one in Korolev and two in crater 663) and shifted the contours in relation to the  
229 images by  $\pm 460$  m in the direction of greatest change in slope. This simulated “worse-case”  
230 misalignment resulted in an error in the measured dip angle of  $\pm 1.5^\circ$ .

231 We inspected all available MRO Shallow Radar (SHARAD) data intersecting craters with  
232 mounds for signs of internal structure. Where we found structure within mounds we  
233 performed clutter simulations using MOLA data to confirm that observed structures were not  
234 due to surface topographic effects (Russo et al., 2008). To assess layer spacing and  
235 thickness of mound deposits we converted the two-way-time into depth (cf. Plaut et al.,  
236 2009) using a permittivity of 3.15 as previously used by Putzig et al. (2009) for the nearly  
237 pure ice of the polar cap.

## 238 **3. Results**

### 239 **3.1 Northern plains craters morphology and distribution**

240 We found 397 craters with a diameter  $> 5$  km north of  $65^\circ\text{N}$ . The depth-diameter relationship  
241 for these craters is shown in Fig. 1. The relationship is described by  $d = 0.05D^{0.98}$ , where  $d$  is  
242 crater depth (km) and  $D$  is crater diameter (km). For comparison, Garvin et al. (2000) found  
243  $d = 0.03D^{1.04}$  for 109 impact craters north of  $57^\circ\text{N}$ . These relationships differ significantly  
244 from the global depth-diameter relationship for pristine craters as determined by Garvin  
245 (2005). Compared to the polar depth-diameter relationships, the global depth-diameter  
246 relationship predicts deeper craters for a given diameter, apart from for the very largest

247 diameter craters. The same trend has been noted by Boyce and Mouginis-Mark (2005) and  
248 Kreslavsky and Head (2006). This suggests that in the north polar area either, craters have  
249 been subject to significant infilling, or that the properties of local substrate differ substantially  
250 from the rest of Mars such that on formation impact craters are shallower compared to the  
251 global population. From morphological evidence and the existence of a small population of  
252 deep, young craters both Boyce and Mouginis-Mark (2005) and Kreslavsky and Head (2006)  
253 conclude that craters in the north polar area are infilled.

254 At least 38 craters with  $D > 5$  km contain dune fields. Dune fields were found in 28% of  
255 craters  $> 400$  m deep (Fig. 1), but not in shallower craters. Such dune fields are not  
256 restricted to the polar region; we have found them in 24% of craters between  $50^{\circ}\text{N}$  and  
257  $65^{\circ}\text{N}$ . At these latitudes, the relief of dune fields above the crater floor usually does not  
258 exceed 150 m and the deposits usually cover relatively small areas within a crater. At higher  
259 northern latitudes some craters have extensive dune cover. This includes some craters with  
260 depositional mounds with relief in excess of 150 m.

261 According to our criteria, eighteen craters were found to contain mounds (Fig. 2). They are  
262 located between  $70^{\circ}\text{N}$  and  $82^{\circ}\text{N}$ , and none are smaller than 9.5 km in diameter (Table 1).  
263 Seven are adjacent to the polar cap and the furthest is located  $> 600$  km from the cap. No  
264 craters with mounds were found between  $65$  and  $70^{\circ}\text{N}$ . Many of the mounds consistently  
265 have high albedo in summer months (e.g., Armstrong et al., 2007; Garvin et al., 2000).  
266 However, many other craters in the north polar region that do not contain interior mounds  
267 also have this attribute (Calvin et al., 2009; Seelos et al., 2008; and informally by the MRO  
268 HiRISE team). Craters with mounds lie within the general depth-diameter distribution of  
269 craters in this region (Fig. 1), but for a given diameter they are relatively shallow compared  
270 to other craters of the same diameter. This can be accounted for only in part by the presence  
271 of a mound (predicted depths are given in Table 1 and shown on Figs. 1 and 3). Moreover,  
272 mounds are not found in all craters of any particular diameter and not all craters at a given

273 latitude with a similar diameter contain a mound. In fact only 24% of all craters located  
274 above 70.1°N with diameters greater than 9.5 km have interior mounds.

275 Figure 3 shows two representative examples of impact craters with an interior mound (all the  
276 craters are shown in Fig. S1). Firstly, Dokka (388) with a clean ice mound, like Korolev (206)  
277 and six other, smaller craters in our survey and secondly crater 811 with a mound-shape  
278 similar to Dokka's, but entirely covered by dunes ("complete dune cover" on Fig. 2). Crater  
279 814 shares this characteristic. Four other craters have complete dune coverage, but their  
280 mounds do not span the whole crater floor (480, 882, 904 and 934 – "dune covered mounds"  
281 on Fig. 2). There are four mounds with dune partial cover, including one in crater 503, Louth.  
282 In all cases dune patches coincide with the topographic high and only in the cases where  
283 there is complete dune cover do the dunes ingress into the moat. Despite the different levels  
284 of dune cover the mounds share the following morphological characteristics (Fig. S1): flat or  
285 gently sloping summit, asymmetrical placement and a partial or complete moat separating  
286 the mound from part or all of the crater wall.

287 At the scale of MOLA resolution (~230 m) the mounds are smooth (except where dunes are  
288 present, Fig. 3) and gently domed, with maximum local slopes of up to 34° and a half-range  
289 modal slope for all the mounds of 0.9° (mean of 3.6°). Mound relief ranges from 103 m  
290 to 1818 m above the current crater floor and mounds extend to within 13 – 1388 m below the  
291 crater rim, filling their host to 9 – 89 % of current crater depth from rim to floor (Table 1).  
292 Pole-centered, radial swath profiles including the craters containing mounds illustrate the  
293 local penetration depths of these craters into the crust and the relative heights of the mound  
294 summits (Fig. 4). The longitudinal extent of the swaths was chosen to minimize the  
295 longitudinal variation in elevation, so the penetration depth of the craters can be clearly  
296 seen. Figure 4 shows that the craters with mounds tend to be within the craters that  
297 penetrate to the deepest level for a given latitude and longitude region, but also that not all

298 of the deeply penetrating craters have mounds. This figure also demonstrates that there is  
299 no characteristic height up to which the mounds extend vertically.

300 Estimates of maximum ice thickness range from 94 to 1890 m with a mean of 605 m, and  
301 mound volumes range from 0.8 to 3850 km<sup>3</sup>, with a mean of 315 km<sup>3</sup> (Table 1 and Fig. 5).  
302 Our volume estimates are higher than those calculated by Garvin et al. (2000) for the largest  
303 craters. For example Garvin et al. (2000) listed volumes of 1356 and 463 km<sup>3</sup> for the infill of  
304 Korolev and Dokka, respectively and our corresponding estimates are 3850 and 1320 km<sup>3</sup>  
305 (Table 1). The discrepancy can be accounted for by the difference of methods used in this  
306 study and that of Garvin et al. (2000). Garvin et al. (2000) used single MOLA profiles to  
307 determine a polynomial fit to the cavity interior and constrained the predicted depths using  
308 empirical relationships between depth and diameter derived from 109 craters in the region.  
309 We used all available MOLA data to provide information on the cavity shape and did not  
310 constrain the crater depth.

311 Mounds are either completely or partially surrounded by a moat. Similar moats have been  
312 found around concentric crater fill (CFF) near the Martian dichotomy boundary (Levy et al.,  
313 2010). However, CFF is flat-topped, rough at MOLA resolution (~ 20-80 m of relief) and has  
314 not been found to extend above ~450 m below the crater rim. Westbrook (2009) described  
315 75 craters in the south polar region, which also contain mounds. These mounds are similar  
316 to those described here in that they have a flat top, a distinct bounding slope (a moat), are  
317 often offset from the crater center, 35 of them have exposed ice and layers and 17 are  
318 topped by sand dunes. Notable differences include: the south polar mounds often have a  
319 bounding ridge encircling their flat top, some exhibit flow features, some have multiple  
320 superposed mounds, they are found down to lower latitudes (60.8°S) and their host craters  
321 are larger (diameters range from 18.6 to 114.1 km, mean 45.1 km). With the exception of the  
322 southern polar craters, mounds such as the ones described here have not been reported  
323 elsewhere on Mars.

## 324 **3.2 Mound composition results**

325 Spectral data acquired by OMEGA (Fig. 6) show that there are very high water-ice  
326 concentrations (up to ~0.7 band depth) at the surface of the mounds in Korolev (206), Dokka  
327 (388), Louth (503) and unnamed craters 544 and 579. The CO<sub>2</sub> ice signal of from the  
328 2.35 µm band depth is less than 0.2, hence at the limits of the detection using this method.  
329 This indicates that the mounds are predominantly composed of water ice, similar to the  
330 inferred composition of the north polar cap (Bibring et al., 2005). The other mounds in our  
331 survey are too small to be resolved in low resolution OMEGA tracks and are not covered by  
332 high resolution tracks. Where possible we have used CRISM targeted images to investigate  
333 the composition of the mounds. For seven of the craters CRISM targeted images were not  
334 available in the summer season, or of insufficient quality (obscured by clouds or other  
335 atmospheric phenomena). Mounds that are completely covered in dunes had no discernible  
336 water ice signal during northern summer. Instead their spectra resembled those of  
337 background dust. For two mounds with partial dune cover (craters 663 and 769), a weak  
338 water ice signal was detected in high albedo patches, but this signal was not significantly  
339 stronger than that of the surrounding plains or crater interior. For crater 769 in particular the  
340 spectra across both available images (FRT0000b546 and FRT0000cf48) were dominated by  
341 dust, possibly due to the occurrence of small dust storms before these spectra were taken.  
342 These storms were observed in Mars Color Imager (MARCI) images (Malin, et al., 2008.  
343 MRO MARCI Weather Report for the week of 30 June 2008 – 6 July 2008. MSSS-40,  
344 [http://www.msss.com/msss\\_images/2008/07/09/](http://www.msss.com/msss_images/2008/07/09/) and MRO MARCI Weather Report for the  
345 week of 13 October 2008 – 19 October 2008. MSSS-55,  
346 [http://www.msss.com/msss\\_images/2008/10/22/](http://www.msss.com/msss_images/2008/10/22/)). However, by inspecting the map of  
347 surface water ice abundance of Brown and Calvin (2010) derived from analysis of CRISM  
348 mapping data, we were able to confirm the presence of water ice in craters:332, 515, 577,  
349 663, 697 and 795, whereas 436, 480 and 769 had no water ice signal.



350 Spectral instruments (such as OMEGA and CRISM) can only penetrate the optical surface  
351 and give information on the composition of the top few microns of the substrate in the case  
352 of rock or dust, and the top few centimeters in the case of ice (Brown et al., 2010). Hence  
353 the signals that we have observed could be from a thin surface veneer. However, other lines  
354 of evidence support the hypothesis that the mounds are composed of a substantial thickness  
355 of water ice, notably radar and stratigraphic arguments presented in Section 3.3 and also  
356 thermal arguments in Section 4.5.1. Having confirmed the presence of water ice in eleven of  
357 the crater mounds and having found striking morphometric similarities in all 18 mounds,  
358 including craters completely covered by dunes, we propose that all these mounds have a  
359 similar composition.

### 360 **3.3 Mound structure and stratigraphy**

361 Visible layering is common but not universal in mound deposits. It is picked out by reflectivity  
362 contrasts, probably due to differences in dust and/or frost concentration, or different  
363 resistance to erosion. Layers intersect the mound surface, forming contours on the gentle  
364 surface slopes, and outcrop geometries suggest that layering persists at depth within the  
365 mounds. We have mapped and measured spacing between layers on six crater mounds,  
366 three with partial dune cover and three without cover (Fig. 7). In addition, we have observed,  
367 (but did not measure) layers in mounds in craters 697, 795, 544 and 577 located in close  
368 proximity to the polar cap. Layers were not observed in craters 934, 904, 882 814, 811 and  
369 480, where mounds are entirely covered by dunes. Crater 515 has no dunes, but no layers  
370 were observed, as in crater 436 which has partial dune cover. We have also found layering  
371 in a small mound in crater 332 (Fig. 2), which was excluded from our survey, because the  
372 mound does not have sufficient relief (> 150 m) to allow us to reliably distinguish it from a  
373 dunefield, a criteria set out in our mound identification in Section 2.1.

374 Interior layering of mounds is exposed in areas with erosion. These areas are systematically  
375 positioned on the south and east facing slopes of mounds (Fig. 7) and usually on the steeper

376 than average slopes. These zones spatially overlap with significant proportions of water ice  
377 in Fig. 6, in particular zones with water ice band depth > 0.7 water ice in Korolev (206),  
378 Dokka (388) and crater 579. This strongly suggests water ice is the principal component in  
379 the subsurface. We have estimated the thickness of 1438 layers in the six crater mounds  
380 with extensive exposures. Where CTX images were used, HiRISE images within the same  
381 scene were used to confirm that layers thinner than those easily visible in the CTX images  
382 were not present. Layer thickness ranged from 0.007 to 12 m, with an average of 0.42 m and  
383 a standard deviation of 1.55 m (Fig. 8). The layering observed in HiRISE images of the  
384 mound in Louth crater (503) is much finer than in all other mounds (median 0.15 m). In all  
385 cases apart from the fine-scale layering in Louth crater (503) layers are laterally continuous  
386 on scales of 100-1000 m.

387 Dips and strikes of layers were measured at 35 locations within mounds with extensive  
388 exposures (Fig. 7). Measured dips range up to 20° with a mean of ~ 5°. This is consistent  
389 with the distribution of surface slopes at sites with layer exposures (Fig. 9), with a mean of  
390 4.4° and a maximum of about 20°. The difference between layer dip angles and surface  
391 slope at any given location ranges from 0 to 9°, with a mean of 2° and little skewing. This  
392 implies that the dip of the layers could be explained by draping of a topography similar to  
393 that of the present day outcrop sites. Figure 10 shows a detailed example of the interaction  
394 of layers with topography, highlighting that the dip directions are robust, even if the  
395 measured angles are subject to uncertainty (see Section 2.3 for a detailed discussion). The  
396 patterns of layer orientation are similar in all the mounds: strike orientations are similar to  
397 those of the present surface with dip directions away from the top of the mound and in some  
398 cases sub-parallel to crater-rim interior slopes. In all mounds with extensive exposures,  
399 layering is disrupted by unconformities. As an example, Fig. 10 shows unconformities  
400 observed within the mound in crater 579. Younging of these deposits towards the top of the  
401 mound can be inferred from the truncation of layers that are located stratigraphically below  
402 truncating layers (e.g., layer packet A (below) is truncated by layer packet B (above) in Fig.

403 10). Unconformities were also observed in Louth crater (503) with the same apparent trend.  
404 Although the younging directions are similar for coarse and fine-scale layering in this crater,  
405 exposures of the two layer types are separate. Hence, we cannot tell if the fine layered  
406 deposits are located stratigraphically beneath (i.e. older), or above (i.e. younger) the coarse  
407 layered deposits. The fine-scale layers in Louth (503) pinch out laterally on the scale of  
408 meters and have frequent discontinuities, which we interpret as evidence of small-scale  
409 topographic drape. Recent wind erosion of these layer outcrops has caused the formation of  
410 sharp, irregular groves or sastrugi (previously noted by Brown et al., 2008), draping of which  
411 would give rise to the observed stratigraphy.

412 SHARAD radar data shows that the layered structure of mound deposits extends deeper into  
413 the subsurface. We have found internal structures in the mounds of Korolev (206) and  
414 Dokka (388) craters. Verified with clutter simulations, radargrams of the interiors of these  
415 craters (e.g., Fig. 11) indicate that the main stratigraphy follows the contours of the present-  
416 day mounds. Layer thinning is observed on the gently dipping south facing slope in Korolev  
417 (Fig. 11). Layers deeper in the mound interior have a lower dip for both craters, but are more  
418 undulating in the case of Korolev. The following vertical measurements are directly  
419 dependent on the assumed permittivity, as we have chosen pure water ice they are  
420 maximum estimates (lower water ice contents would give reduced lengths). The minimum  
421 spacing between reflectors in the radargram for Korolev is estimated to be 6-18 m with  
422 approximately ~ 20 distinct reflectors visible over a thickness of ~ 2.5 km. The reflectors  
423 picked up by radar instruments, such as SHARAD are generally acknowledged to delineate  
424 packets of layers (Phillips et al., 2008; Putzig et al., 2009), rather than individual beds. The  
425 last return corresponds to ~ 3.9 km below the rim for Korolev, which compares favorably to  
426 the estimated depth of ~ 2.9 km from the relationships of Garvin et al. (2000) and 3.1 km  
427 from our results, implying that the permittivity of the mound material does not differ much  
428 from that of water ice, as was assumed in the depth correction. Thus, the SHARAD data

429 confirms that layering continues throughout the mound, and that the layered material is likely  
430 to consist mainly of water ice over the entire depth of fill.

431 Other, smaller crater mounds did not produce internal radar reflections, probably because  
432 they do not contain sufficiently continuous layering or sufficiently strong dielectric contrasts.  
433 In the along and across track directions reflectors must be at least 300-1000 m and 1500-  
434 8000 m long, respectively, to produce a strong radar return (Alberti et al., 2007). The mound  
435 in crater 579 is likely to be sufficiently large to allow radar detection of internal structures, but  
436 it had no SHARAD coverage, at the time of writing.

437 Given that layering appears to be pervasive within the mound deposits, we can surmise that  
438 mound patches without exposed layering in Fig. 7 represent areas with present-day  
439 deposition of water ice.

#### 440 **4. The origin and evolution of the crater-mounds**

441 Eleven, possibly eighteen intermediate and large impact craters at high northern latitudes on  
442 Mars have interior mounds consisting mainly of water ice. These ice-filled craters are some  
443 of the deepest depressions in their surroundings. The mounds have a smooth, convex-up  
444 shape, often asymmetrically placed within their crater and inclined to the south, surrounded  
445 by a distinct moat. They have internal layering with unconformities indicating upward  
446 younging of deposits and an alternation of phases of deposition and erosion. Layers appear  
447 to drape over the extant topography of the mounds. This layering may be pervasive down to  
448 the base of the deposits where they rest on the crater floor. Any explanation of the origin  
449 and evolution of the crater mounds must address these key features. In this section we  
450 consider four distinct scenarios of mound formation after a brief exploration of controls on  
451 the present day geometry of the mounds.

## 452 **4.1 Present-day form**

453 The surface form and position of the mounds inside the craters may be determined by the  
454 mechanism that drives mound formation, or it could be due to subsequent processes  
455 changing the initial shape of the deposit. Only in the former case does the mound geometry  
456 contain information about the formative mechanism. Therefore we consider briefly whether  
457 post-depositional erosion alone can account for the mound shape. Using a radiation balance  
458 approach, and including effects of shadowing caused by the crater walls, atmospheric  
459 scattering, temperature-dependent re-radiation from the surface and conduction, Russell et  
460 al. (2004) have demonstrated that a north-south asymmetry and an exterior moat can be  
461 developed from an initially flat ice body inside a crater over limited time under current orbital  
462 configuration. They showed that any east-west asymmetry cannot be produced from  
463 radiation alone, but could be explained by aeolian processes, as winds coming off the cap  
464 are deflected longitudinally by planetary vorticity. Figure 12 shows the asymmetrical  
465 placement of the mounds within our studied craters. Mounds proximal to the cap have a  
466 westward displacement from the crater center and this matches the prevailing easterly wind  
467 direction as indicated by dune slip faces (Tanaka and Hayward, 2008). Mounds closer to the  
468 cap tend to be more asymmetric than those further away. These observations suggest that  
469 these mounds are primarily shaped by the wind, which is known to be stronger near the cap  
470 (e.g., Howard, 2000). Further away from the cap the mounds are placed obliquely or  
471 orthogonal to the prevailing wind, suggesting a stronger influence of radiation. The  
472 orientation of mound patches with exposures of internal layering in six of the craters (Fig. 7)  
473 matches this explanation. Dominance of south-facing layer exposures can be attributed to  
474 directionality of incident radiation, and east- or west-facing exposures can be related to  
475 regional winds. Together the asymmetry of the mounds and the orientation of layer  
476 exposures suggest that radiation-driven ablation and wind work together (with different  
477 relative magnitudes) to shape the existing ice deposits. This likely obviates the need to

478 invoke a primary formation mechanism to explain the present-day large-scale morphology of  
479 crater mounds.

## 480 **4.2 Remnant of a more extensive polar cap**

481 As a first possible scenario of mound formation it has been proposed that the interior mound  
482 of Korolev and similar features elsewhere could be erosional remnants of a formerly more  
483 extensive polar cap (Fishbaugh and Head, 2000; Garvin et al., 2000; Tanaka et al., 2008),  
484 along with outliers such as Olympia Mensae. Specifically, Tanaka et al. (2008) have  
485 suggested that the Korolev deposit and those similar to it could be related to stratigraphic  
486 unit "ABb1", the Polar Layered Deposits (PLD). A previously larger extent of the cap  
487 (including the PLD and the Basal Unit beneath) is surmised based on the large erosional  
488 scarps at the current margins of the cap, however the precise spatial extent is not known.  
489 With reference to the position of outliers, Fishbaugh and Head (2000) and Johnson et al.  
490 (2000) have proposed that the cap extended symmetrically down to 80-75°N. Rodríguez et  
491 al. (2010) have argued that an extension of the PLD down to ~ 60°N and subsequent retreat  
492 could account for the distribution of Late Amazonian pedestal craters. If the polar cap was  
493 more extensive, then there is general agreement that it must have occurred under higher  
494 obliquity conditions than at present (which favors migration of ice to lower latitudes), but the  
495 exact timing is debated.

496 The PLD was laid down in the Amazonian as sub-horizontal layers from regular (possibly  
497 seasonal) cycles of atmospheric deposition of water-ice mixed with small and variable  
498 amounts of dust, producing regularly spaced layers with differing albedo of meter to tens of  
499 meters in thickness. Layers are extremely laterally continuous (e.g., Fishbaugh and  
500 Hvidberg, 2006) and angular unconformities occur mainly in association with the spiral  
501 troughs (Putzig et al., 2009; Smith and Holt, 2010; Tanaka et al., 2008). These layers are  
502 observed to generally dip at less than 1° from image (Milkovich et al., 2008) and SHARAD  
503 radar data. Even layers draping trough walls do not have dips in excess of 1° (e.g. Fig. 3e of

504 Smith and Holt, 2010). The maximum total deposit thickness is estimated to be 1800 m from  
505 MARSIS radar data (Selvans et al., 2010). These deposits are thought to provide a record of  
506 past climate, similar to the polar ice caps on Earth (e.g., Cutts 1973; Laskar et al., 2002;  
507 Milkovich and Head, 2005; Milkovich et al., 2008). Estimates of past accumulation rates are  
508 on the order of 0.5 mm/yr (e.g., Laskar et al., 2002), or lower (Perron and Huybers, 2009).  
509 The modern polar cap is undergoing both accumulation, as shown by the burial of craters in  
510 fine-grained ice (Banks et al., 2010) and the lack of dust accumulation on its surface, and  
511 erosion, as shown by the exposure of coarser grained ice with lower albedo at scarps  
512 (Langevin et al., 2005).

513 Underlying a large part of the PLD is the Basal Unit (BU) or Planum Boreum Cavi unit  
514 (ABbc) using the nomenclature of Tanaka et al. (2008). This unit is characterized by a lower  
515 albedo compared to the PLD and is inferred to be rich in sandy material containing a variable  
516 quantity of volatiles. Layers have variable regularity and cross-bedding and a thickness up to  
517 decameters (Herkenhoff et al., 2007). Layers can be laterally discontinuous particularly on  
518 the 100 m scale with frequent angular unconformities. Lighter-toned layers are more  
519 resistant and thought to be more ice-rich. The BU is hypothesized to be of Middle to Late  
520 Amazonian age, originating from aeolian deposition, sometimes in the form of ice-cemented  
521 dunes. The dip angle of these layers has not been measured, but cross-bedded layers are  
522 locally steeper than strata of the PLD. The maximum deposit thickness is estimated to be  
523 1100 m from MARSIS data (Selvans et al., 2010). It is possible that the BU, like the PLD has  
524 been more extensive in the past.

525 If the mounds in our study are remnants of a larger, continuous polar deposit then they might  
526 be expected to have a similar stratigraphy. Measured layer thicknesses on the mounds are  
527 generally within the range reported for the PLD (Milkovich et al., 2008). According to our own  
528 assessments of ~ 350 layers over three outcrops (see Section 2.3 for details) the PLD have  
529 layer spacing of 0.5 to 40 m with a median of 4.7 m and BU between 0.05 and 7.0 m with a

530 median of 1.4 m, presenting no statistically significant difference with layering in crater  
531 mound deposits (Fig. 8). The only exception is the fine-scale layering found in the central  
532 part of the mound in Louth crater (503), which is significantly and consistently finer than  
533 layers measured anywhere else. However, the frequency of discontinuities (e.g. Fig 10) in  
534 the mounds in general seems to be greater than within the PLD (where they are rare). This  
535 implies that the mounds have experienced more erosive episodes. In addition, mound  
536 layering is laterally less continuous, but this could be due to limited exposure compared to  
537 the polar cap. Layer dip angles in the mounds are up to 20°, which is much greater than the  
538 ~1° dips measured by Milkovich et al. (2008) for the PLD. Moreover, it would be expected in  
539 the case of PLD-like deposition that layers should drape the crater walls, dipping gently  
540 towards the center of the crater, with a flat lying central part as observed for craters  
541 emerging from the polar cap (see Fig. 4 of Rodríguez et al., 2010). This contrasts with the  
542 observed outward dip of mound layers that extends into the mound interior, indicating growth  
543 from a central core (Figs. 7, 11).

544 Preservation of the mounds in crater interiors during cap-retreat has been attributed to the  
545 shielding effect of the crater geometry (Garvin et al., 2000). For a given crater  
546 depth/diameter ratio, then, the ice preservation rate should depend to a degree on the  
547 radiation regime which changes with latitude. Confirmation of this link comes from the south  
548 polar region, where the volume of ice bodies inside craters has been observed to decrease  
549 away from the pole (Russell et al., 2003). However, there exists no such relationship either  
550 between the mound volume as a proportion of the total cavity volume (a least squares linear  
551 fit gives  $R^2$  of 0.302 and p-value of 0.011), or the absolute mound volume and distance from  
552 the polar cap in the northern hemisphere ( $R^2$  of 0.058 and p-value of 0.806). This could  
553 indicate a) a different origin for the mounds in the south compared to the north, or b) different  
554 environmental factors determining mound survival between the two hemispheres (e.g.,  
555 geometric shielding is less important than, for example, wind patterns in the north).



556 On balance we feel that stratigraphic, structural and volumetric evidence are not compatible  
557 with the theory that crater mounds distal from the current polar cap formed as part of a larger  
558 contiguous PLD or BU deposit. In particular this applies to Louth (503), Dokka (388), Korolev  
559 (206), craters 579, 663 769 and 436, but we cannot rule out the role of a slightly more  
560 extensive polar cap in the formation of mounds located proximal to the present-day polar cap  
561 deposits.

### 562 **4.3 Impact-driven water release**

563 Our second scenario involves the mobilization of water from permafrost. It has been  
564 hypothesized that relatively long-lived hydrothermal systems could be driven by the heat  
565 released by a meteorite impact (Abramov and Kring, 2005; Osinski et al., 2005; Rathbun and  
566 Squyres, 2002), or that the seismic energy of an impact can mobilize water/permafrost  
567 (Harrison et al., 2010). This mechanism was suggested for the formation of a channeled  
568 scabland extending from the ejecta blanket of Lyot crater located at 55°N, 330°W and a  
569 band of paleo crater lakes (El Maarry, et al., 2010), both south of our study area. The  
570 northern plains region of Mars should be particularly susceptible to the mobilization of  
571 ground ice as it is abundant in the shallow sub-surface. The possibility of impact-induced  
572 hydrothermal systems in permafrost-rich ground on Mars was first suggested by Brakenridge  
573 et al. (1985). In this process the impact melt sheet of larger impact craters contains sufficient  
574 heat energy to melt the surrounding permafrost and water contained in topographic highs  
575 drains into the crater hollow. The resulting lake freezes at the surface, retarding evaporative  
576 loss. Additional water can be sourced from subsequent hydrothermal circulation, driven by  
577 temperature gradients within the surrounding regolith, which draws water into the crater  
578 interior. Once the system has cooled sufficiently water starts to drain downwards out of the  
579 crater lake and eventually a frost front may propagate upwards from the subsurface, leaving  
580 a solid body of ice in the crater interior.

581 Rathbun and Squyres (2002) have shown that impacts creating craters with a diameter less  
582 than 7 km have insufficient energy to sustain a crater lake. This cut off is relatively close to  
583 the observed lower diameter limit for craters with mounds of ~ 9.5 km. For larger craters, the  
584 presence or absence of a mound should then depend on the time since impact, and we  
585 would expect to find mounds preferentially in the youngest craters. At received cratering  
586 rates (e.g., Hartmann and Neukum, 2000), over our study area (excluding the area of the  
587 cap), an impact such as Dokka (51 km diameter) could be as old as several hundreds of  
588 millions of years and Korolev (80 km) over 1 Ga. It is unlikely that relatively small ice bodies  
589 would have survived for this length of time, especially given that the polar cap is believed to  
590 be no older than 4-5 Ma (e.g. Levrard et al., 2007). There are not sufficient craters in this  
591 size range without a mound to confirm, or refute the impact heat theory, although we note  
592 that Lyot crater, a large, 215 km diameter crater just south of our study area, has no  
593 evidence of water ponding in its interior either as a mound, or a desiccated lake (Harrison et  
594 al., 2010; Russell and Head, 2002).

595 In this scenario mound size should have no particular spatial trend, assuming that the same  
596 amount of sub-surface water is available throughout the polar region, but depend primarily  
597 on the energy of impact. As crater diameter is a proxy for impact energy, we might expect it  
598 to scale with the mound volume (an approximation of the amount of water released).  
599 Although the percent of the crater cavity in-filled by the mound does not correlate well with  
600 the diameter of the crater, the absolute volume of infill increases with the crater diameter,  
601 apparently as a power law with the form  $(0.04 \pm 0.09) D^{2.8 \pm 0.2}$  with an  $R^2$  of 0.983 and a p-  
602 value of  $9.6 \times 10^{-11}$  where the uncertainty attached to the estimation of mound volume has  
603 not been taken into account. However, the hydrothermal system is unlikely to have sustained  
604 a hydraulic head permitting significant flow above the plains surrounding impact craters. In  
605 fact, Rathbun and Squyres (2002) estimated a lake depth of 300 m for a 7 km diameter  
606 crater and of ~ 1 km for a 180 km diameter crater (which is almost twice the diameter of  
607 Korolev 206). Several craters in our survey have mounds that significantly exceed these

608 values. Additional elevation of the mounds (of up to 0.5-0.8 km in some cases) would have  
609 to be accounted for, for example by invoking frost-heaving processes active in the waning  
610 period of hydrothermal activity, similar to pingo formation on Earth, as suggested by  
611 Sakimoto et al. (2005) and Bacastow and Sakimoto (2006).

612 It is perhaps most difficult to reconcile our observations of mound deposit stratigraphy with  
613 the requirements of the scenario of impact-driven water release. Creation of the mounds by  
614 this mechanism implies that the mounds have geologically the same age as the impact that  
615 created their host crater, and are formed in a single event. Moreover, the mechanism could  
616 give rise to complex, out-of-sequence layering as periods of hydrothermal injection into an  
617 ice covered lake should cause under-plating and thermal erosion, similar to that of aufeis  
618 (Gillespie et al., 2005). This could be followed by freezing of the water from both the top and  
619 the bottom, producing frost-heave features, folding and faulting when the hydrothermal  
620 system wanes. Water circulated through the subsurface at high temperatures may also  
621 contain impurities consisting of salt and sediment that could be frozen into the deposits.  
622 These expected characteristics contrast with our observation of regular, upward younging  
623 layers of relatively pure ice, without major faults, or folds. In Louth crater (503) small-scale  
624 layering has more folds, but is still relatively regular. Finally, the pervasive presence of large-  
625 scale discontinuities in the mound deposits suggests an evolution involving multiple events.  
626 This, and lack of correspondence with proposed crater lake dimensions are all problems for  
627 this mechanism.

#### 628 **4.4 Artesian flow**

629 The third scenario of mound formation appeals to the presence of deep-seated faults below  
630 impact craters (e.g., Christeson et al., 2001). These faults could tap into a deep aquifer  
631 confined by the cryosphere that is hypothesized to underlie the north polar plains (as  
632 predicted by Clifford, 1993; Clifford and Parker, 2001; Clifford et al., 2010), providing a  
633 conduit to the surface for the confined water. Water would come to the surface at times

634 when the cryosphere enlarges and impinges on the aquifer producing sufficient confining  
635 pressure. This mechanism has been proposed for the creation of crater lakes at lower  
636 latitudes by Newsom et al. (1996). Upwellings would not necessarily occur at the same time  
637 as the impact event and could occur many times, producing a layered stratigraphy as  
638 observed. Assuming that the top of the aquifer is located on a single level, then mounds  
639 should be found in large craters with large fault systems, but also smaller craters located on  
640 low-lying topography. Our results show this trend, where mounds are found in craters which  
641 tend to penetrate to the deepest local elevation (Fig. 4). If the aquifer is fully connected and  
642 the mounds formed at the same time then the mounds should extend up to a similar  
643 topographic elevation, equal to the hydraulic head. This is not the case. If flow rates are low,  
644 then it might be expected that smaller mounds should be found in craters with a base  
645 located at higher absolute elevation. We do observe a very weak negative relationship  
646 between the inferred elevation of the crater base and both relative (linear) and absolute  
647 mound volume (exponential), with  $R^2$  values of 0.006 and 0.37 respectively and p-values of  
648 0.31 and 0.003 respectively.

649 As in the hydrothermal hypothesis mound formation would involve processes akin to those  
650 occurring in pingos. This, together with wind and/or radiation ablation could give rise to  
651 doming of the mounds. The internal stratigraphy of such mounds should be complex. Water  
652 could pond on the surface and gradually freeze as a lake system, or could inject underneath  
653 pre-existing ice. Subsequent pulses would deform, fracture and fold, possibly under-plating  
654 the roof, or breaking through to the surface, filling topographic hollows. Potentially the age of  
655 the ice could increase, or decrease towards the center, depending on the dominant  
656 emplacement mechanism. Ice interior to the mounds should have many discontinuities, folds  
657 and faults. Such complexity is not characteristic of the mounds in our study, which display  
658 regular layering, large-scale discontinuities, minor folding and no faulting. The fine-scale  
659 layering in Louth crater (503) is the only example that shows sufficient complexity to fit with  
660 this model, but it is the exception, rather than the rule. Interestingly, the mound in that crater

661 is placed very eccentrically, as would be expected from the peripheral position of impact fault  
662 systems. However, neither there nor elsewhere have we found spectroscopic evidence for  
663 the presence of salts in mound deposits, which is expected for upwelling water sourced at  
664 depth. In addition, there appears to be a discrepancy between the observed distribution of  
665 crater mounds and the geometry of the putative deep aquifer (Clifford, 1993). The aquifer is  
666 thought to be located deepest close to the polar cap, where surface temperatures are  
667 lowest, but there we have found mounds in several craters of limited diameter and depth. It  
668 is possible that the aquifer is located at shallower depths than proposed by Clifford (1993)  
669 very near to the pole, due to water being supplied from the base of the polar cap (e.g.,  
670 Longhi, 2006). Away from the polar cap, the cryosphere is thought to thin southward, making  
671 mound or lake formation more likely in this scenario. The lack of evidence for hydrological  
672 activity in Lyot crater (Russell and Head, 2002; Harrison et al., 2010) is at odds with this  
673 expectation. Despite the mounds occurring in the deeper penetrating circumpolar craters,  
674 inconsistencies in stratigraphy, composition, position and distribution argue against artesian  
675 flow from a deep aquifer as a formative mechanism for these mounds.

## 676 **4.5 Crater microclimate**

677 Our fourth hypothesis calls on microclimate phenomena associated with crater topography  
678 for growth of ice mounds from atmospheric deposition. We start our exploration of this  
679 mechanism with some observations of temperature and albedo in and around craters in the  
680 north polar region.

### 681 **4.5.1 Craters as cold traps**

682 The temperature and albedo evolution of ice mounds in Korolev and Dokka through the  
683 Martian year have been reported by Armstrong et al. (2005) and Kuti (2009). These mounds  
684 are consistently ~ 10 K cooler than ice-free terrain at the same latitude for most of the year,  
685 with an accentuated daytime difference of ~20-40 K in summer months (Fig. 13). On these

686 crater mounds, surface temperatures remains close to the water frost point throughout the  
687 year (particularly at night). In other craters without ice (an example is given in Fig. 13),  
688 temperatures inside and outside the craters are very similar for most of the year. These  
689 observations suggest that the presence of ice modulates local near surface temperatures in  
690 crater interiors. A minimum thickness of ice of several meters at the surface may be required  
691 to produce this effect (Armstrong et al., 2005). So how did this initial ice layer come about in  
692 the craters with mounds, and how and when does/did this volatile deposition occur?

693 The following thermal, spectral and image data reveal that crater cavities may enhance the  
694 deposition and/or preservation of volatiles at the present day. Viking Infrared Thermal  
695 Mapper (Kieffer 1977) and Thermal Emission Spectrometer (TES; Titus et al. 2001)  
696 observations have shown temperatures below the CO<sub>2</sub> sublimation point inside craters  
697 during winter. These cold spots are unlikely to represent real surface temperatures, but  
698 could be caused by cloud formation and thus possibly increased deposition of CO<sub>2</sub> ice  
699 (Ivanov and Muhleman, 1999). In agreement with these observations, we also observe that  
700 apparent crater floor temperatures with and without ice mounds are up to 10°K below those  
701 outside the crater between  $L_s = 240-320^\circ$  (Fig. 13).

702 We have examined published OMEGA data (Appéré et al., 2011) and HiRISE and CTX  
703 images for presence of surface ice at latitudes greater than 60°N around the  $L_s = 60^\circ$  crocus  
704 date, when CO<sub>2</sub> frost is receding. The OMEGA data show that crater floors remain covered  
705 in water ice for approximately 5° of  $L_s$  after the main seasonal cap has retreated to higher  
706 latitudes (Figures 5-8 Appéré et al., 2011). These deposits then degrade to an annulus  
707 around the crater rim, before disappearing. HiRISE and CTX images show that crater floors  
708 rarely have any remnant high albedo ice deposits after the crocus date. They do show,  
709 however, that high albedo patches remain after the crocus date on north-facing crater slopes  
710 (Fig. 14B) and sometimes as E-W 'plumes' outside the crater (Fig. 14A). Many of these  
711 patches disappear in the summer, but some remain as shown in CRISM analyses performed  
712 by Seelos et al. (2008). These authors have hypothesized that the 'plumes' are a result of

713 wind-driven, orographic deposition of water ice. Hajigholi et al. (2010) monitored seven  
714 craters at  $> 55^{\circ}\text{N}$  and also noted crater interiors were favored sites for ice deposition. These  
715 observations show that crater floors are not presently sequestering  $\text{H}_2\text{O}$  or  $\text{CO}_2$  deposited in  
716 the seasonal polar cap under present day conditions.

717 If atmospheric deposition is the driving process in which layers are constructed, then to start  
718 mound formation, ice build-up in winter months on the crater floor must outstrip sublimation  
719 in spring and summer. The presence of high-albedo ice deposits throughout the year may  
720 then locally suppress near surface temperatures and form a long-lived cold trap for  $\text{H}_2\text{O}$ . It is  
721 possible that the ice layer needed to trigger further build-up is provided by a hydrothermally  
722 induced crater lake, or the remnant of a more extensive cap deposit. Below, we examine a  
723 scenario that does not involve an external start, and is instead entirely climate-driven.

#### 724 **4.5.2 Reduced sublimation of water ice in craters**

725 We have demonstrated that at least seasonally all craters trap water ice. However, this does  
726 not explain why only some craters in the near polar area host mounds and why others do  
727 not. We suggest that this is because of differing preservation potentials between the craters,  
728 which are determined by differing rates of sublimation. Factors, such as shadowing within  
729 the crater, differences in surface thermophysical properties, atmospheric temperature,  
730 atmospheric pressure and the wind regime, play a role in defining the sublimation rate.

731 The higher the surface temperature the more rapid the sublimation, so cooler temperatures  
732 favor the preservation of ice mounds. The surface temperature is controlled by insolation  
733 (and thus shading) and surface thermophysical properties. If we consider shadowing alone,  
734 water ice should be preserved on all north-facing crater walls rather than on crater floors and  
735 mounds should therefore have an off-center nucleus, positioned on the north-facing slope. In  
736 the craters where we have studied the stratigraphy the nucleus of the mound is located on  
737 the crater floor and not all craters have mounds, hence this factor alone does not explain our

738 observations. We cannot determine the surface material albedo and thermal inertia of the  
739 craters prior to mound deposition; hence we cannot definitively say what role these  
740 thermophysical properties played.

741 The atmospheric pressure at the base of a crater is greater than on the surrounding plains  
742 (due to altitude) and this can act to reduce sublimation by free convection (e.g., Ingersoll,  
743 1970). As the mounds are often found in craters that penetrate deeply into the crust (Fig. 4),  
744 this may be one factor that could help to explain the mound distribution. However, other  
745 factors must be playing a role, because not all deeply penetrating craters have mounds.  
746 Wind speed and its saturation level also play a key role in sublimation, with strong, dry winds  
747 enhancing forced sublimation (e.g., Ingersoll, 1970). Given this, it might be expected that  
748 craters with mounds should be located away from the strong summer katabatic winds, but  
749 we observe no systematic placement of craters with mounds with respect to these winds  
750 (see maps in Massé et al. 2012, Ewing et al., 2010 and Howard, 2000). At a smaller scale  
751 craters generate their own wind systems. Fenton and Hayward (2010) noted a peculiar  
752 “bullseye” dunefield morphology in craters close to the southern polar cap, and attributed it  
753 to inward flowing local katabatic winds. We see the same morphology inside many of the  
754 craters with mounds and inside other craters in the area, indicating the strong influence of  
755 local winds. The topography of each crater would have different effects on these wind  
756 patterns, but with the data available we find no systematic pattern to explain why some  
757 craters have mounds and others do not. To precisely determine the role of local-scale winds  
758 in triggering mound formation would require a full meso-scale climate model (e.g. Spiga, et  
759 al. 2011), which is outside the scope of this paper.

### 760 **4.5.3 Initiation and mound building**

761 We envisage the following sequence of events (Fig. 15) for the initiation and evolution of  
762 mound building:



763 1) In winter condensation of water ice is followed by the condensation of CO<sub>2</sub> intermixed with  
764 a smaller fraction of water ice. The microenvironment inside the crater interior causes  
765 additional condensation of volatiles over the winter period, resulting in a thicker layer of both  
766 CO<sub>2</sub> and H<sub>2</sub>O in the crater floor than on surrounding plains.

767 2) The CO<sub>2</sub> layer is first to sublimate in spring. This process is driven by direct insolation, but  
768 also draws heat from the surrounding atmosphere, and this maintains a low temperature in  
769 the crater interiors (~150 K). Simultaneously, water ice is sublimating at lower latitudes and  
770 this water vapor can condense back on to the sublimating CO<sub>2</sub> deposits at higher latitudes  
771 (e.g. Appéré et al. 2011). The thicker layer of CO<sub>2</sub> deposited on the crater floor, and lower  
772 local temperatures cause the crater floor to defrost later than the surrounding landscape.  
773 This means that the process of re-condensation of water vapor can continue for longer and  
774 in particular while H<sub>2</sub>O is sublimating from the landscape immediately surrounding the crater.

775 3) Once the surrounding landscape has completely defrosted and the CO<sub>2</sub> sublimation in the  
776 crater has finished, there remains a layer of water ice condensed over winter and additional,  
777 re-condensed water ice layer.

778 4) The sublimation of this remaining water ice is retarded by the microclimate of the crater  
779 interior (likely pressure and wind effects). Due to the high albedo of the deposit both free and  
780 forced sublimation will also be slowed due to the lower atmospheric temperature above the  
781 deposit (further enhanced if the deposit is thick). A thick layer (with high thermal inertia)  
782 might permit re-condensation during the night if any sublimation has occurred.

783 5) Once a “thick” layer has been built (~1-4 m required according to Armstrong et al., 2005)  
784 this creates a positive feedback, whereby the high albedo and high thermal inertia form a  
785 cold trap which produces net accumulation over the course of a year (Fig. 13). Then, water  
786 vapor delivered to the crater at almost any time of year could freeze onto the existing  
787 deposit, and progressive build-up of an ice mound would ensue.

788 Atmospheric deposition would give rise to upward younging stratigraphy, with regular  
789 layering, reflecting cyclical deposition on seasonal, but more likely much longer timescales.

790 Changes in the balance of deposition and ablation could cause alternation of aggradation  
791 and decay of the deposits, recorded in (angular) unconformities within the mound  
792 stratigraphy. During an initial build up phase, deposits are expected to line the crater interior,  
793 but solar irradiation and directional ablation by winds would eventually cause the formation  
794 of a moat and give the deposit a characteristic mound shape. Further volatile deposition  
795 would drape the mound topography, dipping outward from an accumulation center, and  
796 following any erosional detail in the pre-existing ice surface. All of these expectations are  
797 matched by our stratigraphic observations.

#### 798 **4.5.4 Timing**

799 At present, craters are not initiation points for mound building, nor is mound building very  
800 rapid. Assuming that current maximum deposition rates are similar to those on the north  
801 polar cap, 3-4 mm/yr (Banks et al., 2010), a mound such as the one in Korolev would take  
802 ~ 500 ka to form when deposition is uninterrupted. Orbital forcing of climate is important on  
803 this time scale. Using a global climate model and different orbital parameters Levrard et al.  
804 (2007) showed that obliquity (axial tilt, ~124 ka cycle) is the primary orbital control on ice  
805 accumulation in the polar region. Low obliquity favors polar cap accumulation and obliquities  
806 greater than 30° can destabilize ice in the whole polar region (which last occurred at  
807 ~0.4 Ma). Another important feature is the precession cycle (~51 ka), a combined effect of  
808 the eccentricity and longitude of the perihelion. The orbit of Mars is elliptical, so that northern  
809 hemisphere spring is the longest season, followed by northern summer, winter and the  
810 shortest season is autumn, the present-day location of the perihelion. Thus, northern winters  
811 are comparatively short and warm, and summers are long and cool. If the perihelion is  
812 located in northern summer, then winters become longer cooler and the summer becomes  
813 short and relatively hot. It is the length of the seasons, rather than their relative temperature,  
814 that governs ice accumulation at obliquities less than 25° (Levrard et al., 2004; Levrard et  
815 al., 2007). As the obliquity has been relatively stable over the last 500 ka, precession cycles

816 dominate. We suggest that mound triggering and building may be favored when the  
817 perihelion is located in summer or autumn, allowing a longer period of winter deposition and  
818 a long spring period when volatiles are delivered from the receding seasonal cap and the  
819 main polar deposits. This situation last occurred between 10-25 ka before present  
820 (Montmessin et al., 2007). These cycles could account for the large angular unconformities  
821 that we observe. Further modeling is required to accurately ascertain orbital parameters that  
822 are favorable to mound building.

823 If the mounds are indeed formed by atmospheric deposition, then their overall form and  
824 internal stratigraphy are controlled by climatic conditions. If their timescale of adjustment is  
825 relatively quick compared to the timescale of climate change then they should provide a  
826 stratigraphic record of recent climate changes, driven by changes in Mars' orbital  
827 configuration.

#### 828 **4.5.5 Other ice outliers**

829 We surveyed the outlying high albedo deposits that are not located within craters to  
830 ascertain if there was a common formation mechanism with the mounds inside craters. The  
831 majority of these deposits are mostly thin (they show underlying impact craters of ~ 500 m  
832 diameter with an expected rim height of ~ 25 m) and only around Olympia Mensae (between  
833 ~95-135°E and ~73-80°N, Fig. 2, marked "OM") do they reach thicknesses of > 100 m. The  
834 presence of relatively thin outliers located between Dokka, Korolev and the Olympia Undae  
835 dunefield (between ~150-240°E and ~75-80°N latitude) has been previously attributed to the  
836 presence of polar deposits underlying this area (Fishbaugh and Head, 2000). Tanaka et al.  
837 (2008) classified these high albedo deposits as 'ABb<sub>4</sub>' or Planum Boreum 4 unit, which is the  
838 unit that caps the present polar cap, and suggested that these deposits are recent (last  
839 21.5 ka) and relatively thin. Recent radar data has confirmed that the BU extends beneath  
840 the Olympia Undae dunefield (Selvans et al., 2010), making it quite plausible that thin  
841 deposits extend further north. These high albedo deposits occur where dunes are not

842 present, so it could be that they are accumulations resulting from the exposure and resulting  
843 cold-trap effect of BU deposits.

844 The presence of thicker deposits in the Olympia Mensae area is more difficult to explain.  
845 They occur as discrete patches with steep boundary scarps with up to  $\sim 20^\circ$  slopes and  
846 thickness of up to 350 m, but more generally around 100 m. They are located latitudinally  
847 between and to the east of Louth (503) and crater 579. This area is of relatively high  
848 elevation compared to the same latitude elsewhere around the pole. Three of the outcrops  
849 are elongate in the E-W direction and have layer exposures in all orientations, consistent  
850 with wind erosion rather than radiation as the primary shaping mechanism. The Olympia  
851 Mensae deposits have visually very similar stratigraphy to the crater mounds in terms of  
852 layer spacing and presence of low-angle unconformities, but only have very low dips ( $<1^\circ$ )  
853 and no draping layers (Fig. 16). They have almost 100 % exposure of the layers, which  
854 implies they are currently undergoing retreat. This is supported by Brown et al. (2011), who  
855 suggest that sublimation in the Olympae Mensae region might be the main source of the  
856 water which masks the CO<sub>2</sub> seasonal cap during its spring regression. This suggests these  
857 outliers unlike the crater mounds have not undergone significant recent deposition and  
858 therefore their evolution is somewhat different to that of the ice mounds inside craters. The  
859 questions of how their deposition was triggered and their previous extent are left open as  
860 targets for future investigation.

## 861 **5. Conclusions**

862 We have identified and studied 18 inner-crater mounds in Mars' north polar region that have  
863 an origin different from the central peaks normally found in complex craters. They are  
864 restricted to craters with a diameter  $>9.5$  km located at latitudes  $> 70^\circ\text{N}$ . Two of these crater  
865 mounds consist largely of water ice according to radar data and nine others have substantial  
866 water ice at the surface as observed in spectral data. We infer by similarity of form and  
867 location that the other mounds are also composed of water ice. Their large-scale

868 morphology, flat topped with a circumferential moat, can be explained by ablation of volatiles  
869 by solar radiation and wind, leaving no indication of the formation mechanism.

870 The formation of these mounds by either impact-induced hydrothermal circulation or artesian  
871 upwelling is inconsistent with the generally unfolded and unfaulted, regular layering with  
872 upward younging stratigraphy exposed on mound surfaces. Moreover, ice layers drape the  
873 existing topography on at least six of the mounds, implying growth from a central core. This  
874 is inconsistent with these mounds being erosional remnants of a previously more extensive  
875 polar cap. It is plausible that this form of growth is shared by eight other mounds that are not  
876 directly adjacent to the present polar cap. For the four mounds abutting the present polar  
877 cap we cannot rule out an origin by cap retreat.

878 Ice accumulations can be maintained or grow by cold trapping when they have attained a  
879 minimum thickness required to form a negative thermal anomaly that persists throughout the  
880 year. This minimum condition can be achieved in one of three ways: a frozen paleo-lake  
881 from an impact hydrothermal system, a remnant of a more extensive polar cap, or  
882 atmospheric deposition driven by microclimate processes inside the crater. We have no  
883 observational evidence to support any of these initiation mechanisms, but we have explored  
884 in more detail the possibility that mound formation is entirely due to the microclimatic  
885 characteristics of deep impact craters at high northern latitudes.

886 Mounds are found in deeply penetrating craters where atmospheric pressures are high  
887 compared to the areas surrounding the crater. This suppresses ice sublimation, but not all  
888 deeply penetrating craters have mounds, so other climatic factors, such as wind regime,  
889 must be playing a role. We suggest that microclimatic effects act to suppress the sublimation  
890 of seasonal ice in springtime, both increasing its lifetime and creating a cold-trap onto which  
891 volatiles released from the surrounding landscape during warm seasons can condense. It is  
892 likely that during periods when Mars' orbital perihelion was located in northern summer,  
893 longer winters have allowed enhanced deposition of volatiles, while the potential for  
894 sublimation was limited by the brevity of summers. Under these conditions, which last

895 occurred 10-25 ka ago, enough ice may have built up in deep crater interiors to start a  
896 positive feedback permitting mound building due to the formation of long lived cold trap  
897 above bodies with high albedo and thermal inertia. The main supply of water vapor to these  
898 cold traps may be the seasonal cap with secondary input from katabatic winds flowing from  
899 the polar cap during spring and early summer.

900 Where mound surfaces are not clad by dunes, the fact that layers are seen to be exposed at  
901 the surface indicates recent or ongoing erosion in these areas. However, elsewhere the lack  
902 of visible layering can be attributed to recent deposition of ice draping the mound  
903 topography. Hence, the mounds are currently undergoing change, likely driven by changes  
904 in the local climate. Changes in climate may shift and resize the depositional and erosion  
905 areas, explaining the complex pattern of discontinuities visible in exposed mound  
906 stratigraphy. If this interpretation is correct, then the crater mounds may be sensitive  
907 recorders of climate change in the north polar area, located in closest proximity to the main  
908 source of volatiles on present day Mars. Further investigation of their stratigraphy and  
909 dynamics may yield new insights into the past and present H<sub>2</sub>O and CO<sub>2</sub> cycles of the  
910 planet.

## 911 **Acknowledgements**

912 Firstly we thank Colin Dundas and Adrian Brown for their thorough and thoughtful reviews,  
913 which greatly improved the manuscript. We thank Edwin Kite, Simon Dadson, and Dimitri  
914 Lague for their additions and critique. Additional support provided by the Earth Science  
915 Department at Cambridge University was essential in completing this work. We are indebted  
916 to the late Ali Safaeinili who created the code enabling estimation of the SHARAD time to  
917 depth conversion. Marion Massé provided useful discussion on CRISM and OMEGA  
918 spectral data. Many thanks to Rosalyn Hayward for giving permission to use her data on  
919 dunefields in the north polar region and Lori Fenton for useful discussion regarding bullseye  
920 dunes. Thomas Appéré provided insightful comments on polar seasonal processes.

921 **References**

- 922 Abramov, O., Kring, D. A., 2005. Impact-induced hydrothermal activity on early Mars. J.  
923 Geophys. Res. 110 (E12), doi:10.1029/2005je002453.
- 924 Alberti, G., Dinardo, S., Mattei, S., Papa, C., Santovito, M. R., 2007. SHARAD radar signal  
925 processing technique. IWAGPR 4th International Workshop on Advanced Ground  
926 Penetrating Radar, Naples, Italy.
- 927 Antoniadi, E. M., 1930. La Planète Mars. Herman, Paris.
- 928 Appéré, T., B. Schmitt, Y. Langevin, S. Douté, A. Pommerol, F. Forget, A. Spiga, B. Gondet,  
929 J. P. Bibring (2011), Winter and spring evolution of northern seasonal deposits on  
930 Mars from OMEGA on Mars Express, J. Geophys. Res. 116(E5), E05001,  
931 doi:10.1029/2010JE003762.
- 932 Armstrong, J. C., Titus, T. N., Kieffer, H. H., 2005. Evidence for subsurface water ice in  
933 Korolev crater, Mars. Icarus. 174 (2), 360-372.
- 934 Armstrong, J. C., Nielson, S. K., Titus, T. N., 2007. Survey of TES high albedo events in  
935 Mars' northern polar craters. Geophys. Res. Lett. 34, doi:10.1029/2006GL027960.
- 936 Bacastow, A. L., Sakimoto, S. E. H., 2006. Martian North Polar Crater Morphology:  
937 Implication for an Aquifer. Lunar Planet. Sci. 37. Abstract 2239.
- 938 Banks, M. E., Byrne, S., Galla, K., McEwen, A. S., Bray, V. J., Dundas, C. M., Fishbaugh, K.  
939 E., Herkenhoff, K. E., Murray, B. C., 2010. Crater population and resurfacing of the  
940 Martian north polar layered deposits. J. Geophys. Res. 115 (E8),  
941 doi:10.1029/2009JE003523.

942 Barlow, N. G., Perez, C. B., 2003. Martian impact crater ejecta morphologies as indicators of  
943 the distribution of subsurface volatiles. *J. Geophys. Res. Planets.* 108 (E8),  
944 doi:10.1029/2002JE002036.

945 Barnie, T. D., 2006. Placing constraints on the origin of the ice fill of north polar ice impact  
946 craters on Mars using impact crater and ice fill morphology. Master's Thesis,  
947 University of Aberystwyth, pp. 114.

948 Bibring, J. P., Langevin, Y., Gendrin, A., Gondet, B., Poulet, F., Berthe, M., Soufflot, A.,  
949 Arvidson, R., Mangold, N., Mustard, J., Drossart, P., 2005. Mars surface diversity as  
950 revealed by the OMEGA/Mars Express observations. *Science* 307 (5715), 1576-  
951 1581.

952 Brakenridge, G. R., Newsom, H. E., Baker, V. R., 1985. Ancient hot springs on Mars: Origins  
953 and paleoenvironmental significance of small Martian valleys. *Geology* 13 (12), 859-  
954 862.

955 Brown, A. J., Byrne, S., Tornabene, L. L., Roush, T., 2008. Louth crater: Evolution of a  
956 layered water ice mound. *Icarus* 196 (2), 433-445.

957 Brown, A. J., Calvin, W., 2010. MRO (CRISM/MARCI) Mapping of the North Pole - First  
958 Mars Year of Observations. *Lunar Planet. Sci.* 41. Abstract 1278.

959 Brown, A. J., Calvin, W., McGuire, P., Murchie, S., 2010. Compact Reconnaissance Imaging  
960 Spectrometer for Mars (CRISM) south polar mapping: First Mars year of  
961 observations. *J. Geophys. Res. Planets.* 115, doi:10.1029/2009JE003333.

962 Brown, A. J., Calvin, W., Hollingsworth, J. L., Schaefer, J. R., Michaels, T. I., Mellem, B. A.,  
963 2011. CRISM and MARCI Observations of North Polar Springtime Recession for MY  
964 29/30. . Fifth International Conference on Mars Polar Science and Exploration  
965 Abstract 6060.



966 Boyce, J.M., Mouginiis-Mark, P., Garbeil, H., 2005. Ancient oceans in the northern lowlands  
967 of Mars: Evidence from impact crater depth/diameter relationships. *J.Geophys. Res.*  
968 110, doi:10.1029/2004JE002328.

969 Byrne, S., Dundas, C.M., Kennedy, M.R., Mellon, M.T., McEwen, A.S., Cull, S.C., Daubar,  
970 I.J., Shean, D.E., Seelos, K.D., Murchie, S.L., Cantor, B.A., Arvidson, R.E., Edgett,  
971 K.S., Reufer, A., Thomas, N., Harrison, T.N., Posiolova, L.V., Seelos, F.P., 2009.  
972 Distribution of mid-latitude ground ice on mars from new impact craters. *Science* 325,  
973 1674-1676.

974 Calvin, W. M., Roach, L. H., Seelos, F. P., Seelos, K. D., Green, R. O., Murchie, S. L.,  
975 Mustard, J. F., 2009. Compact Reconnaissance Imaging Spectrometer for Mars  
976 observations of northern Martian latitudes in summer. *J. Geophys. Res.* 114,  
977 doi:10.1029/2009JE003348.

978 Christeson, G. L., Nakamura, Y., Buffler, R. T., Morgan, J., Warner, M., 2001. Deep crustal  
979 structure of the Chicxulub impact crater. *J. Geophys. Res.* 106 (B10), 21751-21769.

980 Clifford, S. M., 1993. A Model for the Hydrologic and Climatic Behavior of Water on Mars. *J.*  
981 *Geophys. Res. Planets* 98 (E6), 10973-11016.

982 Clifford, S. M., Parker, T. J., 2001. The evolution of the Martian hydrosphere: Implications for  
983 the fate of a primordial ocean and the current state of the northern plains. *Icarus* 154  
984 (1), 40-79.

985 Clifford, S. M., Lasue, J., Heggy, E., Boisson, J., McGovern, P., Max, M. D., 2010. Depth of  
986 the Martian cryosphere: Revised estimates and implications for the existence and  
987 detection of subpermafrost groundwater. *J. Geophys. Res.* 115 (E7),  
988 doi:10.1029/2009JE003462.

- 989 Cull, S., Arvidson, R. E., Mellon, M., Wiseman, S., Clark, R., Titus, T., Morris, R. V.,  
990 McGuire, P., 2010. Seasonal H<sub>2</sub>O and CO<sub>2</sub> ice cycles at the Mars Phoenix landing  
991 site: 1. Prelanding CRISM and HiRISE observations. *J. Geophys. Res.* 115,  
992 doi:10.1029/2009JE003340.
- 993 Cutts, J.A., 1973. Nature and origin of layered deposits of the Martian polar regions. *J.*  
994 *Geophys. Res.*, 78, 4231–4249.
- 995 El Maarry, M. R., Markiewicz, W. J., Mellon, M. T., Goetz, W., Dohm, J. M., Pack, A., 2010.  
996 Crater floor polygons: Desiccation patterns of ancient lakes on Mars? *J. Geophys.*  
997 *Res.* 115 (E10), doi:10.1029/2010JE003609.
- 998 Ewing, R. C., Peyret, A.-P. B., Kocurek, G., Bourke, M., 2010. Dune field pattern formation  
999 and recent transporting winds in the Olympia Undae Dune Field, north polar region of  
1000 Mars. *J. Geophys. Res.* 115 (E8), doi:10.1029/2009JE003526.
- 1001 Feldman, W. C., Prettyman, T. H., Maurice, S., Plaut, J. J., Bish, D. L., Vaniman, D. T.,  
1002 Mellon, M. T., Metzger, A. E., Squyres, S. W., Karunatillake, S., Boynton, W. V.,  
1003 Elphic, R. C., Funsten, H. O., Lawrence, D. J., Tokar, R. L., 2004. Global distribution  
1004 of near-surface hydrogen on Mars. *J. Geophys. Res.* 109 (E9),  
1005 doi:10.1029/2003JE002160.
- 1006 Fenton, L.K., Hayward, R.K., 2010. Southern high latitude dune fields on Mars: Morphology,  
1007 aeolian inactivity, and climate change. *Geomorphology* 121, 98-121.
- 1008 Fishbaugh, K. E., Head, J. W., 2000. North polar region of Mars: Topography of circumpolar  
1009 deposits from Mars Orbiter Laser Altimeter (MOLA) data and evidence for  
1010 asymmetric retreat of the polar cap. *J. Geophys. Res.* 105, 22455-22486.

- 1011 Fishbaugh, K. E., Hvidberg, C. S., 2006. Martian north polar layered deposits stratigraphy:  
1012 Implications for accumulation rates and flow. *J. Geophys. Res.* 111 (E6),  
1013 doi:10.1029/2005je002571.
- 1014 Garvin, J. B., Sakimoto, S. E. H., Frawley, J. J., Schnetzler, C., 2000. North Polar Region  
1015 Craterforms on Mars: Geometric Characteristics from the Mars Orbiter Laser  
1016 Altimeter. *Icarus* 144, 329-352.
- 1017 Garvin, J. B., 2005. Impact Craters on Mars: Natural 3D Exploration Probes of Geological  
1018 Evolution. Workshop on the Role of Volatiles and Atmospheres on Martian Impact  
1019 Craters. LPI Laurel, Maryland. Abstract 1273, p.38-39.
- 1020 Gillespie, A. R., Montgomery, D. R., Mushkin, A., 2005. Planetary science: Are there active  
1021 glaciers on Mars? *Nature*. 438 (7069), E9-E10.
- 1022 Hajigholi, M., Bertilsson, S. A. M., Brown, A. J., McKay, C. P., Fredriksson, S., 2010.  
1023 Monitoring Seasonal Behavior of Ices in the Craters in the Martian Northern Polar  
1024 Region with CTX and HiRISE. *Lunar Planet. Sci.* 41. Abstract 1553.
- 1025 Harrison, T. N., Malin, M. C., Edgett, K. S., Shean, D. E., Kennedy, M. R., Lipkaman, L. J.,  
1026 Cantor, B. A., Posiolova, L. V., 2010. Impact-induced overland fluid flow and  
1027 channelized erosion at Lyot Crater, Mars. *Geophys. Res. Lett.* 37 (21),  
1028 doi:10.1029/2010gl045074.
- 1029 Hartmann, W. K., Neukum, G., 2001. Cratering Chronology and the Evolution of Mars.  
1030 *Space Sci. Rev.* 96, 165-194.
- 1031 Herkenhoff, K. E., Byrne, S., Russell, P. S., Fishbaugh, K. E., McEwen, A. S., 2007. Meter-  
1032 Scale Morphology of the North Polar Region of Mars. *Science* 317 (5845), 1711-  
1033 1715.

- 1034 Hovius, N., Conway, S. J., Barnie, T. D., Besserer, J., 2009. Ice Filled Craters in Mars' North  
1035 Polar Region -- Implications for Sub-Surface Volatiles. *Lunar Planet. Sci.* 40. Abstract  
1036 2042.
- 1037 Howard, A. D., 2000. The Role of Eolian Processes in Forming Surface Features of the  
1038 Martian Polar Layered Deposits. *Icarus* 144 (2), 267-288.
- 1039 Ingersoll, A. P., 1970. Mars: Occurrence of liquid water. *Science* 168, 972-973.
- 1040 Ivanov, A. B., Muhleman, D. O., 2001. Cloud Reflection Observations: Results from the Mars  
1041 Orbiter Laser Altimeter. *Icarus* 154 (1), 190-206.
- 1042 Jakosky, B. M., Mellon, M. T., Varnes, E. S., Feldman, W. C., Boynton, W. V., Haberle, R.  
1043 M., 2005. Mars low-latitude neutron distribution: Possible remnant near-surface water  
1044 ice and a mechanism for its recent emplacement. *Icarus* 175, 58-67.
- 1045 Johnson, C. L., Solomon, S. C., Head, J. W., Phillips, R. J., Smith, D. E., Zuber, M. T., 2000.  
1046 Lithospheric Loading by the Northern Polar Cap on Mars. *Icarus* 144 (2), 313-328.
- 1047 Kieffer, H.H., Martin, T.Z., Peterfreund, A.R., Jakosky, B.M., Miner, E.D., Palluconi, F.D.,  
1048 1977. Thermal and Albedo Mapping of Mars During the Viking Primary Mission. *J.*  
1049 *Geophys. Res.* 82, 4249-4291, doi:10.1029/JS082i028p04249.
- 1050 Kreslavsky, M. A., Head, J. W., 2006. Modification of impact craters in the northern plains of  
1051 Mars: Implications for Amazonian climate history. *Meteorit. Planet. Sci.* 41, 1633-  
1052 1646.
- 1053 Kuti, A., 2009. Thermal Behavior of Dokka Crater and its Surroundings in the North Polar  
1054 Region of Mars. *Lunar Planet. Sci.* 40. Abstract 1006.

- 1055 Langevin, Y., Poulet, F., Bibring, J. P., Gondet, B., 2005. Summer evolution of the north  
1056 polar cap of Mars as observed by OMEGA/Mars express. *Science*. 307 (5715), 1581-  
1057 1584.
- 1058 Laskar, J., Levrard, B., Mustard, J. F., 2002. Orbital forcing of the martian polar layered  
1059 deposits. *Nature* 419 (6905), 375-377.
- 1060 Levrard, B., Forget, F., Montmessin, F., Laskar, J., 2004. Recent ice-rich deposits formed at  
1061 high latitudes on Mars by sublimation of unstable equatorial ice during low obliquity.  
1062 *Nature* 431 (7012), 1072-1075.
- 1063 Levrard, B., Forget, F., Montmessin, F., Laskar, J., 2007. Recent formation and evolution of  
1064 northern Martian polar layered deposits as inferred from a Global Climate Model. *J.*  
1065 *Geophys. Res.* 112 (E6), E06012.
- 1066 Levy, J., Head, J. W., Marchant, D. R., 2010. Concentric crater fill in the northern mid-  
1067 latitudes of Mars: Formation processes and relationships to similar landforms of  
1068 glacial origin. *Icarus* 209 (2), 390-404.
- 1069 Longhi, J., 2006. Phase equilibrium in the system CO<sub>2</sub>-H<sub>2</sub>O: Application to Mars. *J.*  
1070 *Geophys. Res. Planets*. 111 (E6), doi:10.1029/2005JE002552.
- 1071 Massé, M., Bourgeois, O., Le Mouélic, S., Verpoorter, C., Spiga, A., Le Deit, L., 2012. Wide  
1072 distribution and glacial origin of polar gypsum on Mars. *Earth Planet. Sci. Lett.* 317-  
1073 318, 44-55.
- 1074 Mellon, M. T., Arvidson, R. E., Malin, M. C., Lemmon, M. T., Heet, T., Marshall, J., Sizemore,  
1075 H. G., Searls, M. L., Phoenix Science Team, 2008. The Periglacial Landscape and  
1076 Ground Ice at the Mars Phoenix Landing Site. *AGU Fall Meeting Abstracts* 14, 08.

1077 Milkovich, S. M., Head, J. W., 2005. North polar cap of Mars: Polar layered deposit  
1078 characterization and identification of a fundamental climate signal. *J. Geophys. Res.*  
1079 110 (E1), doi:10.1029/2004JE002349.

1080 Milkovich, S. M., Head, J. W., Gerhard, N., 2008. Stratigraphic analysis of the northern polar  
1081 layered deposits of Mars: Implications for recent climate history. *Planet. Space Sci.*  
1082 56 (2), 266-288.

1083 Montmessin, F., Harberle, R. M., Forget, F., Langevin, Y., Clancy R. T., Bibring, J.-P. On the  
1084 origin of perennial water ice at the south pole of Mars: A precession-controlled  
1085 mechanism? *J. Geophys. Res. Planets.* 112 (E8), doi:10.1029/2007JE002902.

1086 Moore, J.M., Mellon, M.T., Zent, A.P., 1996. Mass Wasting and Ground Collapse in Terrains  
1087 of Volatile-Rich Deposits as a Solar System-Wide Geological Process: The Pre-  
1088 Galileo View. *Icarus* 122, 63-78.

1089 Morgan, F., Seelos, F., Murchie, S., CRISM Team, 2009. 'CAT Tutorial', CRISM Data Users'  
1090 Workshop at Lunar Planet. Sci. 40.

1091 Mouginit, J., Pommerol, A., Kofman, W., Beck, P., Schmitt, B., Herique, A., Grima, C.,  
1092 Safaeinili, A., Plaut, J. J., 2010. The 3-5 MHz global reflectivity map of Mars by  
1093 MARSIS/Mars Express: Implications for the current inventory of subsurface H<sub>2</sub>O.  
1094 *Icarus* 210 (2), 612-625.

1095 Newsom, H. E., Brittelle, G. E., Hibbitts, C. A., Crossey, L. J., Kudo, A. M., 1996. Impact  
1096 crater lakes on Mars. *J. Geophys. Res.* 101 (E6), 14951-14955.

1097 Osinski, G. R., Lee, P., Parnell, J., Spray, J. G., Baron, M. T., 2005. A case study of impact-  
1098 induced hydrothermal activity: The Haughton impact structure, Devon Island,  
1099 Canadian high arctic. *Meteorit. Planet. Sci.* 40 (12), 1859-1877.

- 1100 Pankine, A. A., Tamppari, L. K., Smith, M. D., 2009. Water vapor variability in the north polar  
1101 region of Mars from Viking MAWD and MGS TES datasets. *Icarus* 204 (1), 87-102.
- 1102 Perron, J. T., Mitrovica, J. X., Manga, M., Matsuyama, I., Richards, M. A., 2007. Evidence of  
1103 an ancient martian ocean in the topography of deformed shorelines. *Nature* 447, 840-  
1104 843.
- 1105 Perron, J. T., Huybers, P., 2009. Is there an orbital signal in the polar layered deposits on  
1106 Mars? *Geology* 37 (2), 155-158.
- 1107 Phillips, R. J., Zuber, M. T., Smrekar, S. E., Mellon, M. T., Head, J. W., Tanaka, K. L.,  
1108 Putzig, N. E., Milkovich, S. M., Campbell, B. A., Plaut, J. J., Safaeinili, A., Seu, R.,  
1109 Biccari, D., Carter, L. M., Picardi, G., Orosei, R., Surdas Mohit, P., Heggy, E., Zurek,  
1110 R. W., Egan, A. F., Giacomoni, E., Russo, F., Cutigni, M., Pettinelli, E., Holt, J. W.,  
1111 Leuschen, C. J., Marinangeli, L., 2008. Mars north polar deposits: stratigraphy, age,  
1112 and geodynamical response. *Science* 320 (5880), 1182-1185.
- 1113 Plaut, J. J., Safaeinili, A., Holt, J. W., Phillips, R. J., Head, J. W., Seu, R., Putzig, N. E.,  
1114 Frigeri, A., 2009. Radar evidence for ice in lobate debris aprons in the mid-northern  
1115 latitudes of Mars. *Geophys. Res. Lett.* 36, 02203.
- 1116 Putzig, N. E., Phillips, R. J., Campbell, B. A., Holt, J. W., Plaut, J. J., Carter, L. M., Egan, A.  
1117 F., Bernardini, F., Safaeinili, A., Seu, R., 2009. Subsurface structure of Planum  
1118 Boreum from Mars Reconnaissance Orbiter Shallow Radar soundings. *Icarus* 204  
1119 (2), 443-457.
- 1120 Rathbun, J. A., Squyres, S. W., 2002. Hydrothermal Systems Associated with Martian  
1121 Impact Craters. *Icarus* 157, 362-372.

- 1122 Rodríguez, J. A. P., Tanaka, K. L., Berman, D. C., Kargel, J. S., 2010. Late Hesperian plains  
1123 formation and degradation in a low sedimentation zone of the northern lowlands of  
1124 Mars. *Icarus* 210 (1), 116-134.
- 1125 Russell, P. S., Head, J. W., 2002. The martian hydrosphere/cryosphere system: Implications  
1126 of the absence of hydrologic activity at Lyot crater. *Geophys. Res. Lett.* 29 (17),  
1127 doi:10.1029/2002GL015178.
- 1128 Russell, P. S., Head, J. W., Hecht, M. H., 2003. Evolution of Volatile-rich Crater Interior  
1129 Deposits on Mars. Sixth International Conference on Mars. Abstract 3256.
- 1130 Russell, P. S., J. W. Head, I., Hecht, M. H., 2004. Evolution of Ice Deposits in the Local  
1131 Environment of Martian Circum-Polar Craters and Implications for Polar Cap History.  
1132 *Lunar Planet. Sci.* 35. Abstract 2007.
- 1133 Russo, F., Cutigni, M., Orosei, R., Taddei, C., Seu, R., Biccari, D., Giacomoni, E., Fuga, O.,  
1134 Flamini, E., 2008. An incoherent simulator for the SHARAD experiment. Radar  
1135 Conference, RADAR '08. IEEE, Rome, Italy, doi:10.1109/RADAR.2008.4720761
- 1136 Sakimoto, S. E. H., 2005. Central Mounds in Martian Impact Craters: Assessment as  
1137 Possible Perennial Permafrost Mounds (Pingos). *Lunar Planet. Sci.* 36. Abstract  
1138 2099.
- 1139 Seelos, K. D., Seelos, F. P., Titus, T. N., Murchie, S. L., Crism, T., 2008. CRISM  
1140 Observations of Persistent Water Ice Deposits in the Northern Plains of Mars. *Lunar*  
1141 *Planet. Sci.* 39. Abstract1885.
- 1142 Selvans, M. M., Plaut, J. J., Aharonson, O., Safaeinili, A., 2010. Internal structure of Planum  
1143 Boreum, from Mars advanced radar for subsurface and ionospheric sounding data. *J.*  
1144 *Geophys. Res.* 115 (E9), doi:10.1029/2009JE003537.



- 1145 Smith, D. E., Zuber, M. T., Neumann, G. A., 2001. Seasonal Variations of Snow Depth on  
1146 Mars. *Science* 294 (5549), 2141-2146.
- 1147 Smith, I. B., Holt, J. W., 2010. Onset and migration of spiral troughs on Mars revealed by  
1148 orbital radar. *Nature* 465 (7297), 450-453.
- 1149 Spiga, A., Forget, F., Madeleine, J.-B., Montabone, L., Lewis, S.R., Millour, E., 2011. The  
1150 impact of martian mesoscale winds on surface temperature and on the determination  
1151 of thermal inertia. *Icarus* 212, 504–519.
- 1152 Stepinski, T. F., Mendenhall, M. P., Bue, B. D., 2009. Machine cataloging of impact craters  
1153 on Mars. *Icarus* 203 (1), 77-87.
- 1154 Tanaka, K. L., Skinner Jr, J. A., Hare, T. M., 2005. Geologic map of the northern plains of  
1155 Mars. Scientific Investigation Map 2888. USGS/NASA.
- 1156 Tanaka, K. L., Hayward, R. K., 2008. Mars' North Circum-Polar Dunes: Distribution,  
1157 Sources, and Migration History. Planetary Dunes Workshop: A Record of Climate  
1158 Change, held April 29-May 2, 2008 in Alamogordo, New Mexico. Abstract1403, p.69-  
1159 70.
- 1160 Tanaka, K. L., Rodriguez, J. A. P., Skinner Jr, J. A., Bourke, M. C., Fortezzo, C. M.,  
1161 Herkenhoff, K. E., Kolb, E. J., Okubo, C. H., 2008. North polar region of Mars:  
1162 Advances in stratigraphy, structure, and erosional modification. *Icarus* 196 (2), 318-  
1163 358.
- 1164 Titus, T.N., Kieffer, H.H., Mullins, K.F., Christensen, P.R., 2001. TES premapping data: Slab  
1165 ice and snow flurries in the Martian north polar night. *J. Geophys. Res.* 106, 23181-  
1166 23196, doi : 10.1029/2000JE001284.
- 1167 Vincendon, M., 2008. Modélisation du transfert radiatif dans l'atmosphère martienne pour la  
1168 détermination des propriétés spectrales de surface et la caractérisation des aérosols

- 1169            martiens à partir des données OMEGA. PhD Thesis, Université de Paris-Sud XI, pp.  
1170            193.
- 1171    Vincendon, M., Langevin, Y., Poulet, F., Bibring, J. P., Gondet, B., Schmitt, B., Douté, S.,  
1172            2006. Surface Water Ice and Aerosols Evolution of 77°N, 90°E Mars Crater During  
1173            Early Summer by OMEGA/MEx. Lunar Planet. Sci. 37. Abstract 1769.
- 1174    Vincendon, M., Forget, F., Mustard, J., 2010. Water ice at low to midlatitudes on Mars. J.  
1175            Geophys. Res. 115, doi:10.1029/2010JE003584.
- 1176    Wagstaff, K. L., Titus, T. N., Ivanov, A. B., Castaño, R., Bandfield, J. L., 2008. Observations  
1177            of the north polar water ice annulus on Mars using THEMIS and TES. Planet. Space  
1178            Sci. 56 (2), 256-265.
- 1179    Westbrook, O.W., 2009. Crater ice deposits near the south pole of Mars. Masters Thesis,  
1180            Massachusetts Institute of Technology, pp. 60.
- 1181

## 1182 **Figure Captions**

1183 Figure 1: Depth-diameter plot of all the craters north of 65°N, with ice-filled craters and dune-  
1184 filled craters highlighted. Lines extending above the mound-points are the predicted depths  
1185 of the craters with the mounds removed. Depth-diameter relationship derived for polar  
1186 craters by Garvin et al. (2000) and the general relationship for Martian craters (Garvin, 2005)  
1187 are marked. An anomalous pixel in the MOLA data has resulted in a ~1.5 km crater with  
1188 >1 km depth, we believe this pixel to be an error in the data; hence this point should be  
1189 ignored.

1190

1191 Figure 2: Map of the north polar region of Mars made from MOLA topography with overlain  
1192 hillshade. It includes the locations of the mounds studied and locations of the swaths used to  
1193 produce Fig. 4. Outlined in grey are all the craters included in the survey. The “+” indicates  
1194 the position of crater 332, which is mentioned in the text, but does not have a significant  
1195 mound. “OM” indicates the position of Fig. 17, with the arrow showing the viewing direction.  
1196 “Complete dune cover” means that the mound spans the whole crater floor and is covered in  
1197 dunes and “dune-covered mounds” are those which are covered in dunes, but only occupy  
1198 part of the crater floor (the rest of the crater floor is dune-free.)

1199

1200 Figure 3: Left, Crater 388 Dokka. Perspective view (with 3x vertical exaggeration) of a  
1201 subset of HRSC nadir (RGB-color online) image H1177\_0000 draped over MOLA  
1202 topography with profiles A-A’ and B-B’ marked and shown beneath. Right: Crater 811.  
1203 Perspective view (with 3x vertical exaggeration) of a subset of HRSC nadir (RGB-color  
1204 online) image H3711\_0000 draped over MOLA topography with profiles C-C’ and D-D’  
1205 marked. The 20 m scale vertical roughness on profiles C and D is a result of the overlying  
1206 dunes. Arrow points to North in both figures. Profiles A, B, C and D were generated from

1207 MOLA topography – note the exaggeration of the vertical scale. Credit for HRSC images  
1208 ESA/DLR/FU Berlin (G. Neukum).

1209

1210 Figure 4: Histogram plots of the elevation variation with latitude within the swaths outlined in  
1211 Fig. 2. Black (blue online) indicates craters with ice-mounds and the height to which those  
1212 mounds reach, labels correspond to those in Fig. 2 and Table 1. Note that the vertical scale  
1213 is exaggerated.

1214

1215 Figure 5: Bar chart of calculated mound volume for each crater in descending order. Note  
1216 the logarithmic scale on the y-axis. The mean value ( $314.7 \text{ km}^3$ ) is indicated by the upper  
1217 dashed line and the median value ( $17.01 \text{ km}^3$ ) by the lower dotted line.

1218

1219 Figure 6: Right optical image with scale and north arrow, and left optical image overlain by  
1220 proportion of water ice detected (band depth at  $1.5 \mu\text{m}$ ).

1221 (A) Korolev crater (206), optical images from MRO CTX P20\_008831\_2529\_XN\_72N195W  
1222 ( $L_s 85.33^\circ$ ), P21\_009042\_2528\_XI\_72N197W ( $L_s 92.58^\circ$ ),  
1223 P21\_009332\_2529\_XN\_72N194W ( $L_s 102.66^\circ$ ), P22\_009477\_2530\_XN\_73N193W ( $L_s$   
1224  $107.77^\circ$ ), P22\_009754\_2529\_XN\_72N195W ( $L_s 117.69^\circ$ ), and OMEGA track 0987\_2 ( $L_s$   
1225  $105.9^\circ$ ).

1226 (B) Dokka crater (388), optical images MRO CTX B01\_010108\_2573\_XN\_77N144W ( $L_s$   
1227  $130.74^\circ$ ) and B02\_010385\_2572\_XN\_77N146W ( $L_s 141.32^\circ$ ), OMEGA track 1221\_1 ( $L_s$   
1228  $136.4^\circ$ ).

1229 (C) Crater 544, optical images THEMIS V13697003 ( $L_s 144.508$ ) and V12474005 ( $L_s$   
1230  $97.106^\circ$ ), OMEGA track 1257\_0 ( $L_s 141.3^\circ$ ).

1231 (D) Crater 579, optical image MRO CTX P02\_001819\_2570\_XN\_77N270W ( $L_s 151.16^\circ$ ),  
1232 OMEGA track 1017\_1 ( $L_s 109.5^\circ$ ).

1233 (E) Louth crater (503), optical image HRSC h1343\_0001 ( $L_s$  153.5°), OMEGA track 1017\_1  
1234 ( $L_s$  109.5°). Credit for CTX images NASA/JPL/MSSS, for HiRISE images  
1235 NASA/JPL/University of Arizona, for THEMIS images NASA/JPL/ASU, for HRSC images  
1236 ESA/DLR/FU Berlin (G. Neukum), for OMEGA data ESA/OMEGA.

1237

1238 Figure 7: Maps of layer exposures and measured layer dips in Korolev (206), Dokka (338),  
1239 crater 579, Louth (503), crater 769 and crater 663. Shaded areas represent areas where  
1240 layers were observed to be cropping out, dotted lines are selected layers to illustrate the  
1241 nature of the layering and the dip and strike labels are in units of degrees. Dotted box in  
1242 panel 579 indicates the approximate location of Fig. 10. Images all MRO CTX: **206 Korolev:**  
1243 P20\_008831\_2529\_XN\_72N195W, P21\_009042\_2528\_XI\_72N197W,  
1244 P21\_009332\_2529\_XN\_72N194W, P22\_009477\_2530\_XN\_73N193W,  
1245 P22\_009754\_2529\_XN\_72N195W, **388 Dokka:** B01\_010108\_2573\_XN\_77N144W and  
1246 B01\_010108\_2573\_XN\_77N144W, **579:** P02\_001819\_2570\_XN\_77N270W, **503 Louth:**  
1247 P01\_001370\_2503\_XI\_70N257W, **769:** B02\_010407\_2587\_XN\_78N028W, **663:**  
1248 P20\_008795\_2592\_XN\_79N299W. Image credit NASA/JPL/MSSS.

1249

1250 Figure 8: Boxplots of the estimated layer spacing in mounds and polar deposits. The vertical  
1251 bars are the median values, the boxes delimit the interquartile range, the whiskers the range  
1252 and the dots are the outliers (data points outside 1.5 interquartile ranges from the box). In  
1253 grey are measurements made outside craters. Shorthand labels are as follows: **206 Korolev**  
1254 – layers measured in Korolev crater in CTX images P20\_008831\_2529\_XN\_72N195W and  
1255 P21\_009042\_2528\_XI\_72N197W, **388 Dokka** – layers measured in Dokka crater in CTX  
1256 images B01\_010108\_2573\_XN\_77N144W and B02\_010385\_2572\_XN\_77N146W, **503**  
1257 **Louth HR** - layers proximal to dunes in Louth crater measured in HiRISE  
1258 PSP\_001700\_2505, **503 Louth CTX** – layers measured in CTX image  
1259 P01\_001370\_2503\_XI\_70N257W at the edge of the mound in Louth, **579:** layers identified in

1260 crater 579 in HiRISE image PSP\_008926\_2575, **663** - layers measured in crater 663  
1261 corrected for layer dip as well as exposure slope, in HiRISE image ESP\_016087\_2595, **769**  
1262 – layers measured in crater 769 in HiRISE image PSP\_008416\_2585, **PLD1** – layers  
1263 measured in the PLD in HiRISE image PSP\_010366\_2590, **PLD2** - layers measured in the  
1264 polar layer deposits in HiRISE image TRA\_000825\_2665 and **PLD3** - layers measured in the  
1265 polar layer deposits in HiRISE image TRA\_000863\_2640, upper quartile is at 15.0 m and the  
1266 upper whisker at 29.3 m, with one outlier at 39.8 m. **BU** – layers measured in the polar basal  
1267 deposits in HiRISE image TRA\_000863\_2640.

1268

1269 Figure 9: Histogram of mound slopes on layer exposure sites (as shown in Fig.7) as derived  
1270 from 128 pixel/degree MOLA data. The mean of the distribution is  $4.4^\circ$  with a standard  
1271 deviation of  $3.6^\circ$  and skew of 1.29.

1272

1273 Figure 10: Detailed sketch (left) cross section (top right) and detail-inset (bottom-right) of the  
1274 layer stratigraphy in crater 579. On the sketch dotted lines are selected layers to illustrate  
1275 the nature of the layering, bold lines are the locations of unconformities and dip and strike  
1276 symbol labels are in units of degrees. The line labeled I-II indicates the position of the cross  
1277 section adjacent to the image. Colored lines are contours in 25 m intervals derived from  
1278 gridded MOLA 128 pixel/degree data (see online for color version). The crater wall is located  
1279 to the right in both the sketch and the cross-section. Overlain on the sketch is the CTX  
1280 image P02\_001819\_2570\_XN\_77N270W, credit NASA/JPL/MSSS. Labels A, B and C are  
1281 packets of layers separated by unconformities. On the cross-section dotted lines show the  
1282 estimated position of the unconformities and the relative vertical positions of the three layer  
1283 packets A, B and C. From layer cross-cutting relationships we know that A is older than B,  
1284 which is older than C; hence the packets were laid down in an upwards younging sequence.  
1285 The location of the inset is indicated by the grey box. The image in the inset is HiRISE image  
1286 PSP\_008926\_2575; credit NASA/JPL/University of Arizona.

1287

1288 Figure 11: Depth-corrected SHARAD radargram r\_0554201\_001 and clutter simulation for  
1289 Korolev (206) crater. South is to the right.

1290

1291 Figure 12: Map of the mound center-of-mass offsets with respect to the crater center  
1292 (normalized by crater diameter) with the mapped location of north pole dunefields and wind  
1293 vectors from dune slipface measurements taken from Tanaka and Hayward (2008). The  
1294 vector linking the center of mass of the ice mound to the centroid of the crater rim polygon  
1295 we use as a representation of the asymmetry of the mounds. Dune density is given as the  
1296 relative density parameter calculated by Tanaka and Hayward (2008) as the ratio of mean  
1297 dune length vs. dune crest separation.

1298

1299 Figure 13: The variation of bolometric brightness temperature with season ( $L_s$ ), inside and on  
1300 the ice-free plains outside two example craters as derived from TES data downloaded using  
1301 the TES Data Tool – [http://tes.asu.edu/data\\_tool/](http://tes.asu.edu/data_tool/) for Mars years 24 to 28. The dataset  
1302 contains both data collected at 2pm and 2am local solar time; hence there are two distinct  
1303 temperatures between  $90$ - $180^\circ L_s$  when the sun is above the horizon at 2pm. Dokka Crater  
1304 (388), a 51 km diameter crater which contains a dome of water ice, which suppresses the  
1305 temperature almost all year round relative to that outside the crater. Crater 1065, at  $70^\circ N$ ,  
1306  $352^\circ E$  diameter  $\sim 40$  km, which has lower temperatures than the exterior only between  $L_s$   
1307  $250^\circ$  and  $L_s 320^\circ$ . The grey band indicates the water frost point temperatures corresponding  
1308 to an atmospheric water content of between 10 and 60  $\text{pr}\mu\text{m}$  (Pankine et al., 2009).

1309

1310 Figure 14: Location of temporary ice deposits which remain after the seasonal cap has  
1311 retreated, as indicated by arrows. The background is a MOLA hillshade image. A: Deposits  
1312 around crater 561 at  $267^\circ E$ ,  $70^\circ N$  form a plume extending to the east, matching dominant  
1313 wind directions in this area (Fig. 12). CTX images P17\_007799\_2513\_XN\_71N093W and

1314 P18\_007944\_2506\_XN\_70N092W. B: Deposits around crater 263 at 146°E, 72°N are  
1315 located mainly on north-facing slopes, CTX image B01\_009847\_2522\_XN\_72N214W.  
1316 Image credit MSSS/NASA/JPL.

1317

1318 Figure 15: Schematic diagram of the initiation and growth of ice domes, with the ices  
1319 throughout as labeled in the first panel. North is to the right in all diagrams. The thickness of  
1320 the frost and ice deposits are greatly exaggerated for illustration purposes. 1. In winter the  
1321 microclimate in the crater provokes additional deposition of CO<sub>2</sub> and water ice inside the  
1322 crater. 2. During the springtime sublimation, the CO<sub>2</sub> layer inside the crater remains  
1323 (because a thicker layer takes longer to sublime), while the crater exterior is denuded of CO<sub>2</sub>  
1324 and the H<sub>2</sub>O starts to sublime. The H<sub>2</sub>O released from the plains around the crater can be  
1325 re-deposited in the crater interior, because of its lower temperature (as the CO<sub>2</sub> remains).3.  
1326 Once the CO<sub>2</sub> has completely sublimed, relatively thick deposits of H<sub>2</sub>O remain in the crater  
1327 (H<sub>2</sub>O from winter plus the H<sub>2</sub>O re-condensed onto the CO<sub>2</sub>), which act as a cold trap for H<sub>2</sub>O  
1328 subliming outside the crater. In addition the higher atmospheric pressure inside the crater  
1329 reduces the rate of sublimation of this water ice. 4. The additional thickness and the reduced  
1330 sublimation enable the survival of at least several meters thick deposit of water ice through  
1331 the summer, which then builds up each year. A perennial deposit creates a positive  
1332 feedback whereby higher thermal inertia and higher albedo than the surrounding landscape  
1333 promotes continued deposition of water ice.

1334

1335 Figure 16: Perspective view of polar outliers near Olympia Mensae at 96.5°E, 74°N. Vertical  
1336 exaggeration is five times. Outcrop in foreground is ~350 m tall and 10 km wide at the base.  
1337 CTX images P21\_009295\_2550\_XN\_75N263W and P20\_009018\_2543\_XI\_74N262W used  
1338 for topographic drape. Background hillshade and topography from the MOLA gridded 256  
1339 tile. CTX image credit MSSS/NASA/JPL.

1340



1341 **Supp. Mat. Figure Captions**

1342 Figure S1: MOLA hillshade image and cross sections for all 18 craters with mounds. The  
1343 black line on the image corresponds to the black north-south cross section on the plot,  
1344 where “N” on the image indicates the northern end. The red line indicates the position of red  
1345 east-west cross section on the plot (always oriented E-W apart from for crater 503, Louth).  
1346 Data from the 256 pix/deg MOLA gridded data were used to produce the hillshade and cross  
1347 sections for craters 206, 503, 579, 811, 814, 882, 904 and 934; for the others the data are  
1348 derived from the 512 pix/deg gridded data.

1349 Table 1: Summary of the characteristics of the mounds and their host craters.<sup>a</sup>

Crater ID	Depth (m)	Diameter (km)	Longitude (°E)	Latitude (°N)	Distance to cap (km)	SwathID	Predicted depth (m)	Max. mound thickness (m)	Mound volume (km <sup>3</sup> )	Garvina ID	Garvina mound volume (km <sup>3</sup> )	Garvina predicted initial depth (m)	Presence of Dunes	Mound planimetric area		Mound relief		Max. slope (°)	Mean slope (°)	Mound summit to rim distance (m)	
														absolute (km <sup>2</sup> )	as % of crater area	absolute (m)	as % of depth			absolute	as % of depth
206 Korolev	3102	82.83	164.49	72.75	624	5	3133	1845	3848.5	E	1356	2860	none	3134	56	1818	59	33.5	3.5	1284	41
332 <sup>#</sup>	1364	21.35	195.59	76.97	330	5	n/c	n/c	n/c	G	2.5	660	partial	n/c	n/c	117*	9*	n/c	n/c	1039*	76*
388 Dokka	2508	51.26	214.29	77.17	301	6	3053	1890	1318.9	D	463	1540	none	1115	53	1443	58	28.7	4.0	1065	42
436	1248	19.66	190.08	81.59	60	5	2069	1640	95.9	A	59	640	partial	129	43	909	73	23.1	6.2	339	27
480	936	16.13	240.14	78.11	119	6	930	383	4.4				100%	30	14	407	44	22.7	5.7	529	56
503 Louth	1788	36.15	103.24	70.17	568	4	1766	267	13.3				partial	136	12	400	22	14.5	3.2	1388	78
515	250	11.21	117.25	81.36	0	4	305	139	2.4				none	37	37	118	47	3.8	1.1	133	53
544	773	20.96	255.07	81.27	0	6	788	378	21.0	F	35	610	none	107	42	686	89	10.4	3.7	87	11
577	248	11.73	88.93	81.16	0	4	284	133	2.4				none	32	52	157	63	4.5	1.4	72	31
579	1173	30.53	89.13	77.11	130	4	1517	932	201.6	B	248	1170	none	485	65	736	63	19.4	2.5	437	37
663	1451	24.60	60.92	79.13	0	3	1836	1017	59.1	H	3.4	600	partial	126	28	822	57	23.7	4.3	629	43
697	151	9.52	47.62	79.76	0	3	161	94	1.0				none	21	46	103	68	3.8	1.6	13	11
769	1058	20.19	331.72	78.59	8	1	1103	512	21.1	C	34	680	partial	96	29	685	65	15.1	4.9	374	35
795	371	12.55	347.00	78.61	0	1	371	178	3.1				none	41	32	274	74	6.8	2.5	98	26
811	571	18.82	309.02	71.20	452	2	773	565	40.4				100%	138	49	380	67	17.2	3.3	191	33
814	694	16.95	319.18	74.25	257	2	666	408	20.7				100%	97	41	457	66	19.8	4.1	237	34
882	572	16.32	340.23	75.05	190	1	543	150	1.8				100%	29	13	192	33	9.2	2.5	381	67
904	993	22.59	346.90	74.63	186	1	942	121	0.8				100%	84	20	178	18	20.1	2.9	488	73
934	666	15.86	348.27	73.54	249	1	653	240	7.2				100%	28	14	368	55	9.8	2.2	626	63

<b>Min.</b>	151	9.52	70.17	0	161	94	0.8		21	12	103	9	3.8	1.1	13	11
<b>Mean</b>	1048	24.33	76.97	183	1161	605	314.7		326	36	563	54	15.9	3.3	495	44
<b>Median</b>	936	19.24	77.17	130	859	381	17.0		96	39	403	59	16.2	3.2	381	41
<b>Max.</b>	3102	82.83	81.59	624	3133	1890	3848.5		3134	65	1818	89	33.5	6.2	1388	78

1350 <sup>a</sup> Abbreviations and symbols used: Max. = maximum, Min. = minimum, Garvin# refers to results in Garvin et al. (2000), # refers to the crater

1351 that has layered deposits, but no significant mound, n/c = not calculated, and \* indicates that the relief was estimated from a MOLA cross

1352 profile, rather than taking the difference between the max. and min. MOLA elevations found within the mound polygon.

### Highlights:

- 18 potentially ice-cored mounds were found in craters in Mars' north polar region.
- The stratigraphy of the mounds argues for deposition from the atmosphere.
- We argue many of them were deposited separately from the polar cap.
- The crater micro-environment is a potential explanation for mound initiation.
- These mounds are sensitive and important records of Amazonian climate on Mars.

Figure1 (black and white)

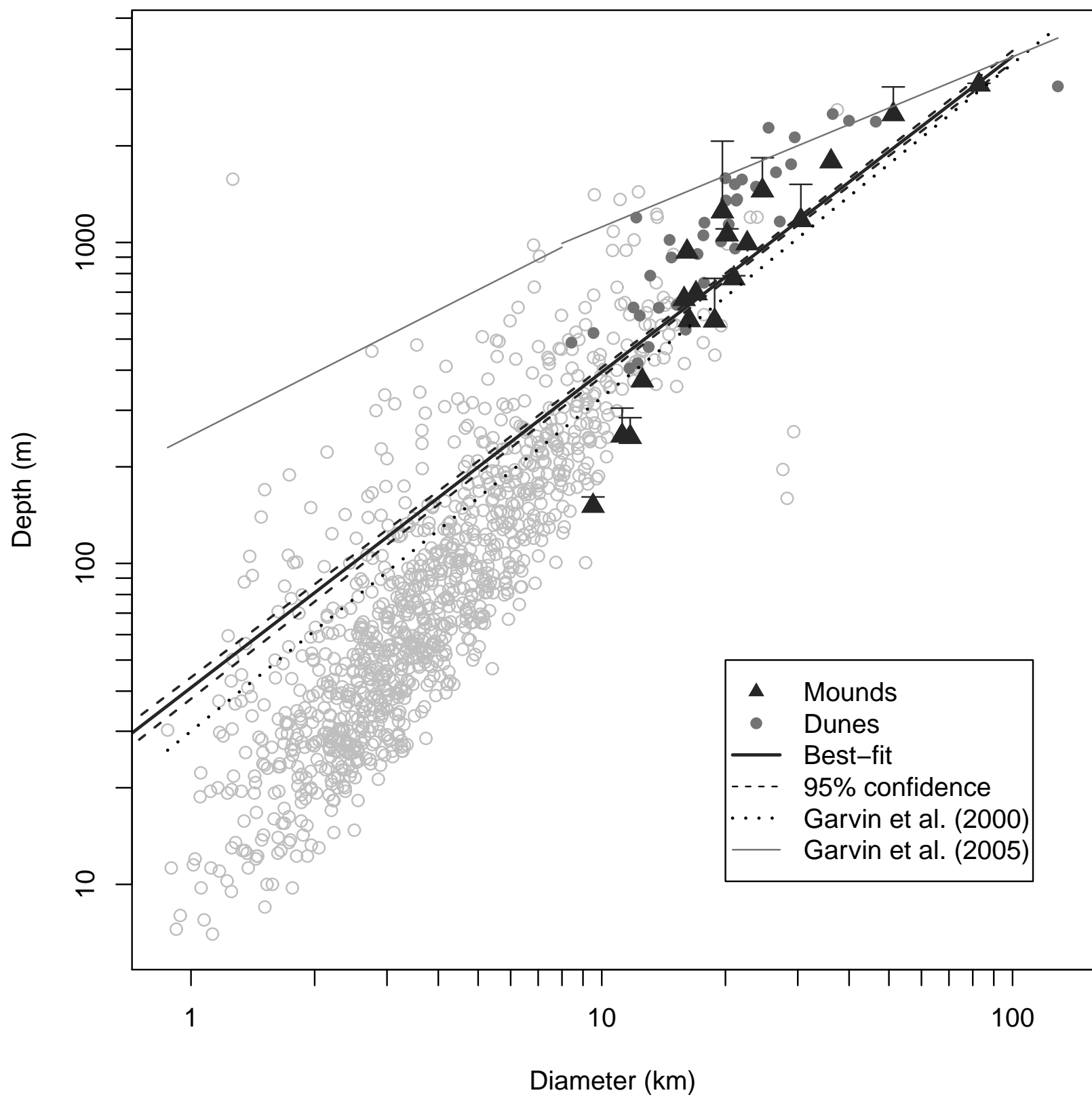


Figure1

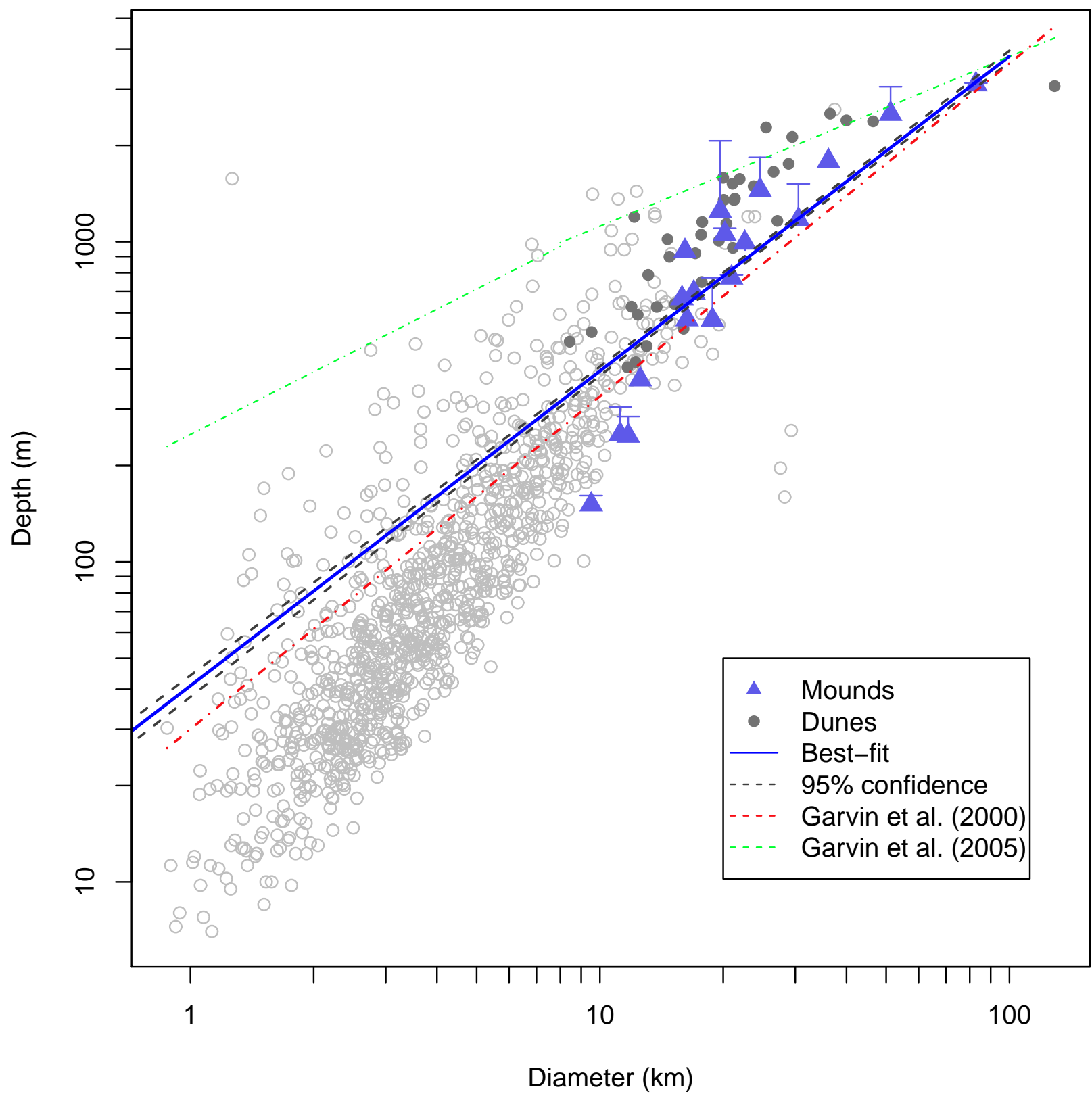


Figure 2 (black and white)  
[Click here to download high resolution image](#)

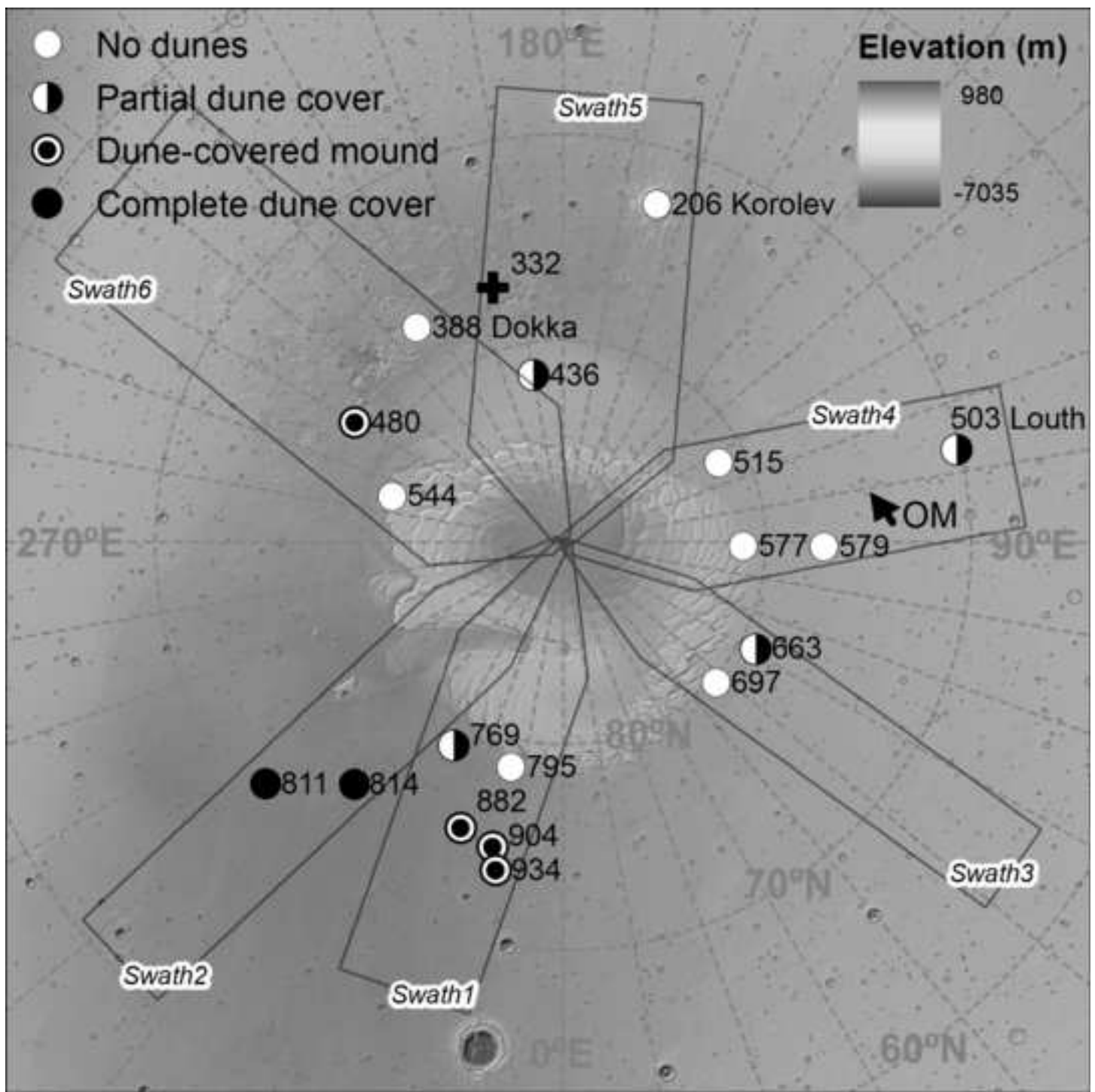


Figure 2  
[Click here to download high resolution image](#)

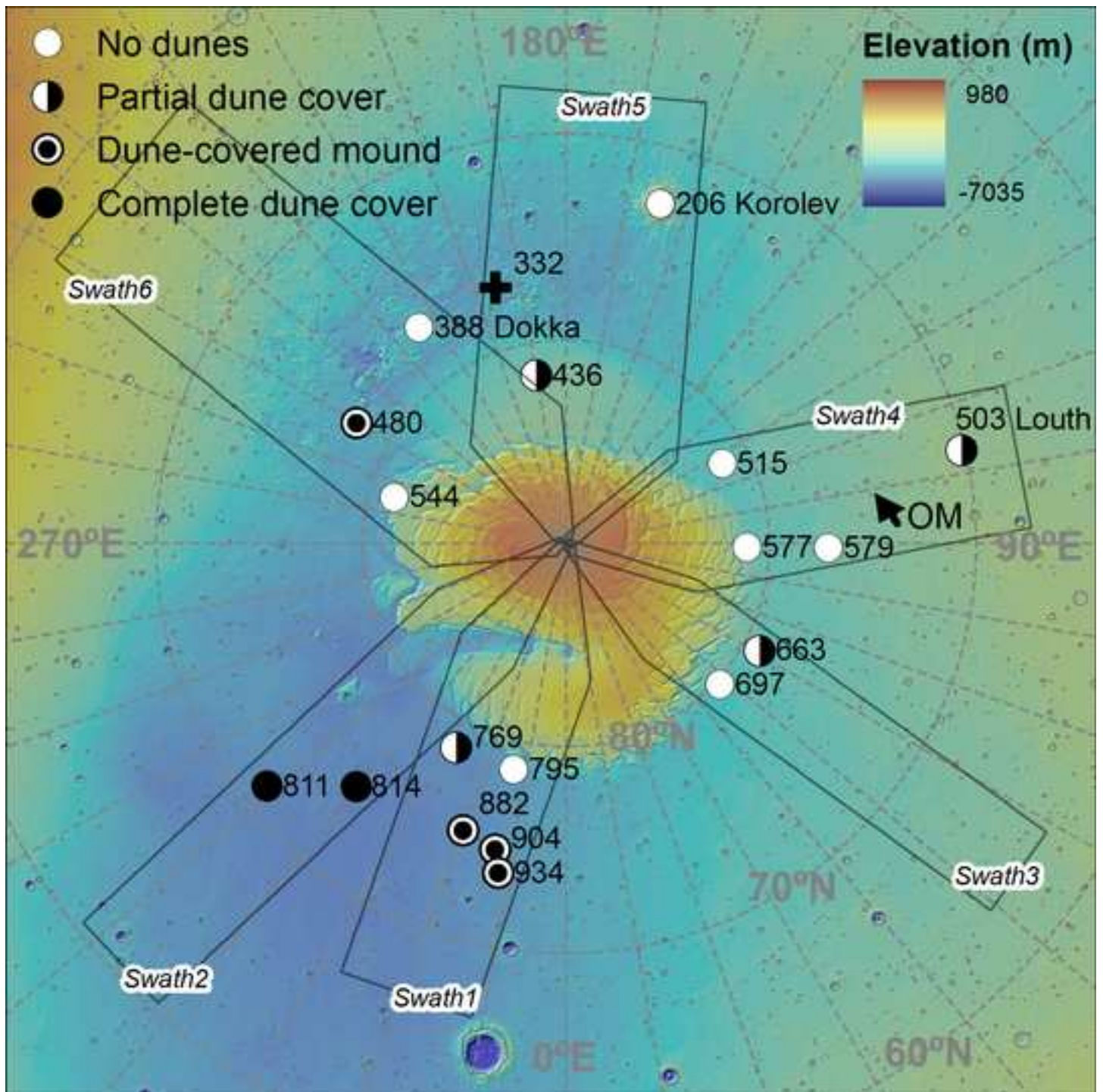




Figure 3 (black and white)  
[Click here to download high resolution image](#)

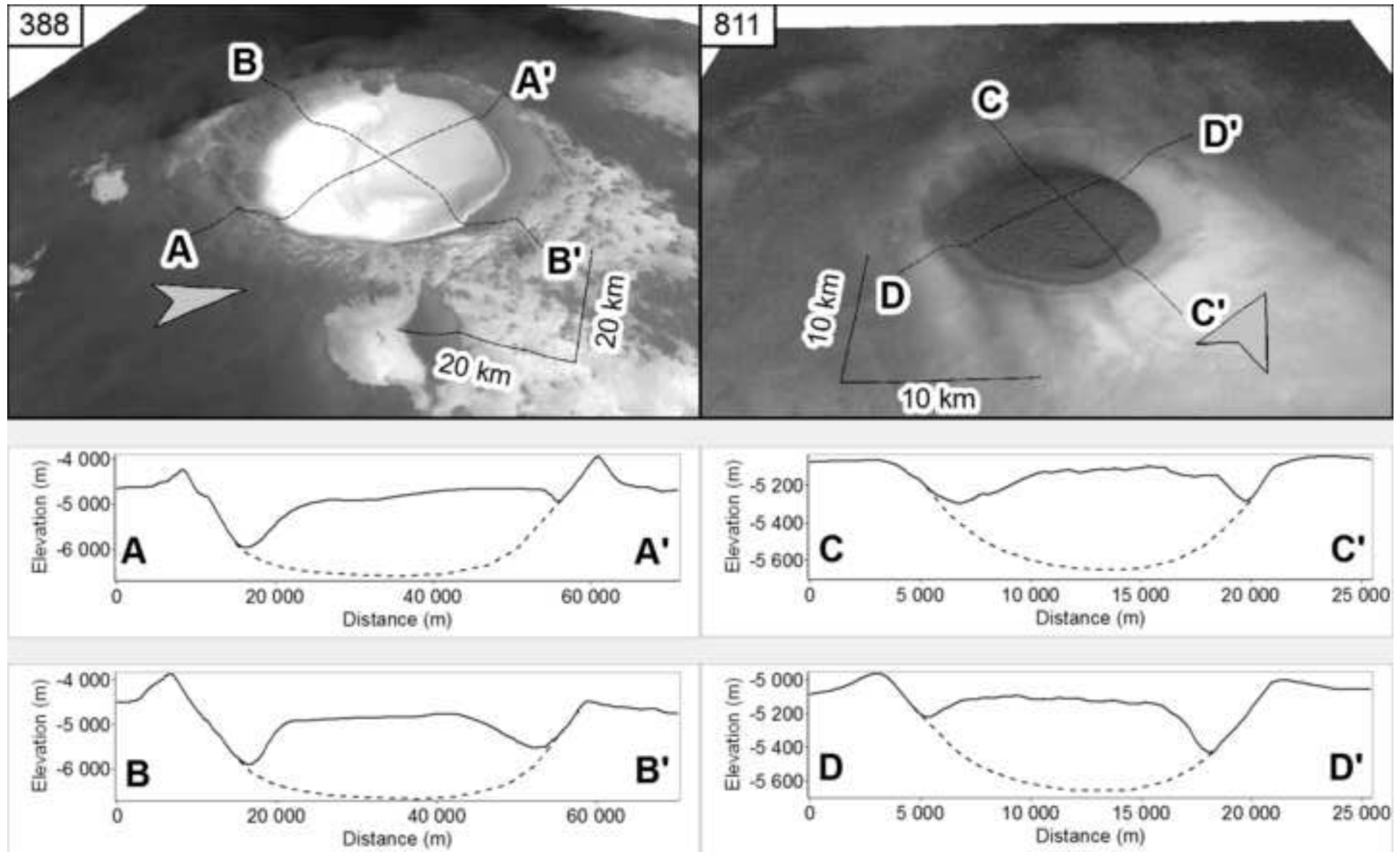


Figure 3  
[Click here to download high resolution image](#)

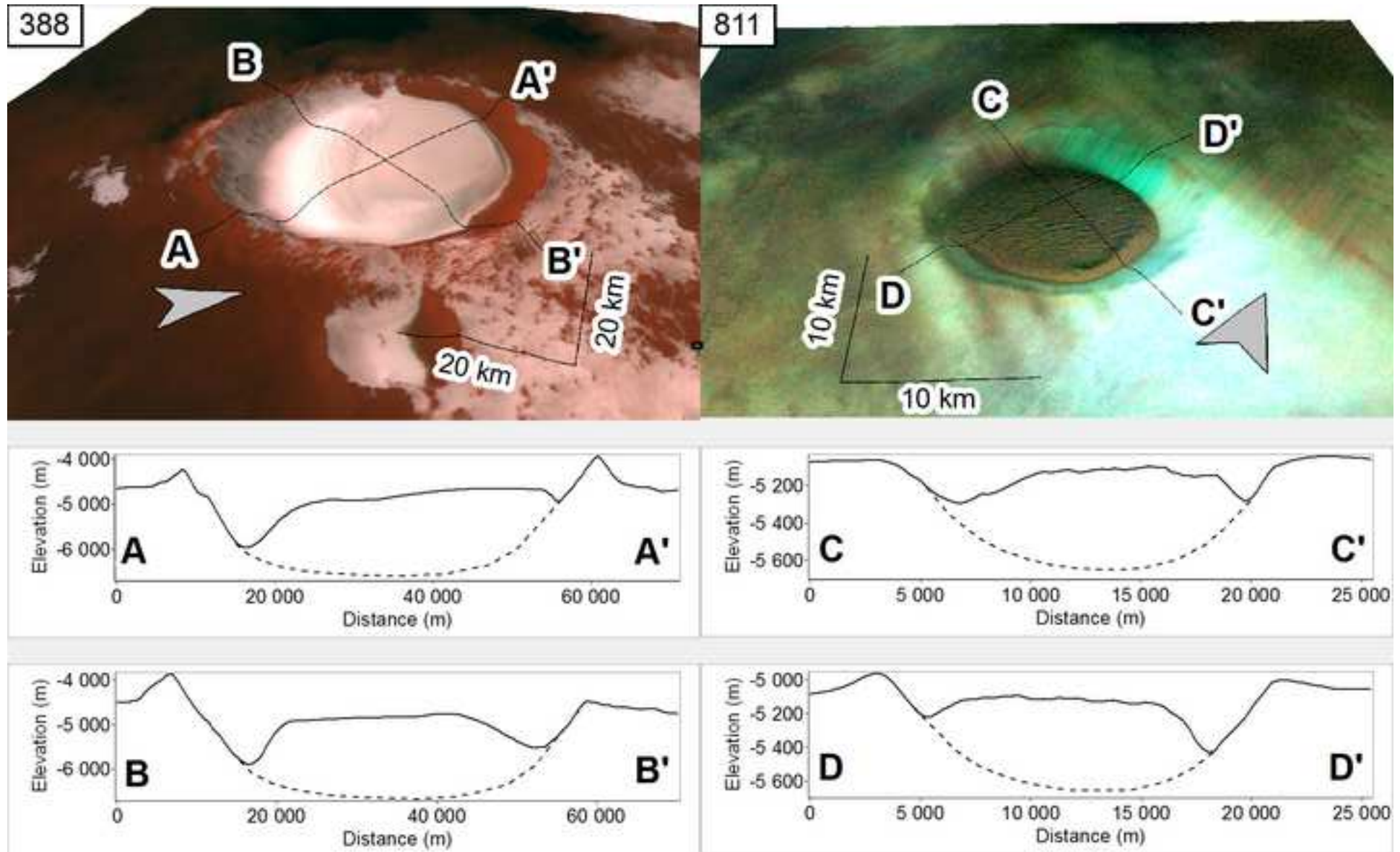


Figure 4 (black and white)

[Click here to download high resolution image](#)

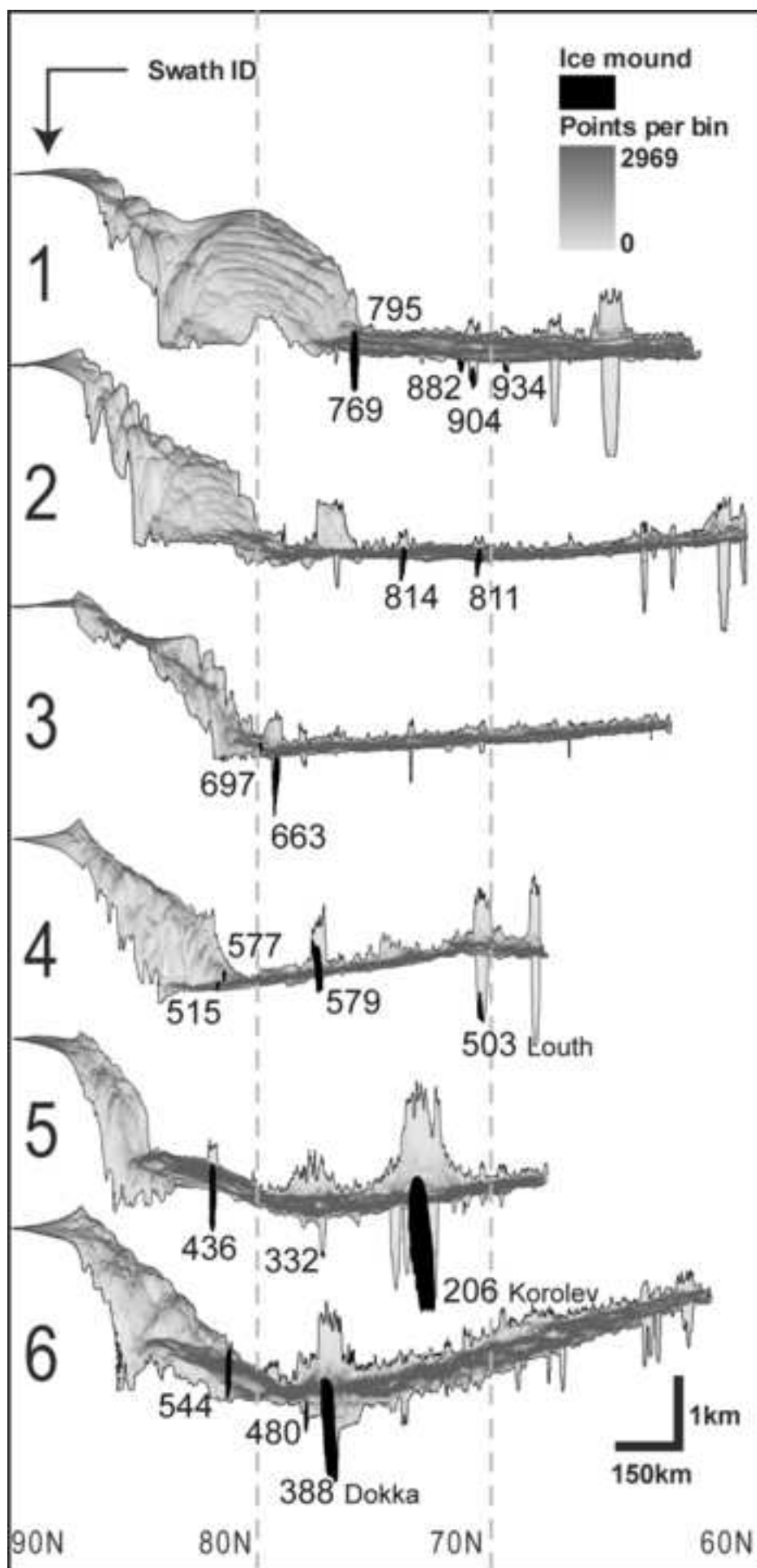


Figure 4

[Click here to download high resolution image](#)

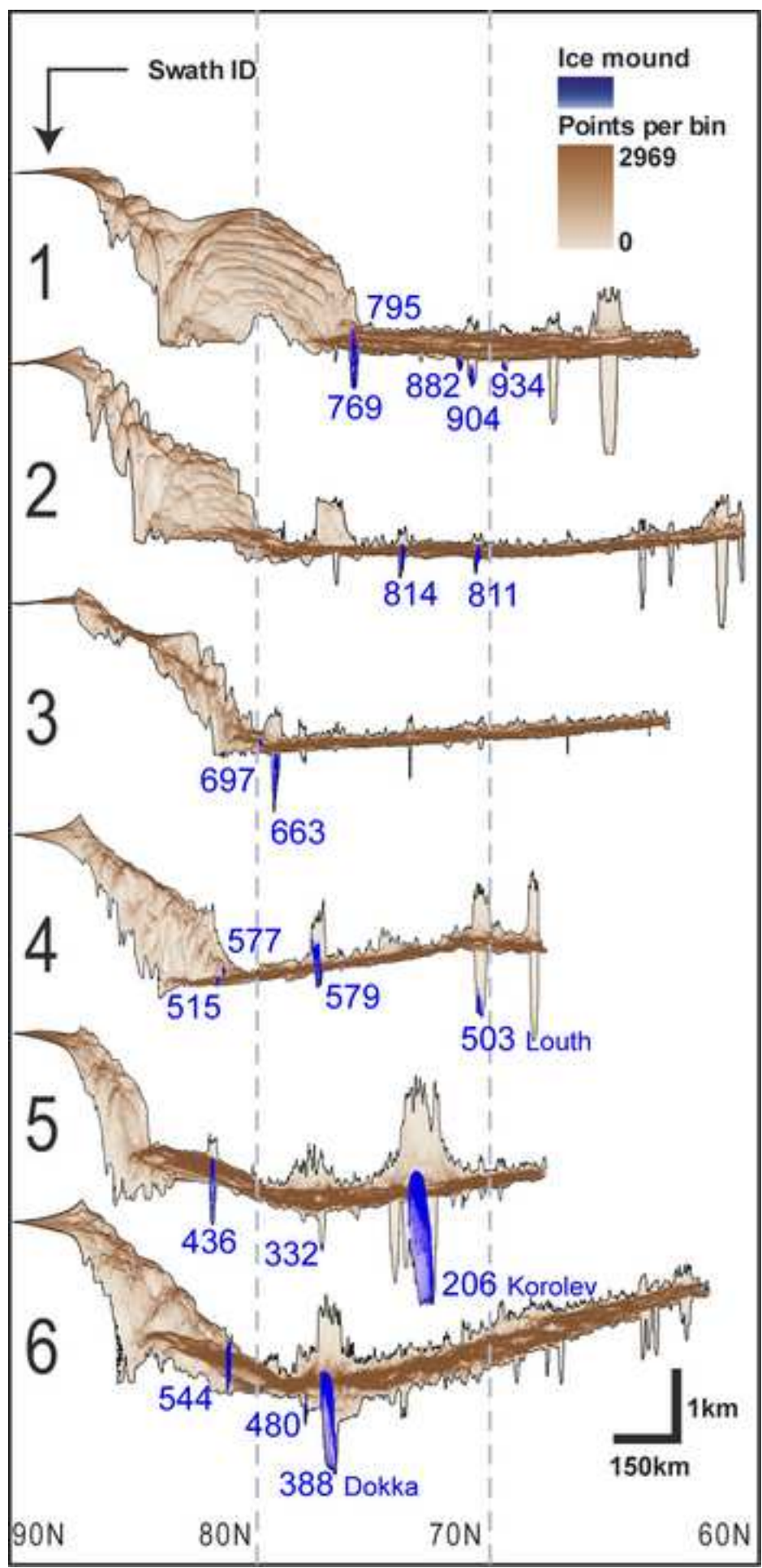


Figure 5 (black and white)

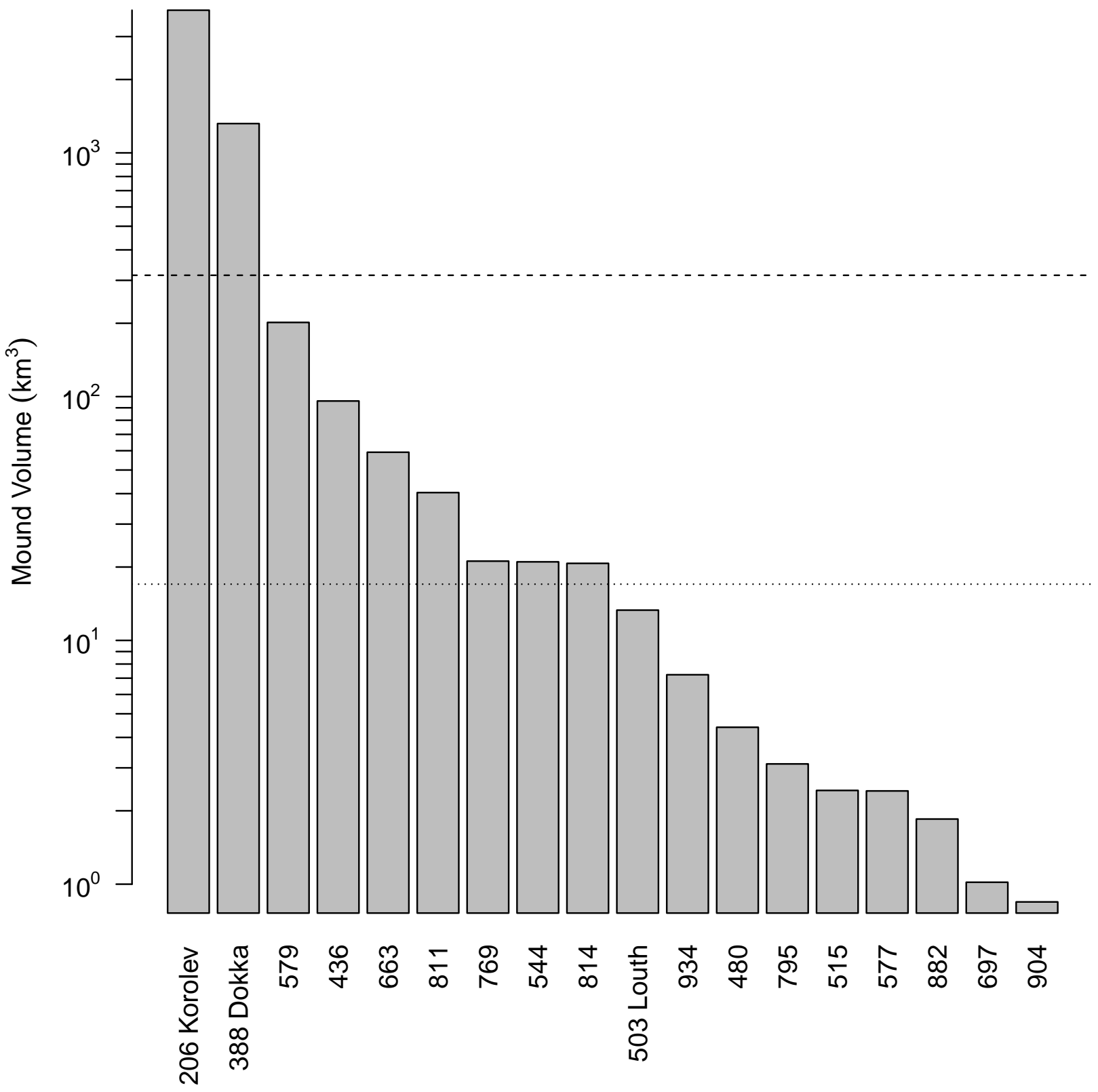


Figure 6 (black and white)

[Click here to download high resolution image](#)

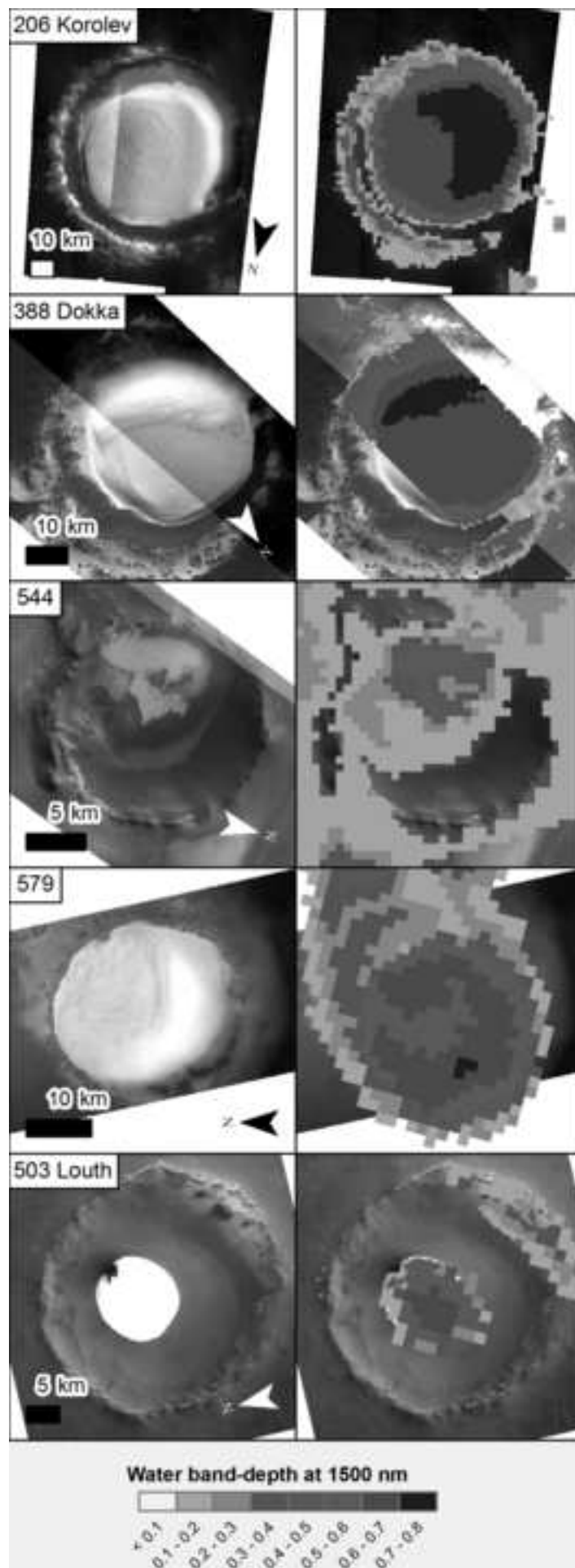


Figure 6

[Click here to download high resolution image](#)

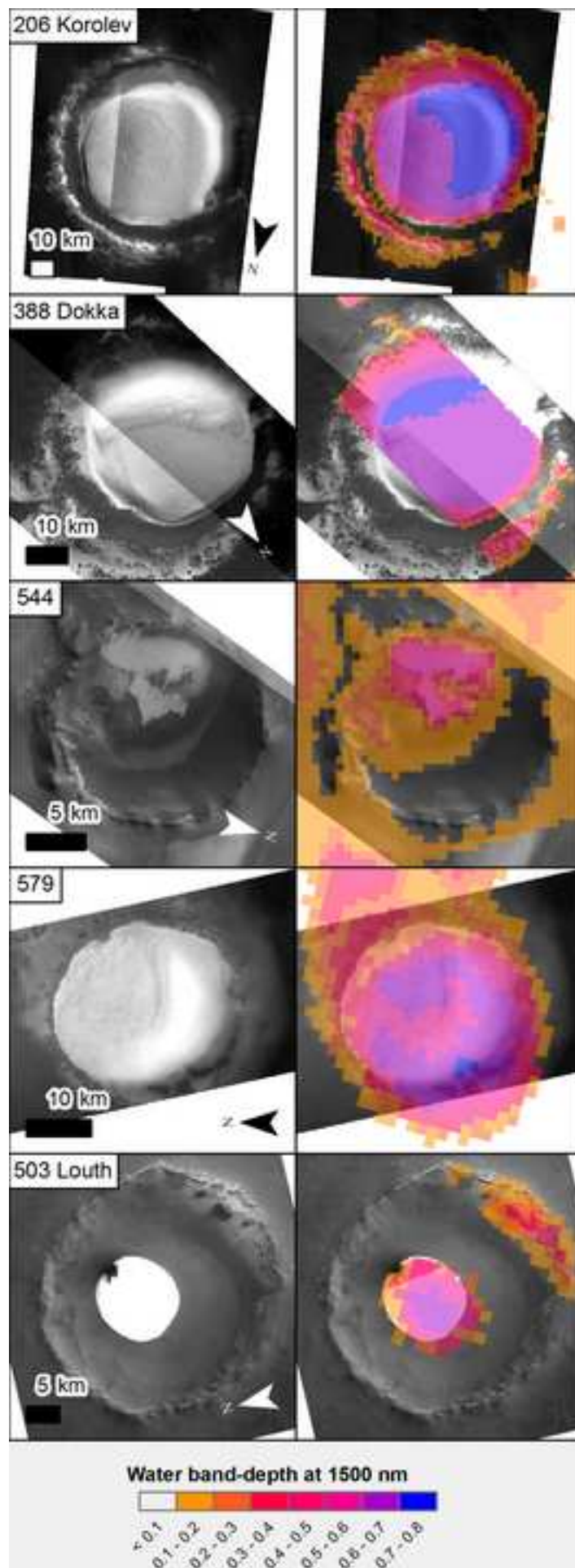


Figure 7 (black and white)

[Click here to download high resolution image](#)

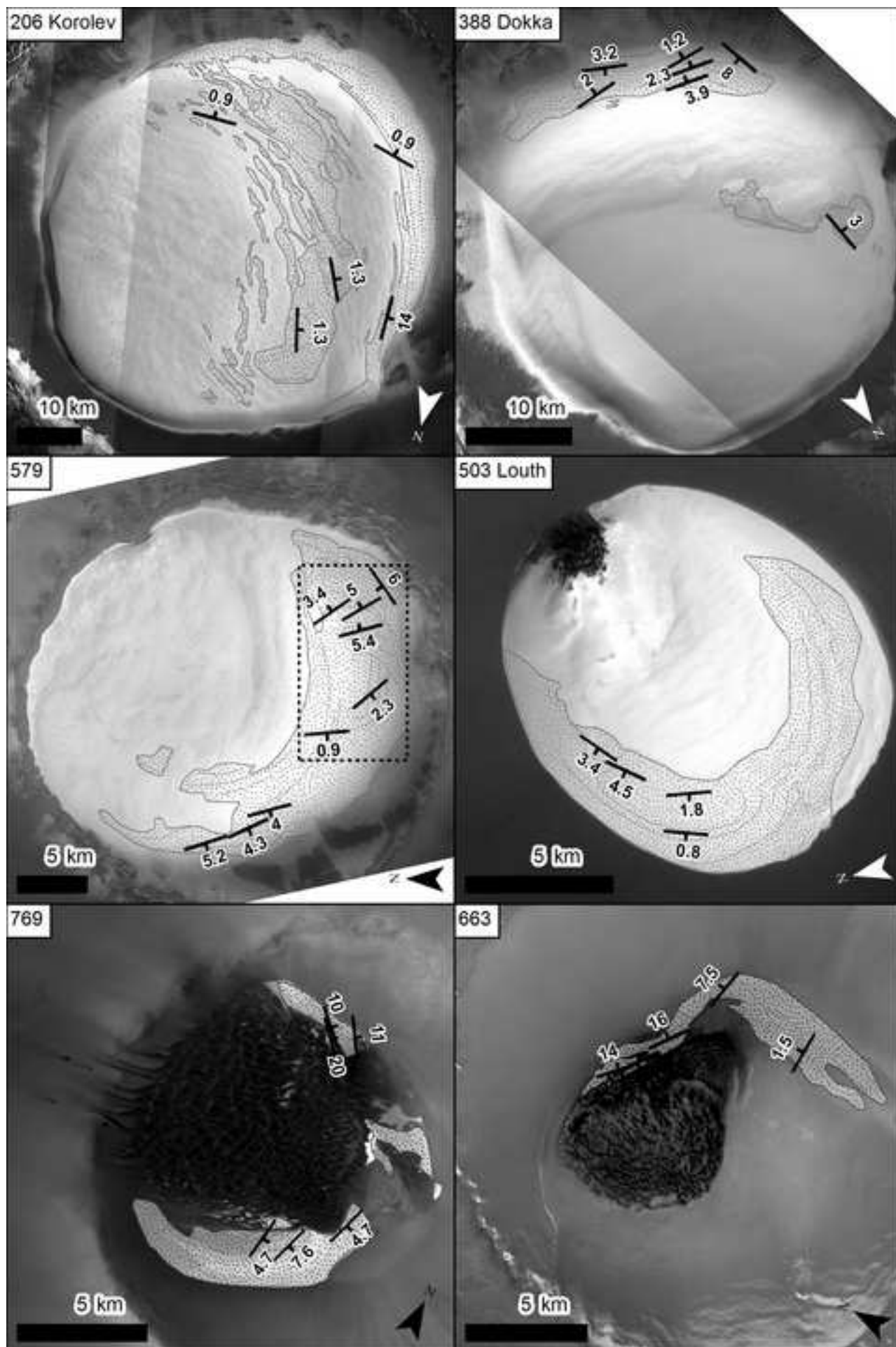




Figure 7  
[Click here to download high resolution image](#)

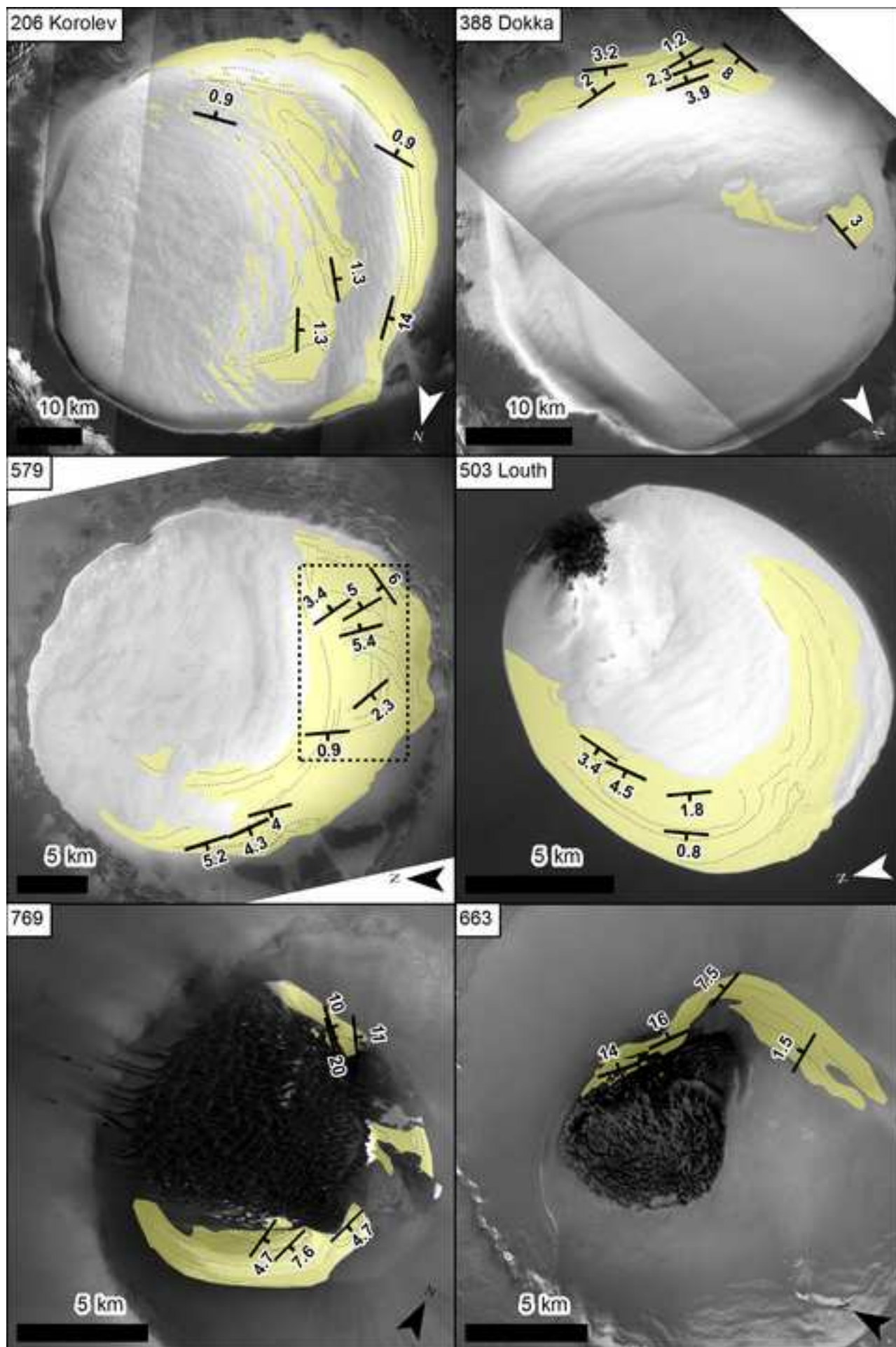


Figure 8 (black and white)

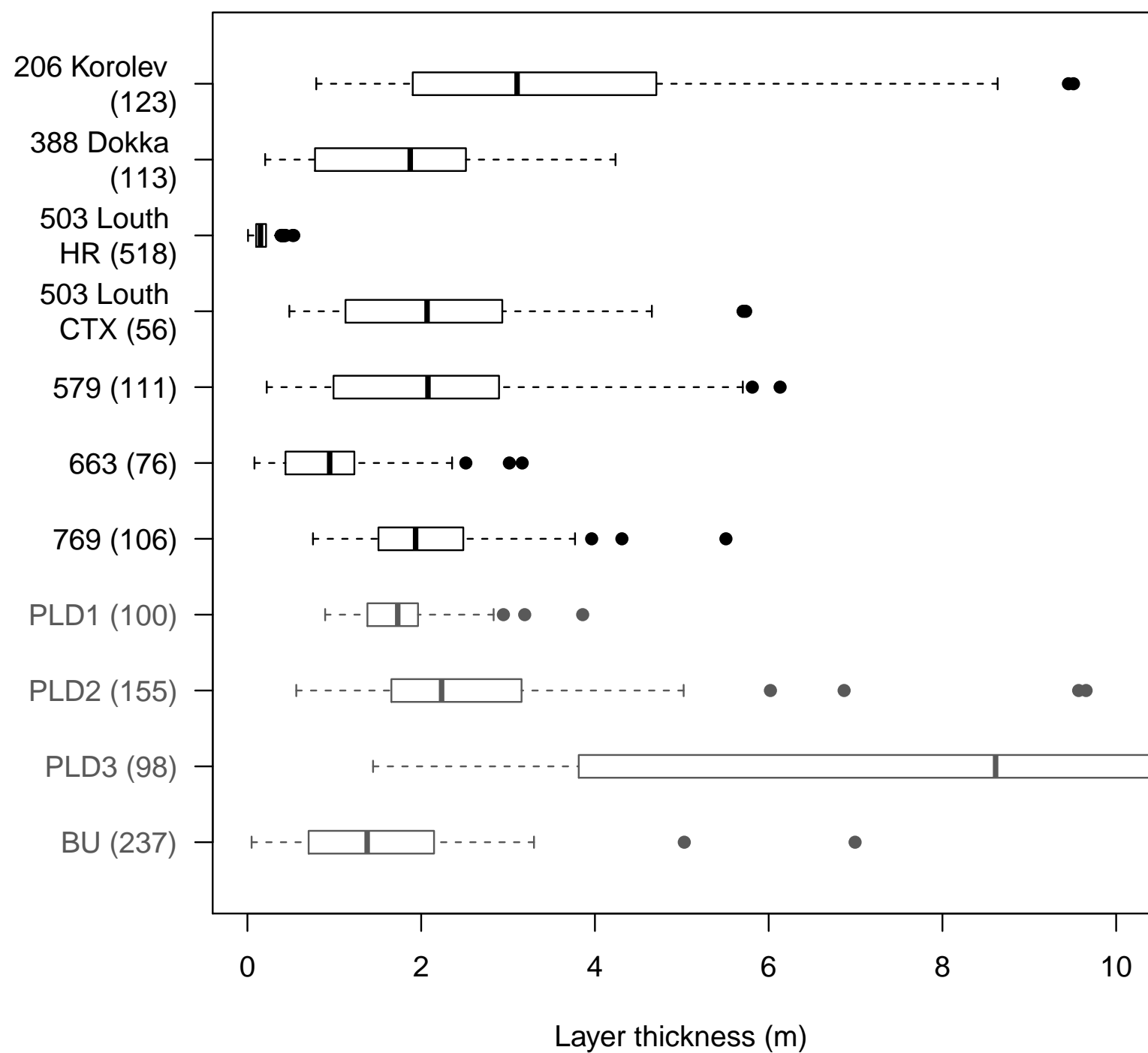


Figure 9 (black and white)

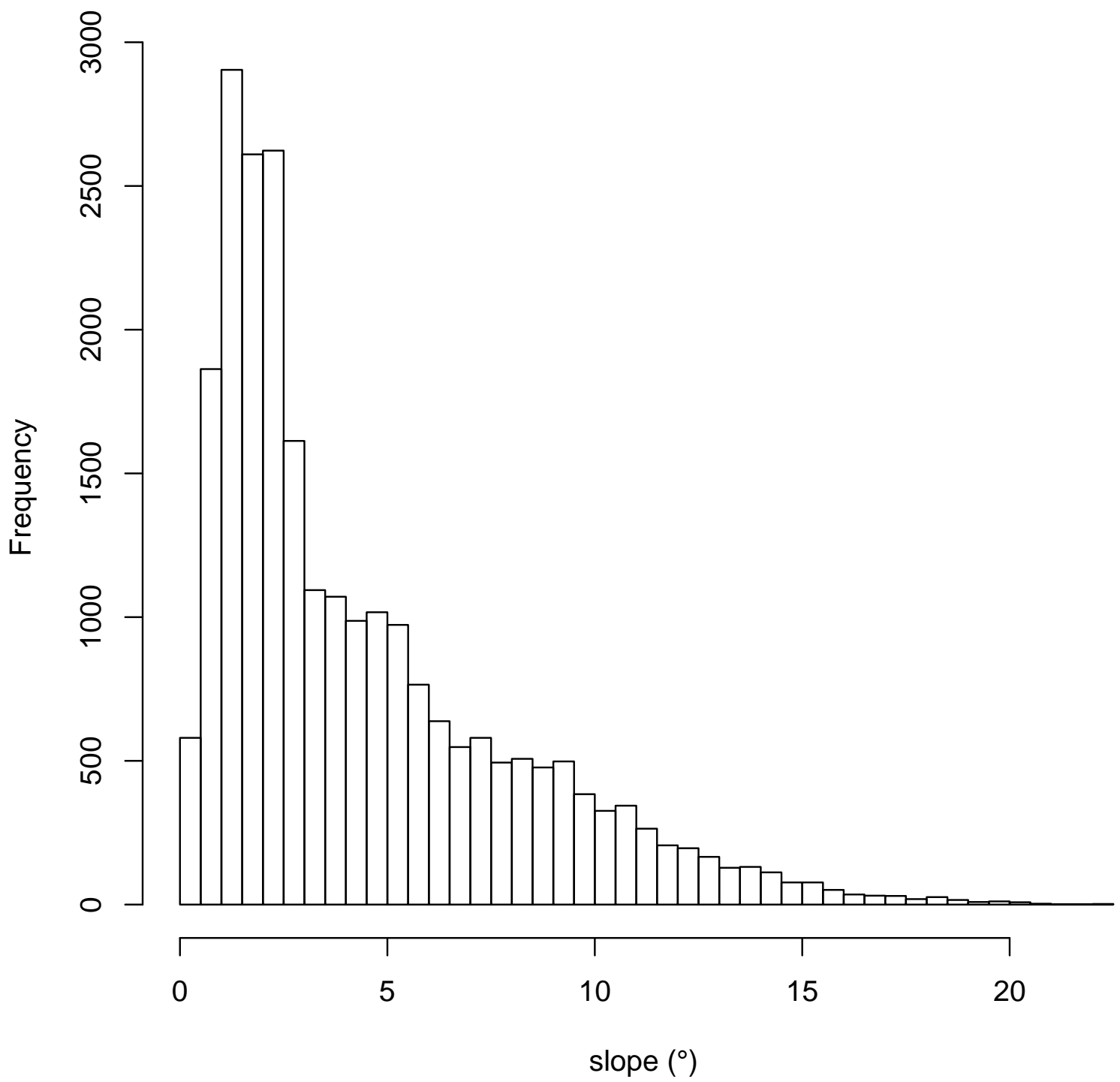


Figure 10 (black and white)  
[Click here to download high resolution image](#)

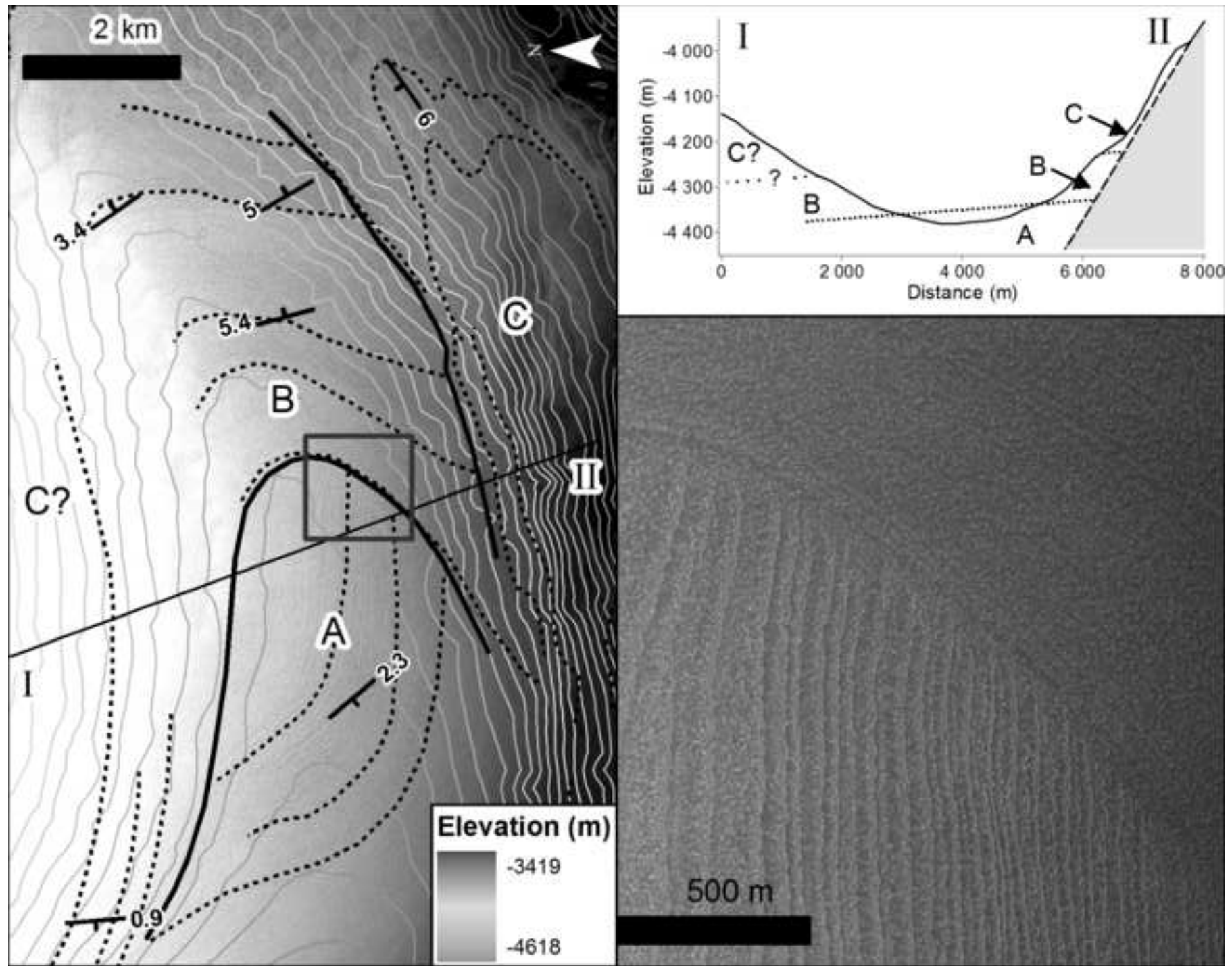


Figure 10  
[Click here to download high resolution image](#)

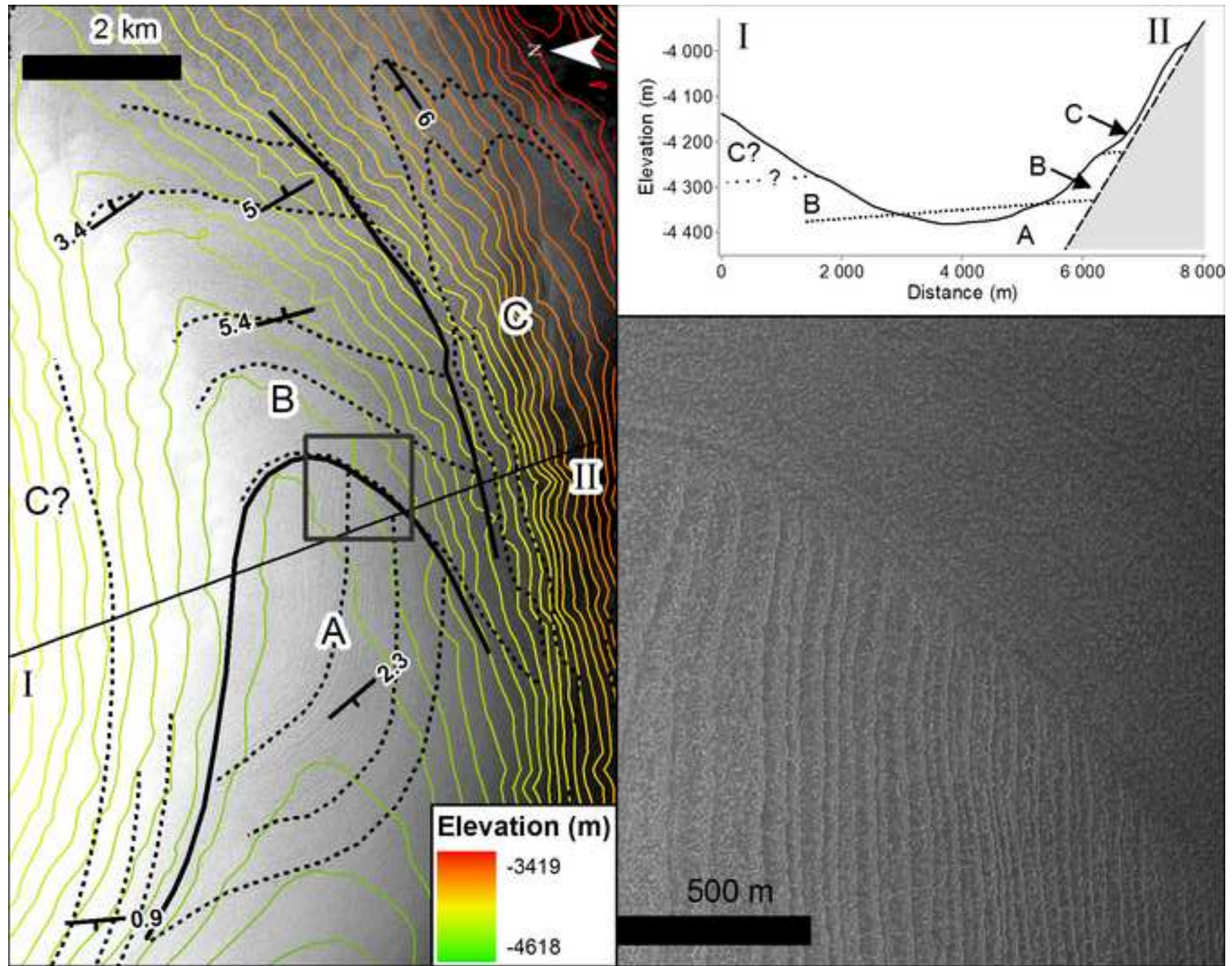


Figure 11 (black and white)  
[Click here to download high resolution image](#)

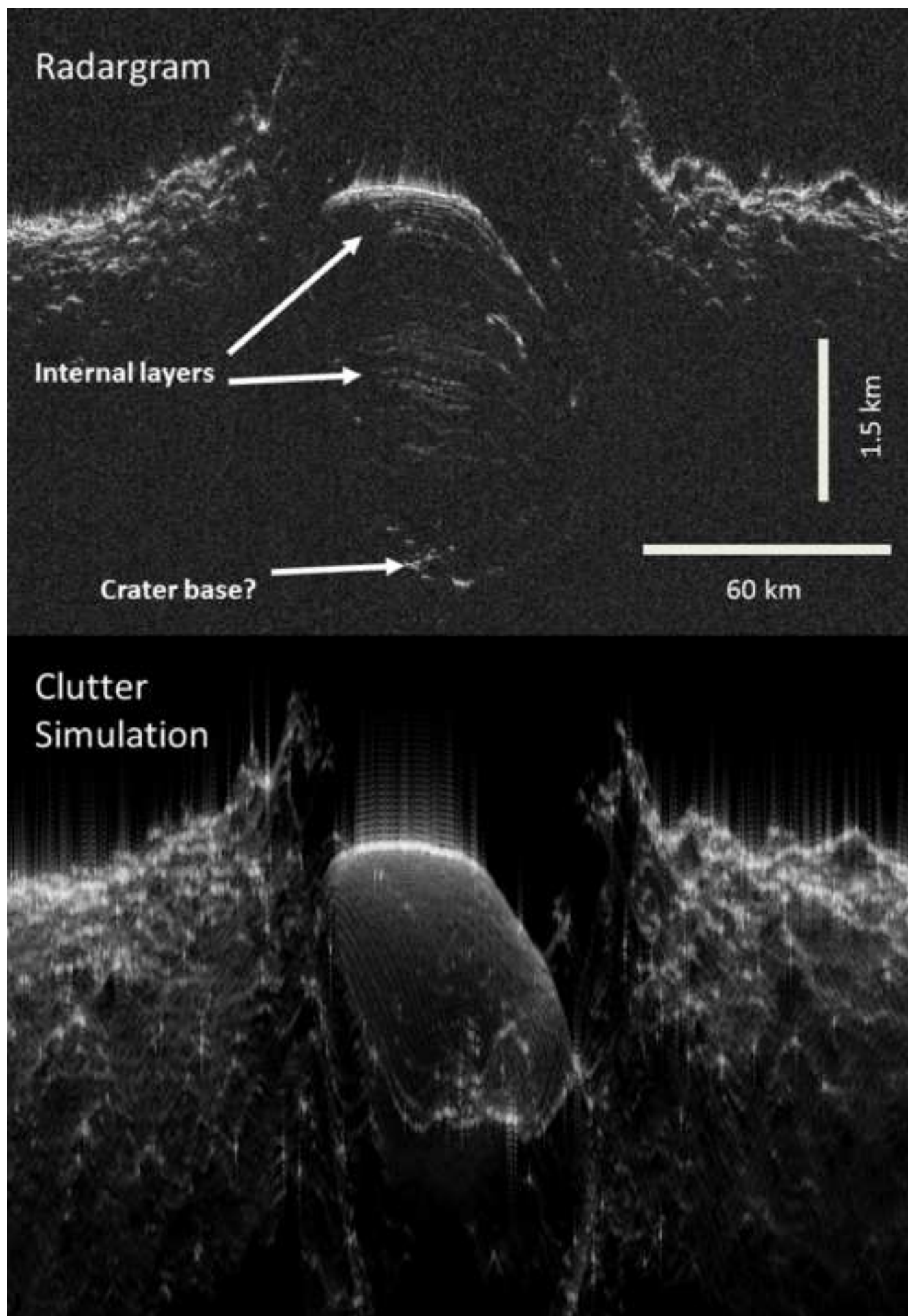


Figure 12 (black and white)

[Click here to download high resolution image](#)

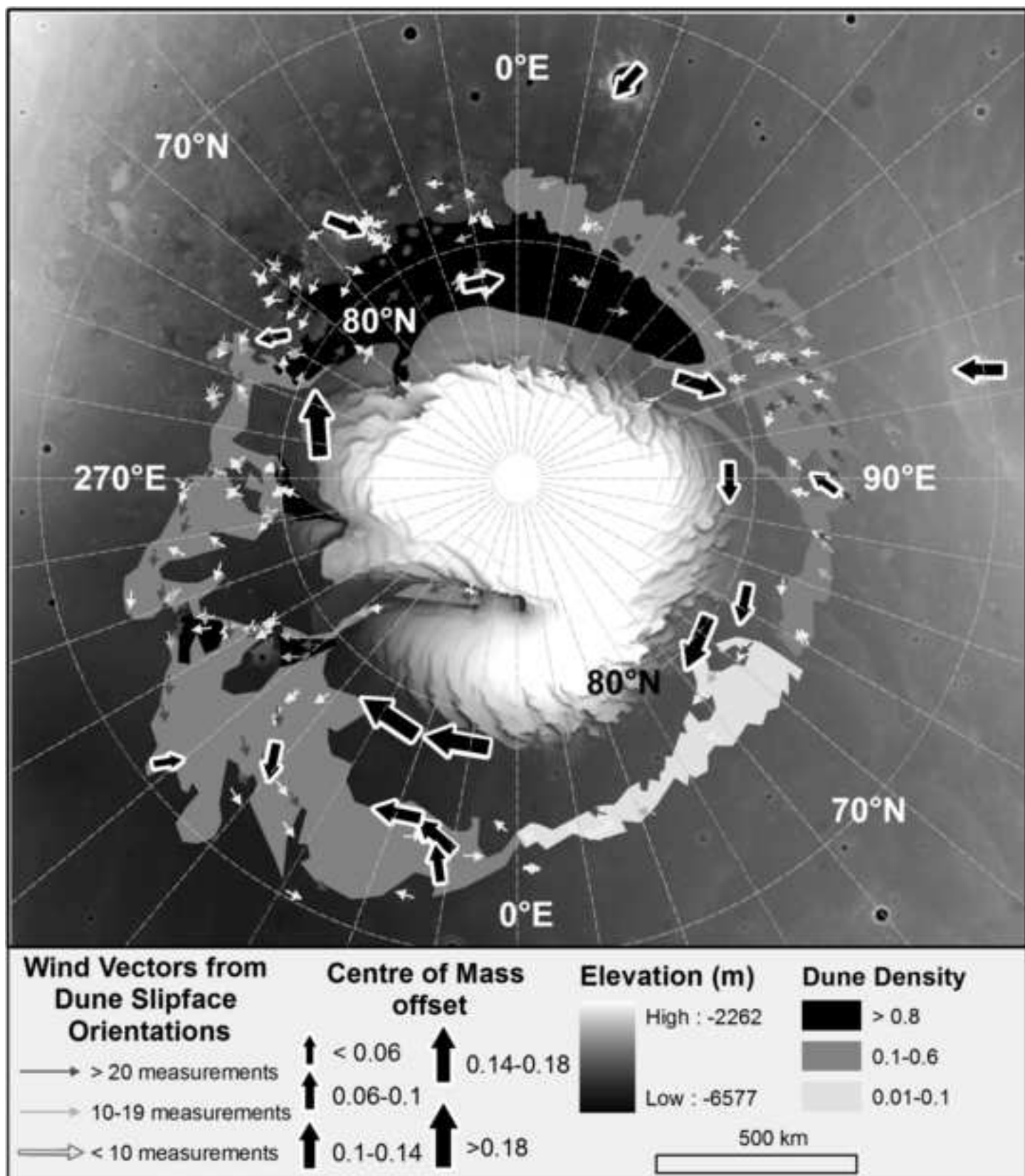


Figure 12

[Click here to download high resolution image](#)

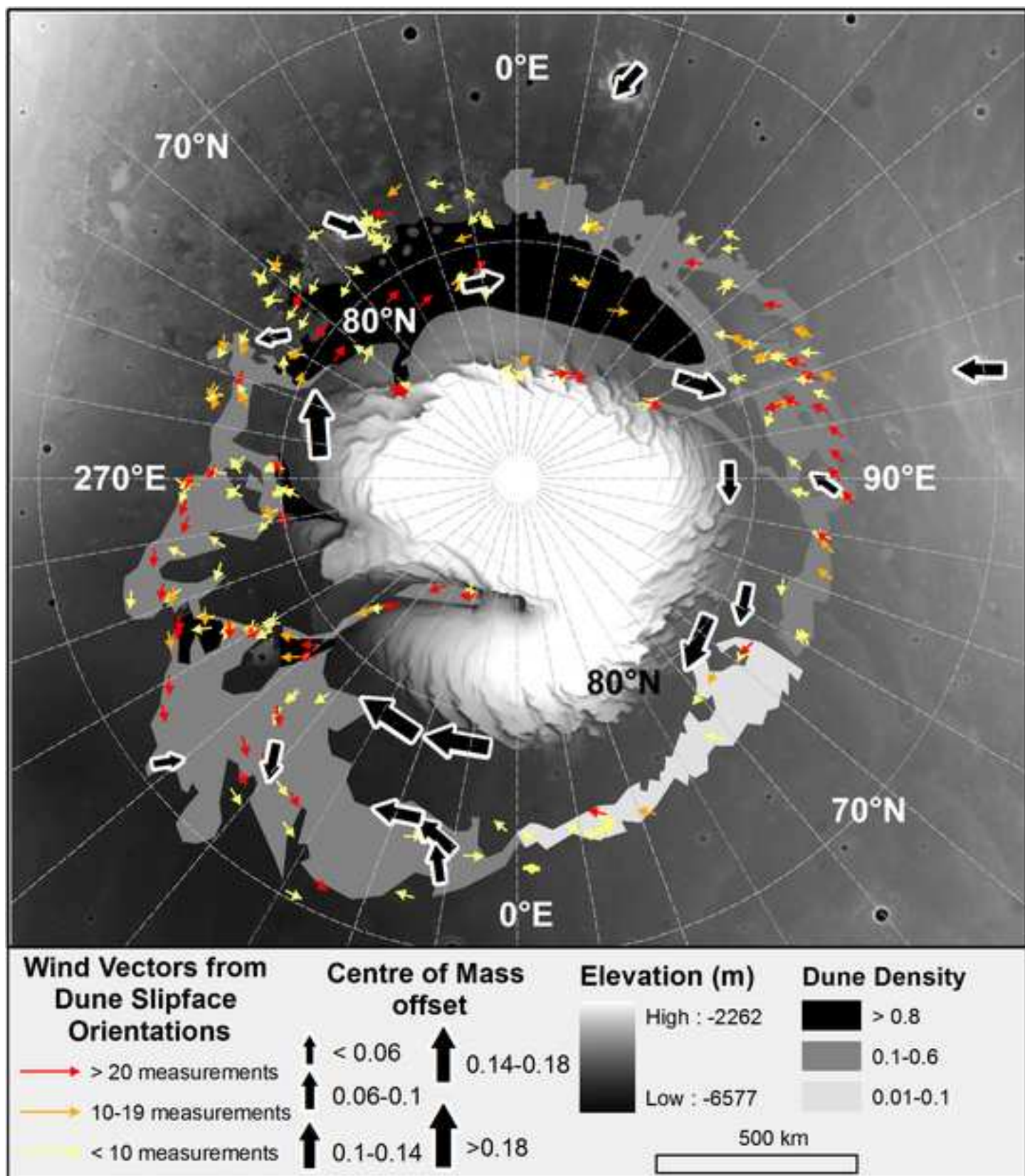




Figure13 (black and white)

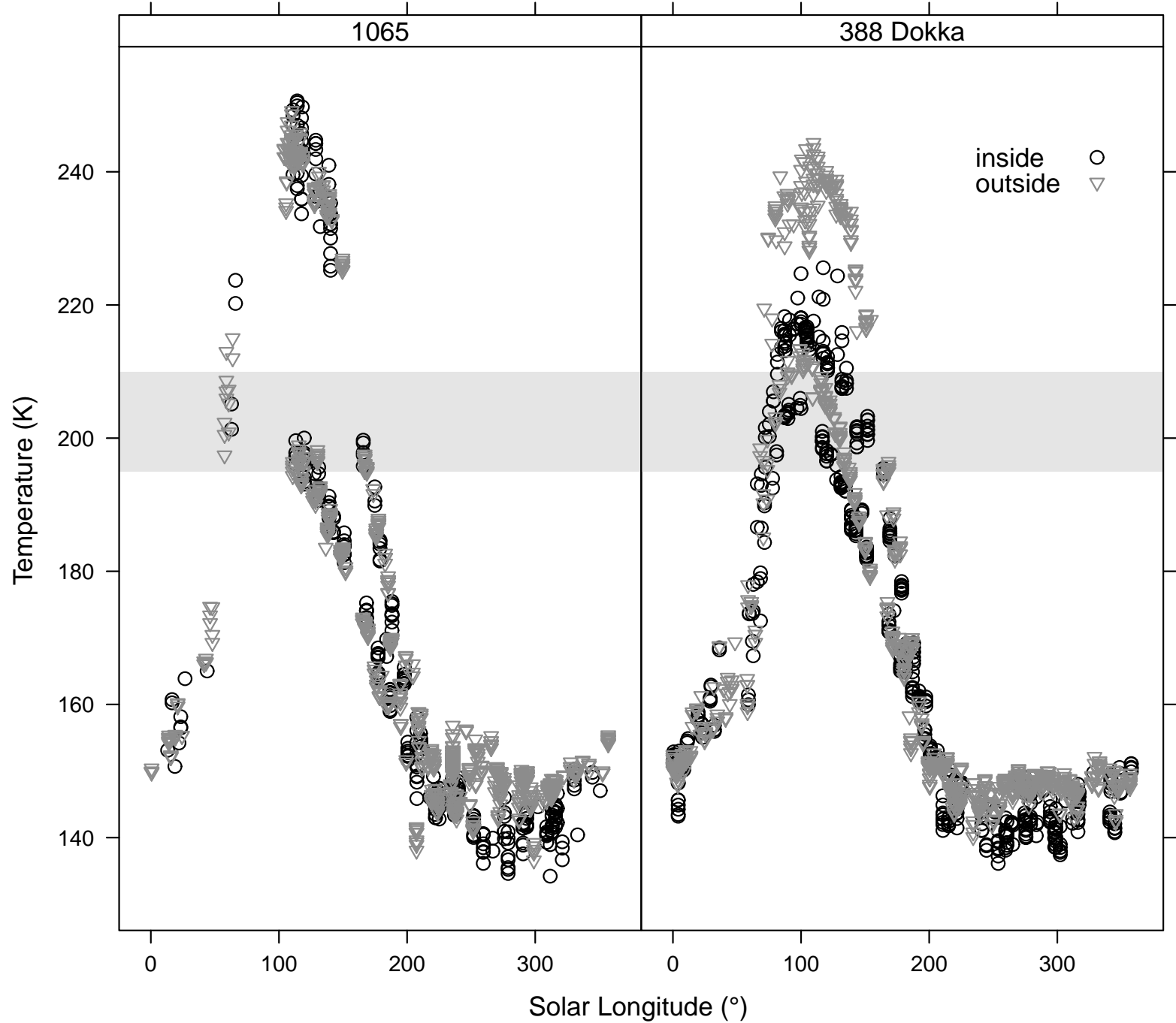


Figure13

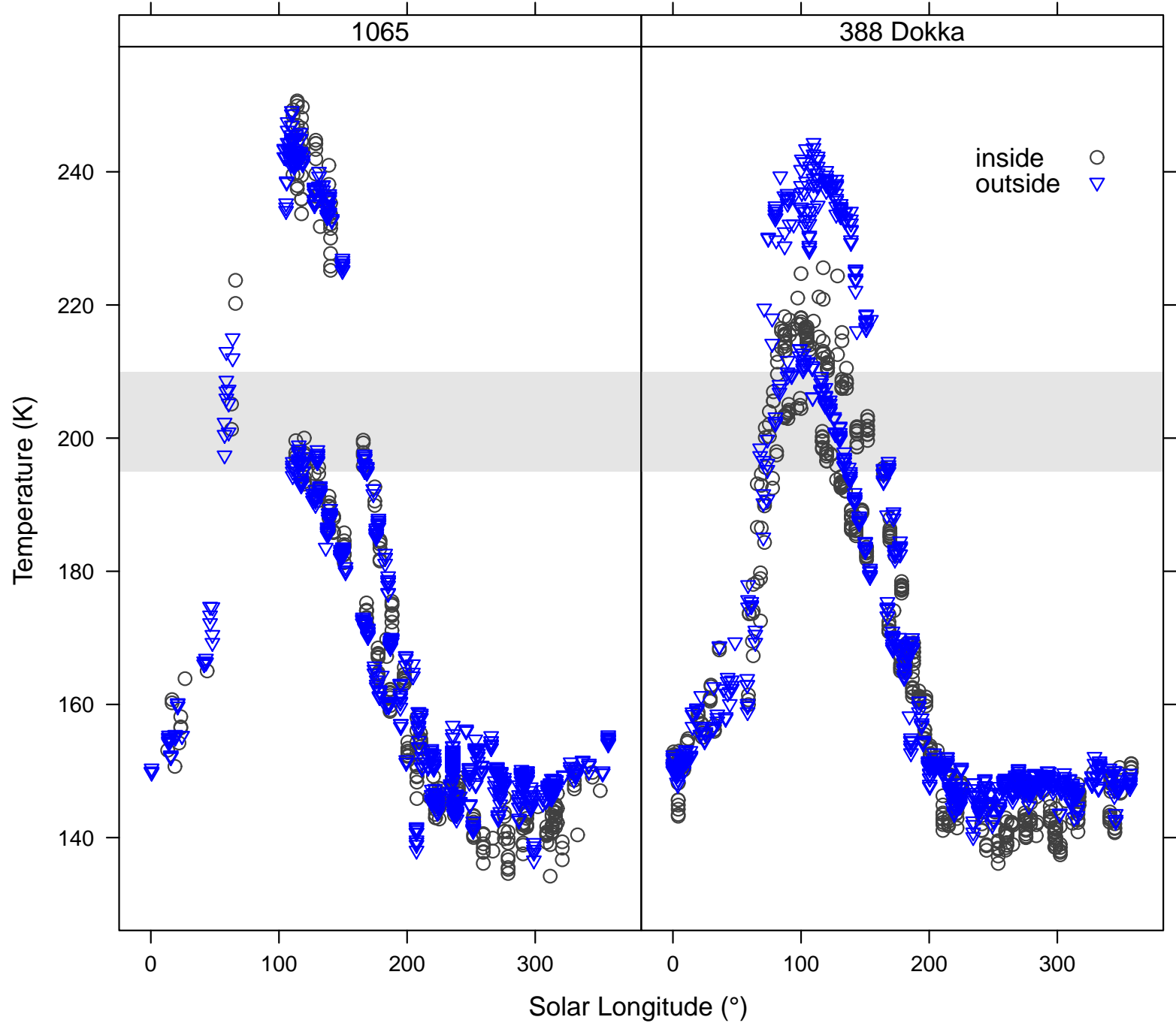


Figure 14 (black and white)  
[Click here to download high resolution image](#)

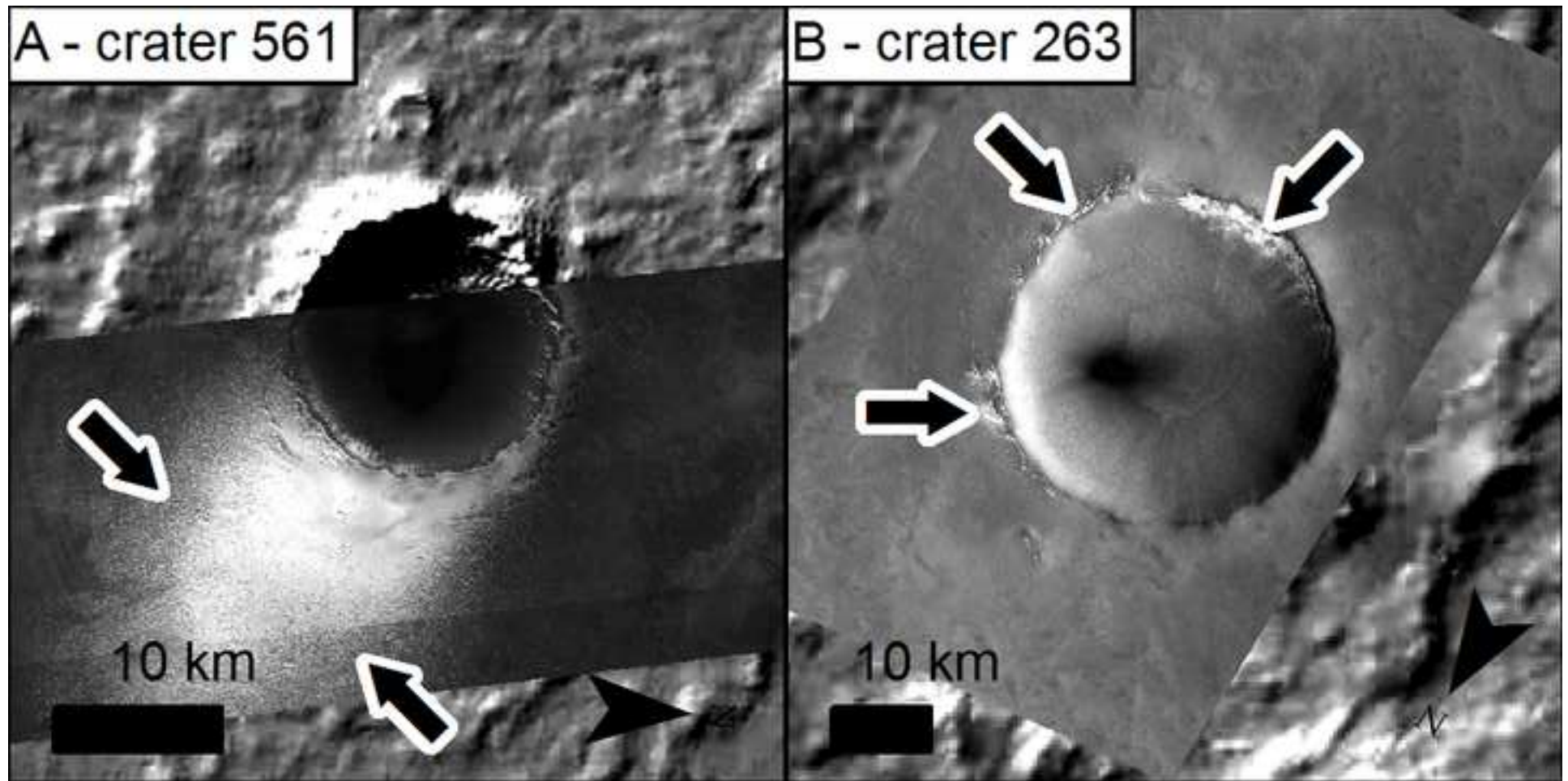


Figure 15 (black and white)  
[Click here to download high resolution image](#)

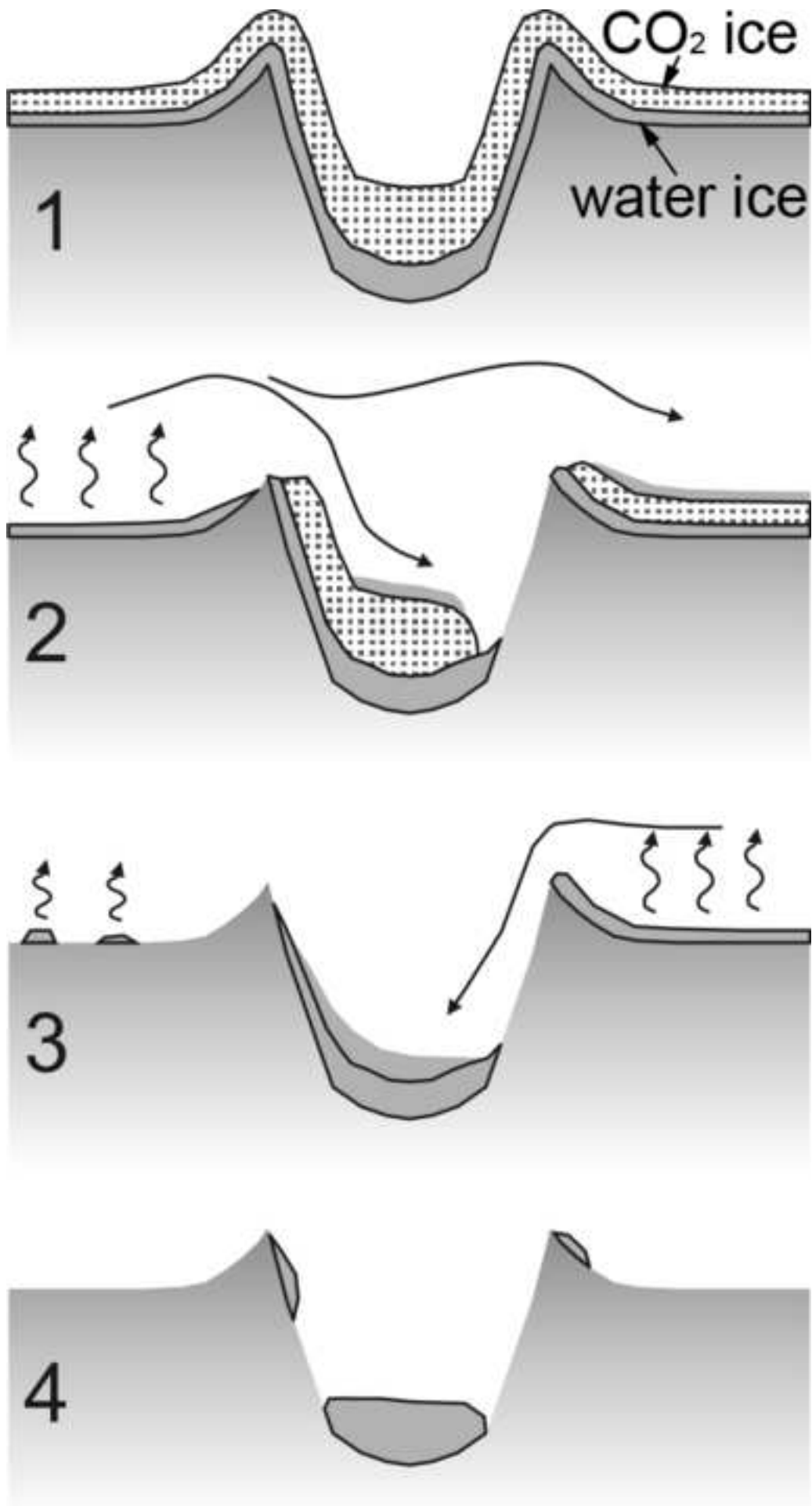


Figure 15  
[Click here to download high resolution image](#)

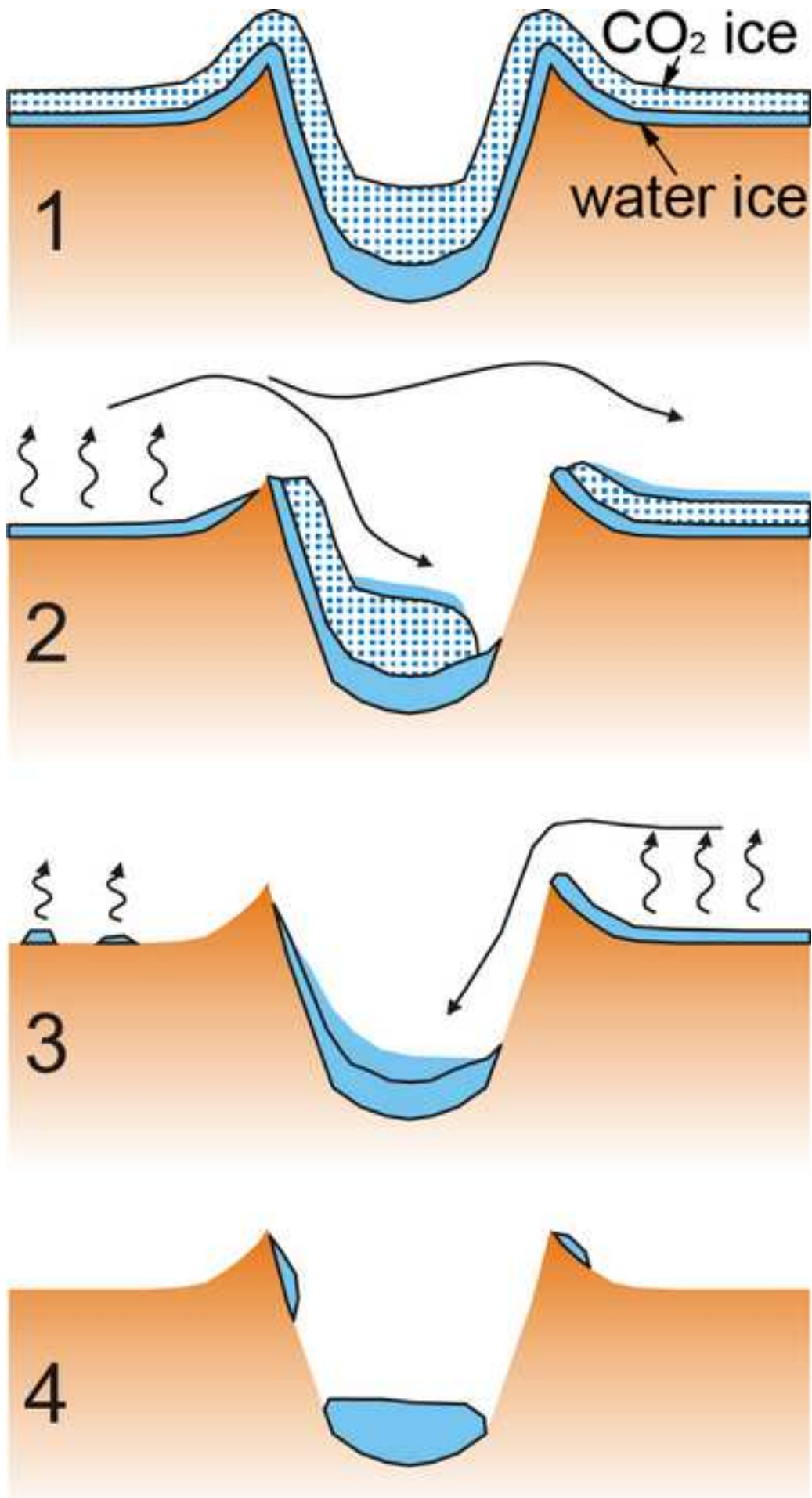
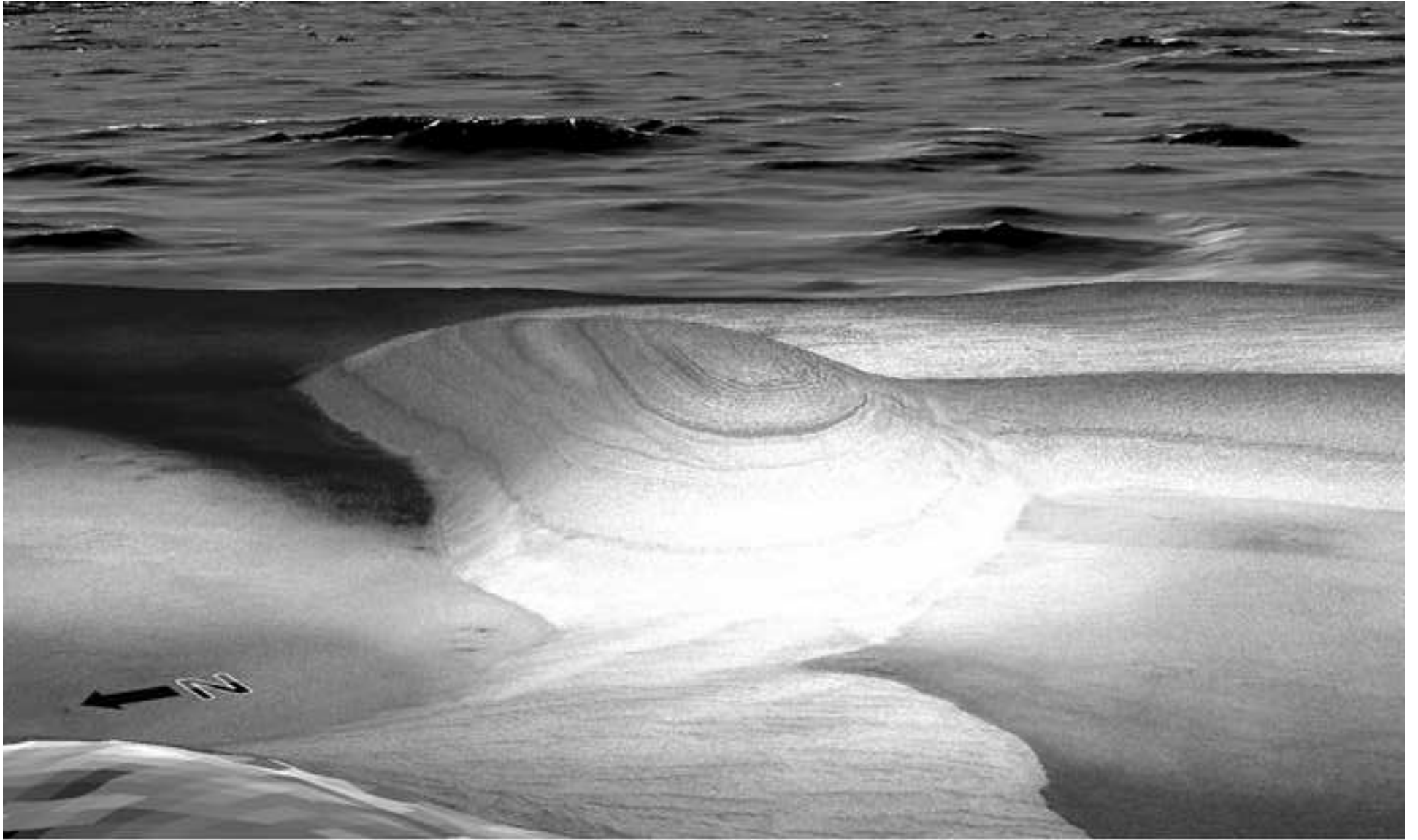


Figure 16 (black and white)  
[Click here to download high resolution image](#)



Sup. Mat. Fig. S1

[Click here to download Supplementary Material for on-line publication only: AllCrossSections.tif](#)